• U C •

FCTUC FACULDADE DE CIÊNCIAS
E TECNOLOGIA
UNIVERSIDADE DE COIMBRA

RICARDO JORGE DIAS SIMÕES

THERMO-RESPONSIVE ULTRASOUND IMAGING: MODELING AND PRELIMINARY RESULTS

Dissertação apresentada à Universidade de Coimbra para cumprimento dos requisitos necessários à obtenção do grau de Mestre em Engenharia Biomédica

Orientador:
Professor Doutor César Alexandre Domingues TEIXEIRA

Coimbra, 2014

Este trabalho foi desenvolvido em colaboração com:

Centro de informação e sistemas da Universidade de Coimbra (CISUC)

Laboratory of Ultrasound of the COPPE-Universidade Federal do Rio de Janeiro

Agradecimentos

Agradeço ao Professor Doutor César Teixeira e ao Professor Doutor Wagner Pereira e a todo o grupo do Laboratório de Ultrassons do Programa de Engenharia Biomédica do COPPE-Universidade Federal do Rio de Janeiro pelos conhecimentos teóricos e práticos que durante toda a minha formação me facultaram. Foi com um grande apreço que desenvolvi o meu trabalho sob a sua orientação. Obrigado pelos incentivos e conselhos prestados, fundamentais para a realização desta investigação. Ao centro de investigação e sistemas da Universidade de Coimbra (CISUC), por me dar a oportunidade de desenvolver o projecto, fornecendo todas as condições para a sua realização. Aos docentes que nele trabalham e que presenciaram a realização deste trabalho dedico uma palavra de gratidão. Aos meus colegas de mestrado, dirijo o meu obrigado, pela ajuda proporcionada e pelos momentos partilhados. Um agradecimento aos meus Pais e ao meu irmão Tiago, pela orientação, carinho e companhia que me deram no meu percurso de vida. Por fim um agradecimento a todos os que estiveram envolvidos neste projecto. Obrigado pela amizade demonstrada e pelos momentos de convivência fantásticos.

Financial Support

Financial support of the Luso-Brazilian cooperation project CAPES/FCT “Thermo-response” (FCT/CAPES: 10172/13-0) and to CNPq and FAPERJ, that enabled the development of the simulation part of this thesis in the University of Coimbra, and the experimental part in the Laboratory of Ultrasound of the COPPE-Universidade Federal do Rio de Janeiro.

”The history of science shows that theories are perishable. With every new truth that is revealed we get a better understanding of Nature and our conceptions and views are modified.” - NIKOLA TESLA

Resumo

O ultrassom é uma onda mecânica, com frequência acima da gama audível pelo ouvido humano, e que pode ser usada para formação de imagens, como é exemplo as ultrassonografias. A ultrassonografia convencional é uma modalidade de imagem não-invasiva aparentemente sem efeitos secundários. Além disso é de baixo custo, versátil e dada a sua simplicidade pode ser adquirida em tempo real. No entanto, a sua resolução espacial fica aquém de imagens obtidas por outras técnicas, como por exemplo a ressonância magnética nuclear (Magnetic Ressonance Imaging-MRI). No sentido de desenvolver técnicas de imagem que incluam as vantagens do ultrassom, aliadas a uma boa qualidade de imagem, diversas variantes de ultrassonografia convencional têm sido propostas nos últimos 20 anos, como por exemplo, o caso da elastografia.

A motivação deste trabalho centra-se na melhoria na qualidade de imagem por ultrassom, através da análise da variação de intensidade de escala de cinzentos em imagens convencionais, quando um meio é sujeito a uma variação de temperatura. A literatura reporta que mudanças monotónicas da energia de retro-espalhada (Changes in Backscattered Energy-CBE) ocorrem com a temperatura, e que essas mudanças dependem do tipo de espalhador (meio). Mais precisamente, é reportado que meios compostos por espalhadores do tipo aquoso resultam em curvas de CBE que decrescem com a temperatura, e que meios compostos por espalhadores do tipo lipídico resultam em curvas de CBE crescentes com a temperatura.

Deste modo, o objectivo primário desta tese é averiguar a hipótese que as CBE devido a variações de temperatura, propagam-se através da ”pipeline” (em toda a sequência) de processamento nos equipamentos de ultrassom convencionais e são perceptíveis ao nível da imagem final, tornando possível a extração de informação sobre o meio em análise e que poderá resultar numa melhoria da qualidade da imagem. Consequentemente, o outro objectivo da tese é averiguar se a informação extraída da dinâmica da relação temperatura-intensidade para cada pixel resulta em imagens de melhor qualidade.

Para avaliar a anterior hipótese, recorre-se a um programa de elementos finitos, o COMSOL Multiphysics, onde é simulado o aquecimento do meio por duas abordagens diferentes: uma que envolve a reprodução de um arranjo experimental real e que consiste na implementação de uma variação de temperatura gradual usando a circulação de água por uma espira de cobre; e outra onde se simula o aquecimento rápido por ultrassom, usado normalmente em terapia. Foi acoplado ao modelo de aquecimento desenvolvido, um modelo construído de raiz que permitiu simular as CBE para diferentes tipos de meios.

Por forma a cumprir o segundo objectivo, isto é, a formação de novas imagens a partir das relações temperatura-intensidade para cada pixel, foram ajustados modelos polinomiais e de correlação à relação temperatura-intensidade do ultrassom. Parâmetros dos modelos foram posteriormente representados para cada pixel formando imagens. As imagens, representam, portanto, a densidade de cada espalhador e a variação velocidade de som, com a temperatura em cada ponto do meio.

Os resultados das simulações comparados com as imagens reais levaram a concluir que, de facto, as CBE em função da temperatura propagam-se pelo ”pipeline” dos equipamentos de ultrassom e que através do processamento de imagens convencionais se pode extrair informação a seu respeito analisando as variações de intensidade de cada pixel. Consequentemente, estas variações podem ser modeladas e representadas para cada pixel, formando o que nesta tese chamamos de imagens ”termo-responsivas”. Foi possível no-

tar que a nova metodologia permite a obtenção de imagens mais sensíveis com textura melhorada do que a imagem de ultrassom convencional.

No decorrer do trabalho verificaram-se curvas de intensidade das imagens reais para além do que era previsto pelo modelo teórico, sendo que estas continham oscilações de frequência bem definida. Tirando partido desta informação foi ajustado mais um modelo para incluir estas oscilações e também a tendência fundamental. O modelo considerado permite a identificação de sistemas lineares e invariantes (LTI) através do ajuste de uma função transferência de segunda ordem, caracterizada por dois parâmetros fundamentais: a frequência natural não amortecida (para captar as oscilações) e o fator de amortecimento (para captar a tendência crescente ou decrescente). Deste modo, foi possível criar mais dois tipos de imagem. As imagens criadas a partir da frequência natural não amortecida parecem enaltecer as interfaces entre as diferentes estruturas, ou seja, as oscilações parecem ocorrer na transição entre os meios. Por outro lado, o fator de amortecimento resulta numa melhor identificação da dinâmica da variação de intensidade, resultando em imagens mais detalhadas. No entanto, será necessário mais investigação sobre estas oscilações que não são contempladas pelo modelo atual de CBE. No seguimento do trabalho também serão realizadas novas experiências para consolidar o conhecimento entre as imagens termo-responsivas e variações de densidade. Esta investigação ficará para trabalho futuro.

Palavras-Chave: Ultrassom, Mudança na Energia de Retroespalhamento, Modelo Numérico, Simulação.

Abstract

Ultrasounds (USs) are characterized as a form of mechanical wave, with frequency above the range that human are able to hear, and is used to create images, called ultrasonographies. The conventional ultrasonography is a non-invasive imaging modality without secondary effects and also known to be: low-cost, versatile and due to its simplicity, can be acquired in real-time. However, its image quality is inferior than the quality obtained with other modalities, like the Magnetic Resonance Imaging (MRI). Aiming to develop imaging techniques which include both the benefits of ultrasonography and good image quality, alternatives to conventional ultrasound have been proposed in the past 20 years, as an example, the elastography and harmonic imaging.

The motivation of this thesis is the improvement of conventional USs image quality by analyzing gray-level intensity variations observed in ultrasound images when the medium suffers a temperature change. Literature reports monotonic changes on backscattered energy (CBE) from sub-wavelength scatterers due to temperature variations and type of medium. Precisely, it is reported that CBE vary negatively with the temperature increase if the medium is based on aqueous scatterers, and positively if the medium is composed by lipid-based scatterers. Therefore, the thesis main objective is to confirm that CBE, due to temperature variations, propagate along the processing pipeline of the ultrasound equipments and have an expression on conventional B-mode images, turning possible to extract additional information about the studied medium, resulting in a improved image

quality. Consequently, the other thesis objective is to demonstrate that the experimentally extracted intensity-temperature dynamics for each pixel results in a better imaging quality.

To prove the previous hypothesis, we use finite element computer software, the COMSOL Multiphysics, where two different simulations were made: one involving the reproduction of a real laboratorial experimental setup used to change the temperature of the medium gradualy. This experimental setup uses a copper pipe to circulate water at different temperatures and consequently change the temperature of the medium; and another simulation where a fast heating is achieved by ultrasound application, generally used in thermal therapies. On top of the temperature change simulations, a brand-new CBE simulation that will be the key element of this thesis was developed.

In order to complete the second objective, the formation of new images from the gray-level intensity variations, polynomials and correlation models were fitted to the temperature-intensity relations extracted for each pixel. Parameters from the models were then represented for each pixel, forming the so called “thermo-responsive images”.

The simulations results indicated that, in fact, intensity variations with temperature are closely related with CBE. Thus it is possible to assume that CBE propagate along the processing pipeline of the ultrasound equipments and has an expression at the gray-level intensity in conventional B-mode images, enabling the development of thermo-responsive images, and the understanding of its basis. Simulations also allow us to observe that CBE is sensitive to density and also to changes on SOS that depend on temperature. Thus, the thermo-responsive images from real tissues maps the combined effect of density and SOS change with temperature, leading to more sensitive and more informative textures than the conventional ultrasound images density map of the tissue under analysis.

In the course of the work, it was verified that the gray-level intensity variations with temperature described oscillations that are not predicted by the present CBE theory. Thus, a new approach to model the intensity variations with temperature was introduced. This

new approach is based on a second-order transfer function modeling, usually used to identify linear time and invariant (LTI) systems. The transfer function is characterized by two fundamental parameters: the undamped natural frequency (to detect oscillations) and the damping ratio coefficient (to detect amplitude increasing or decreasing). With this two parameters, it was possible create two image types. The images based on the undamped natural frequency seem to highlight the interfaces between structures, i.e., the oscillations seem to appear in medium transitions. On other hand, the damping ratio coefficient result in a better intensity variation identification, resulting in more detailed images.

As future work, it will be necessary more investigation aiming to find a theoretical basis for the observed oscillations that are not contemplated in the present CBE model. At more experimental level new experiments will be performed aiming to find out more about the relation between the thermo-responsive images and the underlying density and SOS variations with temperature in *ex-vivo* tissues.

Keywords: Ultrasound Imaging, Changes on Backscattered Energy, Numerical Modeling and Simulation

Acronyms

Ultrasounds (USs)

Changes in Backscattered Energy (CBE)

Three dimensional (3D)

Four dimensional (4D)

Magnetic Resonance Imaging (MRI)

Computational Tomography (CT)

Single Positron Emission Computational Tomography (SPECT)

Positron Emission Tomography (PET)

Optical Coherence Tomography (OCT)

Electrocardiography imaging (ECGi)

Frame Rate (FR)

frame per second (fps)

Pulsed-Wave (PW)

Continuous-Wave (CW)

Young's modulus (E)

High Intensity Focused Ultrasound (HIFU)

Radio Frequency (RF)

Finite Element Method (FEM)

Finite Element (FE)

Finite Element Analysis (FEA)

Degree of Freedom (DOF)

Multifrontal Massively Parallel sparse Solver (MUMPS)

Parallel Direct sparse Solver (PARDISO)

Sparse Object Oriented Linear Equations Solver (SPOOLES)

List of Figures

Contents

List of Tables

Chapter 1

Introduction

1.1 Motivation and Objectives

Ultrasound enables the development of minimally invasive, low-cost, and versatile imaging. However, its image quality is lower than those achieved by other technologies, such as Magnetic Resonance Imaging (MRI). In the past years, several new ultrasound based methodologies were proposed to join the advantages of ultrasound with improved imaging quality. One example is elastography that explores the elastic tissue properties to enhance structures with similar acoustic impedance.

The focus of this thesis is in the physics of a new imaging technique, called the thermo-responsive imaging, that aims also to contribute with an alternative ultrasound imaging improvement by exploring the temperature-dependent changes on backscattered energy (CBE). CBE is claimed to vary monotonically but differently depending on the medium type. It is referred that mediums made of lipid scatterers contributes with CBE curves that increase with temperature, while tissues composed by aqueous scatterers originate CBE decreasing trends with temperature. Therefore, in this thesis, it is developed a set of simulation models based on finite element methods that helps to understand the underlying

physics of the temperature-CBE relation. Thus, the main objective is the development of coupled temperature-CBE simulations in COMSOL Multiphysics® (COMSOL,Inc). The goal of these simulations is the validation of the hypothesis that CBE propagates along the processing pipeline of the ultrasound equipments and are expressed on the intensity of conventional bi-dimensional images (B-mode), making possible the extraction of relevant information at the conventional image level, enabling the development of images with improved quality. The motivation for that simulations are based in a fundamental experience where the variation of grayscale level was verified but not explained. This thesis uses the experiment realized in [18], where the supervisor of this thesis is the author. All simulations aim to understand the experiment and to validate the main hypothesis. The second objective of this thesis is the development of thermo-responsive images by analyzing the image intensity changes at the pixel level in conventional B-Mode images. The data collected in [18] is, also, used in this thesis for real imaging production. For each pixel the grayscale intensity change with temperature [18]. The grayscale intensity variations are modeled by different types of models and then, parameters from these models are represented forming different parametric images.

1.2 Background

USs are widely used in clinical diagnostic due to its portability and low-cost instrumentation. In the last decades two important concerns of USs research were: the improvement of the quality of the image, and the development of trustworthy methods for non-invasive temperature estimation for hyperthermia purposes. Concerning improvement of image quality, modalities such as harmonic imaging by administration of contrast agents, and elastography are the most important ones [19]. On the other hand, different features from US were extracted aiming to estimate temperature non-invasively. To mention that, the existence of non-invasive temperature estimation methods will be of extreme importance for the safe and effective application of thermal therapies, such as hyperthermia. Mag-

netic resonance imaging (MRI) solved partially the problem of temperature estimation, i.e., it achieved acceptable errors and real-time processing [19]. However, it requires expensive instrumentation, its applicability is limited (e.g. due to metal prothesis), and lack of portability. Among the US features, temporal echo-shifts originated from stationary targets, and CBE from sub-wavelength medium inhomogeneities were the more studied ones [20]. Both measures detect temperature changes because they are sensitive to changes on ultrasounds velocities and densities with temperature. However, temporal echo-shifts are highly sensitive to medium movements. In this sense CBE is more robust and varies monotonically with temperature. It was reported that lipid scatterers contribute with monotonically increasing CBE curves with temperature, while aqueous scatterers have monotonically decreasing trends [19] [20], [21]. Image-processing methods have also been applied for non-invasive temperature estimation. The fundamental physical assumption is that temperature variations induce wave propagation changes that modify the USs signals and these changes have an expression in ultrasonographic images. In general, the main effects are apparent image motion due to changes on ultrasounds velocity, as well as changes on image intensity due to variations on the amplitude of echo signal caused by modifications on the attenuation and backscattered properties [19]. To the best of our knowledge, the variation of the temperature-dependent features were always viewed as an indicator for temperature tracking, and never considered for imaging purposes as it is considered in this thesis.

1.3 Chronogram

1.4 Main Contributions

This thesis reports the first developments concerning a new methodology for a new imaging using backscattered ultrasound. The two main contributions were:

1. COMSOL models that simulate 4D(3D+time) temperature maps, and 4D CBE

Table 1.1: Activities

Activities	Description
A	State-of-the art review.
B	Development of the pipe-flow heating simulation based on a real laboratory experiment.
C	Development of ultrasound heating simulation.
D	Development of thermo-responsive images from simulations.
E	Development of identification system models for the encountered oscillations.
F	Development of thermo-responsive images for ex-vivo tissue samples and comparison with original US images.
G	Thesis and scientific papers writing.

Table 1.2: Activity Chronograph

Year	**2013**				**2014**							
Month / **Activity**	**Sep**	**Oct**	**Nov**	**Dec**	**Jan**	**Feb**	**Mar**	**Apr**	**May**	**Jun**	**Jul**	**Aug**
A												
B												
C												
D												
E												
F												
G												

maps of tissue samples. These model helped to understand the physical phenomena that lead to the development of thermo-responsive images;

2. Modeling of the image intensity changes at the pixel level in conventional B-mode images, which enabled the development of thermo-responsive images by representing appropriate model parameters.

This thesis contributed with the following publications in Papers in conference proceedings:

1. Simões R. J., Kruger M. A., Pereira W. C. A. and Teixeira C. A.. A coupled 4-

Dimensional Temperature-Change in Backscattered Ultrasound Energy simulation model. In proceedings of the 6th European Conference of the International Federation for Medical and Biological Engineering (MBEC 2014).

2. Simões R. J., Kruger M. A., Pereira W. C. A. and Teixeira C. A.. A change on Backscattered energy (CBE) simulation model to analyze the influence of heating in ultrasound data. In proceedings of the Congresso Brasileiro De Engenharia Biomédica, 2014.

Chapter 2

State of the art

2.1 Ultrasounds

Ultrasounds are mechanical waves, with frequencies above 20 kHz, thus inaudible to human hear. Ultrasounds as well as the audible sounds are the same form of energy, and thus present the same physical properties and interactions with matter.

2.1.1 Basic ultrasound physics

USs is defined by an induction of acoustic pressures waves into a medium. The acoustic wave propagation within the tissue is based in the particles movement from a rest position in the same direction as the wave is traveling. So, ultrasound waves are mechanical longitudinal waves that need a medium to propagate, and the propagation consist in compression and rarefaction zones. A rarefaction is defined by low pressure zones where particles are dispersed. As opposite, compression refers to localizations characterized by high pressures where particles are closely located. Figure 2.1 represent the wave propagation within a medium, where is possible see the compression and rarefaction zones and how they alternate between them at two different times (Figure 2.1A and B). Note

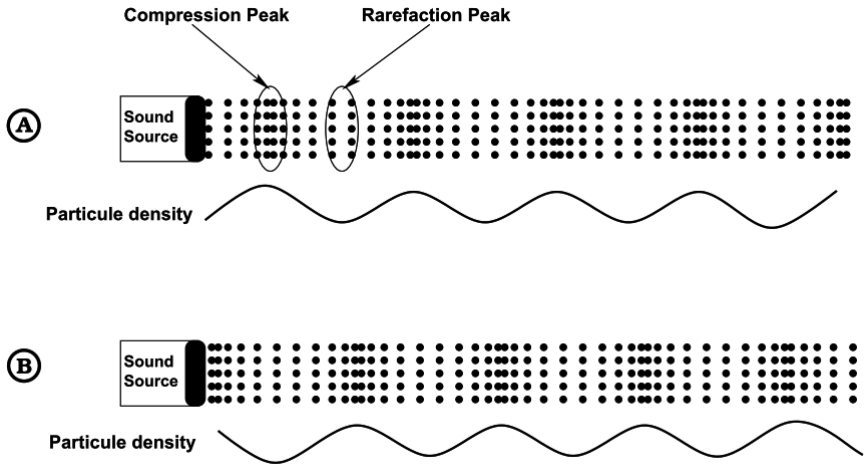

Figure 2.1: Wave propagation caused by the particle density induced by the sound source (piezoelectric transducer)at two different times, A and B. (Adapted from Figure 1-5 in [1])

that, the propagation of a sound wave from two points results from the interaction between adjacent particles, and not from the net movement of particles between these two points [1].

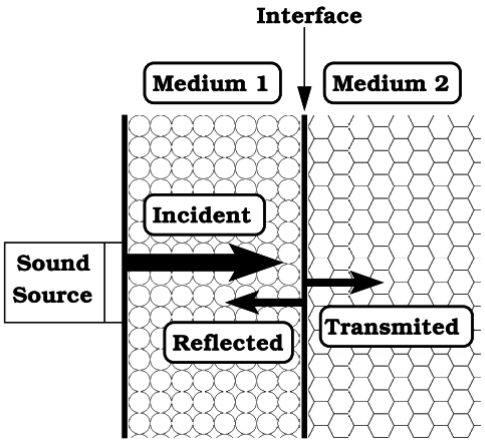

Figure 2.2: Reflection of an incident sound wave that perpendicularly hits a large and smooth interface. (Adapted from [1])

There are several processes of US interaction with the media, like: reflection, refraction, scattering, diffraction, divergence, interference and absorption. Interference is a process that increases the US wave intensity, the other processes, usually, attenuates the US intensity. Reflection is exemplified in Figure 2.2 for an interface with dimensions much larger

than the wavelength. It is exemplified that some of the energy is reflected and return to the transducer. This signal is processed and used to form images by considering the elapsed times of initial pulses and received echoes, and assuming that SOS is by default 1568 m/s in biological soft tissues [21]. One property of the mediums, and consequently, of biological tissues is the acoustic impedance (Z),in units of $kgm^{-2}s^{-1}$, is defined by:

$$Z = \rho c \tag{2.1}$$

Where ρ is the medium density (in kgm^{-3}) and c is the velocity in the medium (in ms^{-1}). Observing the equation 2.1 is possible compare it with the mechanical momentum in classical physics, where mass is substituted by density. The previous equation is extremely important, because if two mediums have the same acoustic impedance, a reflection does not happen and it is impossible to detect an interface with conventional ultrasound. The following equation define the percentage of energy that is reflected:

$$\%R = \left(\frac{Z_2 - Z_1}{Z_2 + Z_1}\right)^2 \times 100 \tag{2.2}$$

where Z_1 and Z_2 are the acoustic impedances of a medium 1 and 2, respectively.

Thus, the percentage of transmitted energy (T) is given by:

$$\%T = 100 - \%R = \left(\frac{4Z_2Z_1}{(Z_2 + Z_1)^2}\right) \times 100 \tag{2.3}$$

Rarefaction occurs if the ultrasound beam hits an interface at an angle different from 90º, as exemplified by Figure 2.3. In this situation, the direction of the incident beam is different from the transmitted one. The relation between the angle of the incident beam and the angle of the transmitted beam with the interface is given by the Snell's law:

$$\frac{\sin(\theta_t)}{\sin(\theta_i)} = \frac{c_i}{c_t} \tag{2.4}$$

Where c_i and c_t are the speeds-of-sound in the incident and transmitted medium, respectively. In the same way, θ_i and θ_t are the incident and transmitted angles, respectively. These angles are measured between an imaginary line normal to the interface, and the direction of the beams. Looking at equation 2.4, it can be concluded that, if a wave beam encounters an interface at an angle of 90 degrees, the transmitted beam travels in the same direction. When the incident angle is not 90 degrees, the transmitted beam travels by a direction given by equation 2.4.

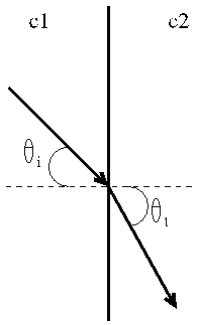

Figure 2.3: Rarefaction of a wave when travel through two mediums: 1 and 2.

Scattering occurs when ultrasound waves hit interfaces with dimensions smaller than the wavelength, causing the emission of ultrasound in all directions. A positive aspect of scattering is that it gives information about the internal texture of the tissues. The scattering effect is exemplified in Figure 2.4.

The diffraction process causes the increasing of ultrasound beam divergence with the distance from the transducer, and can be amplified when the beam passes through a small aperture with diameter smaller than the transducer face diameter. Diffraction is exemplified in Figure 2.5. Interference contributes for the increasing or decreasing of the ultrasound wave amplitude. Amplitude increases when waves with same frequency and phase interfere and cancel when waves have same frequency and opposite phase. If waves with

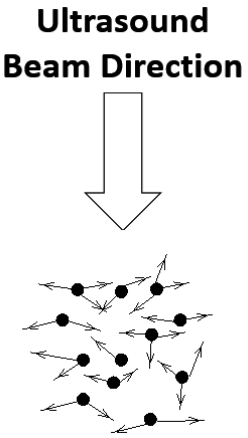

Figure 2.4: Illustration of the scattering process.

different frequency interfere, the result is a multi-frequency wave.

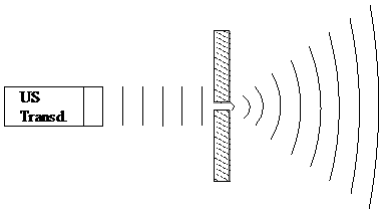

Figure 2.5: Illustration of a diffraction process.

Absorption is the process that induces heat. Sound intensity power is absorbed by the medium and release as heat. This property of heating is extremely useful for therapy purposes. Heat increasing is related with tissue properties: viscosity and relaxation time. Frequency of the ultrasound wave, also, influences the absorption. Relaxation-time is the rate at which particles return to their rest position after they are moved by the effect a wave propagation. When the relaxation time is short particles return to the original position before a new compression arrives. From the other side, longer relaxation times mean that particles do not have the necessary time to return to their original position between compression and refraction times, which means more energy is needed for a particle to invert its movement. Viscosity is a property that define the relaxation time in a medium. High viscosity means more energy to move the particles due to the molecular resistance and the result is a rapidly temperature increase. Frequency affects the time given to the

particles to return to the rest position. High frequencies leads to more upward and backward movements per time, then more friction is made and consequently, more energy is absorbed. Therefore, the rate of absorption is directly proportional to frequency [22].

The intensity of an acoustic wave is exponentially reduced as the travel path:

$$I(z) = I_0 e^{-\mu z} \tag{2.5}$$

where z is the independent variable related with distance, I_0 is the intensity at $z = 0$ (in Wcm^{-2}), $I(z)$ is the intensity at distance z from the origin, and μ is the attenuation coefficient (in Neper/cm). The attenuation is basically produced by two processes: scattering and absorption. In this way, μ can be represented by $\mu = \alpha + u$, being α the absorption coefficient and u the scattering coefficient.

2.1.2 Non-conventional Ultrasound applications

Therapeutic Ultrasound

In clinical procedures, the therapeutic ultrasound can be classified in two distinct classes: the low acoustic intensity (up to $3W/cm^2$) for physiologic and metabolic stimulation and moderate heating of tissues, and the high intensity (from $5W/cm^2$) for controlled destruction of pathological tissues. The thermal effect has several positive aspects associated: decrease joint stiffness, pain relief, changes in blood flow and decrease in muscle spasms. The use of high intensity focus ultrasound (HIFU) allows heating of a selective tissue zone. However, the lack of accurate temperature assessment methodologies and dosimetry protocols question the safety of ultrasound thermal therapies. The non-thermal effects can be non-cyclic or cyclic. Micro massages are originated by the oscillatory movements of the ultrasonic waves. The acoustic streaming in intra or extra cellular fluids is related

with the non-cyclic effect due to radiation forces. The radiation forces induce a streaming by the extracellular membrane due to changes in concentration gradients between intracellular and extracellular mediums, producing a positive change in potassium and calcium cell quantity.

Ultrasound as a non-invasive temperature estimator

The idea of estimating temperature by non-invasive methods is very attractive, since it would enable the tracking of thermal dose reducing risks and maximizing the therapy effectiveness, while minimizing secondary effects of invasive temperature measurements. In top of that, this idea would become more interesting if one could estimate temperature in real-time, with minimal errors, with low-cost and portable instrumentation. Approaches based on MRI achieved acceptable errors and real-time processing [19]. However, the MRI disadvantages, i.e., expensive instrumentation, lack of portability, and sensitivity to ferromagnetic materials, support the research for other approaches based on other technologies. In this sense, approaches based on USs received a considerable research effort in the past 20 years.

To induce and measure temperature it is necessary ultrasonic features that depend on temperature. USs have several features such as: echo-shifts due to changes in tissue thermal expansion and velocity changes; variation in the attenuation coefficient; changes in backscattered energy from tissue inhomogeneities[19].

Among the previous ultrasound features, temporal echo-shifts [23], and CBE [20] were the more studied ones. Both measures are sensitive to temperature changes because they are sensitive to the temperature-dependent changes in SOS and medium expansion/compression. Using the echo-shifts, temperature can be measured according to [23]

by the following equation:

$$\Delta T(z) = \frac{c_0}{2(\alpha - \beta)} \cdot \frac{\delta t(z)}{\delta z} \tag{2.6}$$

where $t(z)$ is the time-shift between a reference echo and the echo at a given time t and at depth z, c_0 is the ultrasound velocities before heating, α is the linear coefficient of thermal expansion and the coefficient $\beta = \frac{1}{c_0} \cdot \frac{\delta c}{\delta t}$ describes the changes in SOS with temperature. By using equation 2.6 on acquired echo-shifts, we can generate a temperature mapping, however, ultrasound velocities and α are necessary for all mediums for a correct temperature estimation; which is a limitation for the estimation on *in-vivo* scenarios.

Changes in backscattered energy (CBE) almost vary monotonically with temperature. This variation reaches 5dB for variation of temperatures in a range of 37°C-45°C. Depending on tissue inhomogeneity that causes scattering, CBE assume different behavior with temperature. If the medium is composed by lipid scatterers, CBE increases while temperature increases. If the medium is composed by aqueous scatterers, CBE decreases while temperature increases [21]. The backscattered energy signal received from a medium/tissue depends on tissue properties like attenuation and backscattered coefficient. Backscattered coefficient depends the scatterer density, the average tissue density, the variation of SOS of the scatterers and the variation SOS in the tissue. R.M.Arthur and Jason W. Trabough modeled a backscattered signal from a small volume medium with the variation of SOS's and densities of sub-wavelength scatterers and medium, where all values are referenced in [21].

$$CBE(T) = \frac{\alpha(T_R)}{\alpha(T)} \cdot \frac{\eta(T)}{\eta(T_R)} \cdot \frac{1 - e^{-2\alpha(T)z}}{1 - e^{-2\alpha(T_R)z}} \tag{2.7}$$

where T is the temperature in ^oC, T_R is the basal temperature (37°C),$\alpha(T)$ is the attenuation within the tissue volume, $\eta(T)$ is the backscattered coefficient of the tissue volume

and $z(cm)$ is the path length in the tissue volume. Backscattered coefficient is defined by [21]:

$$\frac{\eta(T)}{\eta(T_R)} = \frac{\left(\frac{\rho_m c(T)_m^2 - \rho_s c(T)_s^2}{\rho_s c(T)_m^2}\right)^2 + \frac{1}{3}\left(\frac{3\rho_s - 3\rho_m}{2\rho_s - \rho_m}\right)^2}{\left(\frac{\rho_m c(T_R)_m^2 - \rho_s c(T_R)_s^2}{\rho_s c(T_R)_m^2}\right)^2 + \frac{1}{3}\left(\frac{3\rho_s - 3\rho_m}{2\rho_s - \rho_m}\right)^2} \tag{2.8}$$

Where $\rho(kgdm^{-3})$ is the density, $c(ms^{-1})$ is the SOS of the scatterer s and the medium m. Literature presents two types of medium scatterers: a lipid-based scatterers and a water-based scatterers, both in a water-based medium. The density for lipid and aqueous scatterers are referred to be as 920 kgm^{-3} and [1050-1200] kgm^{-3}, respectively. The variation of velocity (c) and attenuation (α) with temperature was assumed to be described by the following polynomials [21]:

$$\alpha(T) \approx 0.98 - 0.03T + 0.80e^{-3}T^2 - 0.68e^{-5}T^3 \tag{2.9}$$

$$c(T)_m \approx 1533.1 + 3.06T - 0.03T^2 \tag{2.10}$$

$$c(T)_{ls} \approx 1810.7 - 13.89T + 0.10T^2 \tag{2.11}$$

$$c(T)_{as} \approx 1471.4 + 4.00T - 0.04T^2 \tag{2.12}$$

Where $\alpha(T)$, $c(T)_m$, $c(T)_{ls}$, and $c(T)_{as}$ are the temperature dependent attenuation coefficient, SOS in soft-tissue, SOS in lipid scatterers, and SOS in aqueous scatterers, respectively.

The literature representation of CBE and backscatterer energy coefficient for a standard soft-tissue with density as 1050 kgm^{-3} is represented in Figure 2.6.

The fundamental physical assumption in the thermo-responsive imaging is that temperature variations induce wave propagation changes that modify the backscattered ultrasound signals and these changes have an expression in ultrasonographic images.

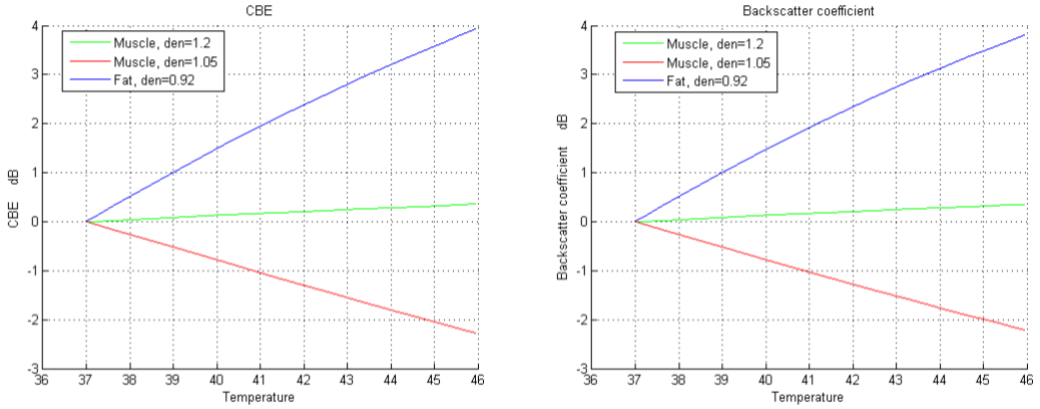

Figure 2.6: Temperature variation in range of 37°C-46°C for a) CBE and b) Backscatterer coefficient ratio.

2.2 Medical Imaging

Medical imaging refers to methodologies that allow the human interior body visualization and diagnosis. Medical imaging makes use of body physiology and anatomy to identify specific metabolisms and structures [24].

Medical imaging techniques try to use minimally invasive and intrusive techniques to acquire images, i.e., they try to disturb as less as possible the patient body.

Techniques like X-ray radiography, computational tomography (CT), magnetic resonance imaging (MRI), medical ultrasonography, single photon emission computational tomography (SPECT) and positron emission tomography (PET) are widely used in nowadays medical diagnosis. However, there are a few other techniques like optical coherence tomography (OCT), thermography, electrocardiography (ECGi) that are under development and in a near future it is expected that they could be used in diagnosis [24].

The image quality from each modality is different even in with presence of noise or artifacts. However, no type of imaging replace other, every one has its own value.

2.2.1 Computational Tomography Imaging

Overview

All imaging techniques based on X-rays are based on the absorption of X-rays as they pass through the different parts of a patient's body. Depending on the amount absorbed in a particular tissue such as muscle or lung, a different amount of X-rays will pass through and exit the body. The amount of X-rays absorbed contributes to the patient radiation dose. During conventional X-ray imaging, the exiting X-rays interact with a detection device (X-ray film or other image receptor) and provide a 2-dimensional projection image of the tissues (tomography).

X-ray computed tomography (CT) is a technology that uses computer-processed X-rays to produce tomographic images of specific areas of the scanned object.

CT images typically provide greater detail than traditional X-rays, particularly of soft tissues and blood vessels.

Although CT scans are generally safe, the patient is exposed to ionizing radiation. The amount of radiation can vary depending on the type of scanning [2].

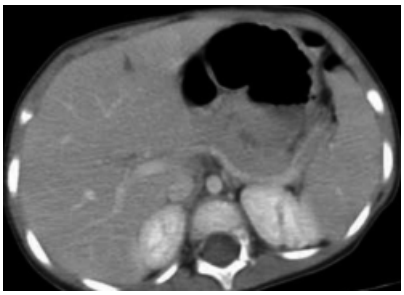

Figure 2.7: Axial plane of an abdomen CT scan. Adapted from [2]

X-ray formation

X-rays are electromagnetic radiation, typically, have a wavelength in the range of 0.01 to 10 nanometers, corresponding to frequencies in the range 30 petahertz to 30 exahertz and energies in the range 100 eV to 100 keV. X-ray wavelengths are shorter than those of UV rays and typically longer than those of gamma rays.

X-rays with photon energies above 5 to 10 keV are called hard X-rays, while those with lower energy are called soft X-rays. Due to their penetrating ability, hard X-rays are widely used to image the inside of objects[25].

X-rays are emitted using electrons and, can be generated by an X-ray tube, i.e., a vacuum tube that uses a high voltage to accelerate the electrons released by a hot cathode to a high velocity. The high velocity electrons collide with a metal target, the anode, creating the X-rays by two different atomic processes: X-ray fluorescence and Bremsstrahlung [25].

Both of these X-ray production processes are inefficient, with a production efficiency of only about one percent, and hence, to produce a usable flux of X-rays, most of the electric power consumed by the tube is released as heat [25].

Instrumentation

CT uses helical scanners that acquires a large number of X-ray projection views, i.e., the distribution of their X-ray photon attenuation characteristics. Along years, CT suffers some improvements that increased its efficiency [2]. With a helical-like CT acquisition, a X-ray tube circulates inside a gantry while a table moves continuously on gantry, allowing a continuously multislice data acquisition. Another improvement is the introduction of multi-array detectors in the CT machines. These multi-array detect and output the acquired signal. In axial mode non-helical CT acquisition, the X-ray tube circulates on gantry and the table is fixed, not allowing a continuously data acquisition. Helical CT ac-

quisition allows a faster and better resolution scanning in the axial plane. An improvement is the transition from single to multisection imaging[26], i.e., single narrow, transverse x-ray beams are conducted into a cone beam. This physical operation provides a wide range of x-rays in the receptor side. CT has some applications like CT angiography and the assessment of patients with renal colic and many routine applications such as: the detection of lung and liver lesions[27] and CT virtual colonoscopy. CT manufacturers tried to improve speeds and longitudinal anatomic coverage during a single gantry rotation. Increasing data acquisition speed provide the capacity of imaging moving organs [2]. A difficulty encountered in CT is the Compton scatter radiation reaching the detectors, and the great disadvantage of CT is the radiation dose associated with the X-ray techniques[28].

2.2.2 SPECT and PET

Overview

Nuclear medicine involves the administration of a radionuclide that emits a gamma photon. An advantage of this imaging is the variety of specific radionuclides that trigger a specific organ function that are detected with scintillation detectors. Single photon emission computed tomography (SPECT) is an imaging technique in which the gamma photons emitted are tomographed. Data acquisition is done by a system composed by a rotating gamma camera. Data acquired is processed by an image reconstruction algorithm. Likewise SPECT, positron emission tomography (PET) is a nuclear medicine imaging, which means that radionuclides are taken by tissues and metabolic processes. One of the prime reasons for the importance of PET in medical research and practice is the existence of positron-emitting isotopes of elements such as carbon, nitrogen, oxygen and fluorine that can be processed to create a range of tracer compounds with similarities to naturally occurring substances in the body. The radioactive part of the radionuclides decay with time

by emission of positrons that travels through human tissue and gives up its kinetic energy by Coloumb interactions with electrons. When the positron reaches basal energy, it starts to interact with electron by annihilation, which produces two $511keV$ anti-parallel photons [3]. The two photons produced by annihilation travel in opposite directions through the human body until they go out to the outer space (as seen in Figure 2.8), and finally reach the PET gamma camera. The information that the detector gets is the line of response (LOR), joining a pair of simultaneously activated detectors. For each slice, the measurements registered by the detectors are saved in sinograms. Sinograms show the events registered by the detectors and the distance between the corresponding LOR's and the central point of the PET scanner. The final image is, then, reconstructed from the sinogram. The final PET image shows the distribution of the absorption/accumulation of isotopes or activity level in different regions of the organs [29]. The fusion of SPECT or PET with CT or MRI[30] provides information about the patient anatomy and physiology, which is an improvement of any of those imaging. Disadvantages of this kind of imaging is the increased cost, low mobility of patient and only a physiology imaging is obtained. In addition, the patient is injected with the radionuclide, i.e., with radioactivity.

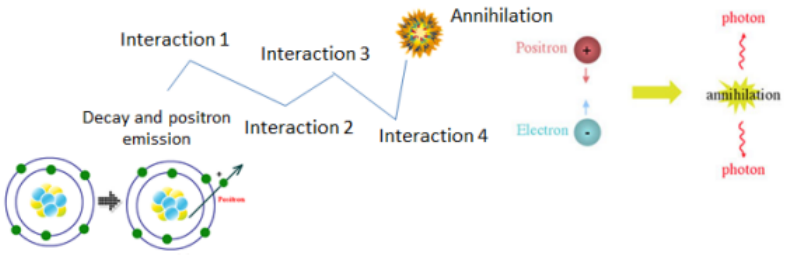

Figure 2.8: Interaction between positron and the medium particles until reach the basal energy. Then Is observed the positron/electron annihilation and the photon propagation. (Adapted from [3])

Radionuclides production

Radionuclides are used with two different purposes: imaging and radiotherapy. Radionuclides are created in accelerators (cyclotrons), where stable isotopes are bombarded with charged particles to trigger nuclear reactions. The result is the traceable instable isotopes used in radiotherapy and imaging [31].

Components of a PET system and image formation

The PET scanner allows data collection, image reconstruction and display of images. Data acquisition depends on γ-ray detection of the free photons from the radionuclides. The quantity of correct γ-ray counts influence positively the image quality of the resulting image. PET detectors count the 511 keV γ-rays, so, it is required that detectors stop this energy. For that, PET scanners use scintillations crystals coupled to photomultipliers as detectors [29].

The signal received from each scintillation crystal is amplified and filtered in order to assign an intensity proportional to the energy from the incident γ-ray (as seen in Figure 2.9).

Then, the acquired volume data is processed with 3D reconstruction algorithms, which is a very time-consuming process [4], and that is a disadvantage.

2.2.3 MRI

Overview

Magnetic resonance imaging (MRI) is an imaging technique which is based in the intrinsic magnetic properties of water protons. The interaction between polar water molecules in tissues and a magnetic fields produces a signal that carries information about the tissue

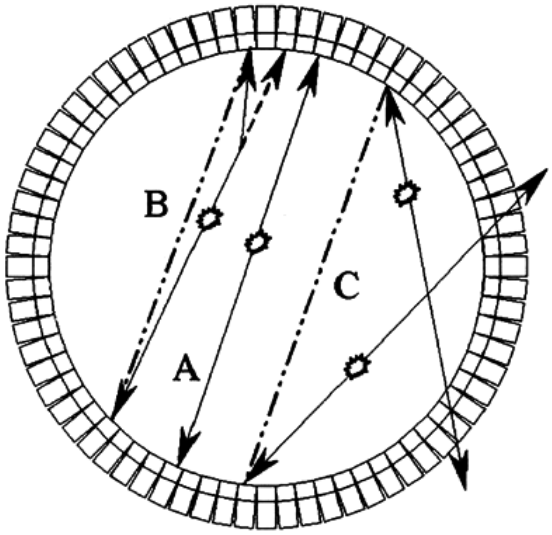

Figure 2.9: Line of response of photon pair from annihilation with the possible cases: true(A), photon scattering(B) and random event(C). (Adapted from [4])

structure [32]. When a water proton is influenced by an external magnetic field, the spin of the water proton tends to align in the same direction as the external magnetic field. This process is called *nuclear magnetic resonance*.

This process involves absorption of radiofrequency energy pulses of a certain frequency and duration by the water protons. After aligning this pulse sequence with the water protons, the protons come back to their lower energy configuration recovering their initial magnetization direction. T1 is the recovery time of longitudinal magnetization. T2 is the time decay of transverse magnetization [32]. T1 and T2 are controlled by the sequences pulses that consist of a series of RF pulses that are applied in a specific order. The time T1 and T2 influence the image contrast and that is controlled by the external magnetic filed intensity [32]. MR imaging have some disadvantages comparing with other imaging modalities: extensive costs, low accessibility, and problems with ferromagnetic materials. However, this imaging has the best resolution and it is a non ionizing imaging technique which gives Gold Standard status to MRI.

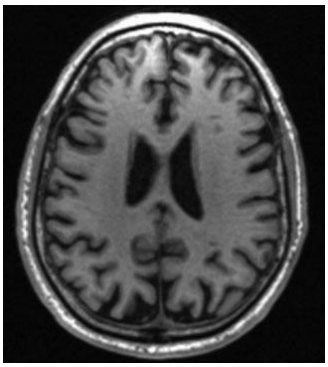

Figure 2.10: Brain axial cross-section with 1.5(T) acquisition. Adapted from [5]

MRI Principles and Instrumentation

MRI is based in the human body magnetic properties and on the fact that each type of tissue react differently to this induced magnetization that is achieved by circulating an electric signal through bundles of wires(coils). The acquired image quality and signal-to-noise ratio depends of the magnetic field intensity.Normally, the magnetic fields have 3.0(T), however the 7.5(T) intensity is coming up. Higher intensity fields represent higher resolution in images [32].

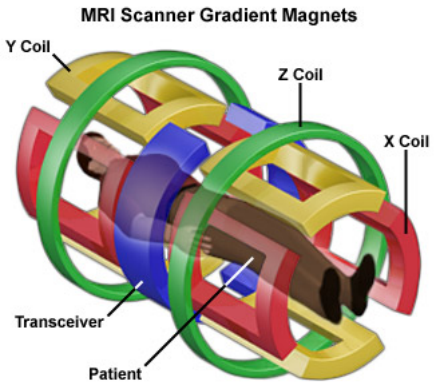

Figure 2.11: Magnet that induce the magnetic field in three coordinate axes. Adapted from [6]

It is necessary develop an adequate coil geometry to produce a uniform magnetic field. So, in recent MRI machines rectangular coils are applied, in all axes in the imaging volume. This main magnet has characteristics like field strength, field homogeneity, temporal

stability that influence the image quality. Therefore, the patient access and comfort, the minimization of fields generated outside, and the imaging environment are also dependent on the magnet properties [32].

The coils not only produce the magnetic field, but also received the modified magnetic field from the volume tissue that are converted into electric signal and converted into a image.

The resultant image should differentiate a diseased tissue from a healthy tissue. The contrast is achieved by mechanisms that produce different types of signal for the different types of tissue. The basic mechanisms depend mainly on T1 and T2 parameters [32].

With the gradient encoding from the water particles induced by the magnetization and the acquired signal from the coil, an image can be reconstructed and displayed.

2.2.4 Ultrasonographic Imaging

Ultrasounds are used in medicine for both diagnostic and therapy and nowadays are indispensable for non-invasive imaging and Doppler blood flow studies. Commercial ultrasound equipments now have frequencies ranging from 1 to 20 MHz.

A-scan mode

Amplitude mode scanning (A-scan mode) is the first ultrasonographic methodology developed and traditionally consisted on the analysis of single radio-frequency (RF) signals emitted/received by a single element transducer. More precisely, a medium is insonified by a pulsed ultrasound wave and the resulting echoes from the different interfaces can be detected. The acquired propagation direction is called line of sight [33].

A-scan RF signal strength is observed as amplitude. The A-scan displays an amplitude

signal relative to time or depth (as seen in Figure 2.12). When the signal is stronger, the amplitude increases. The signal strength refers to the various reflections originated by differences on acoustic impedance along the travel path of the ultrasound wave. Along the travel path, the waves suffer attenuation due to absorption, scattering and diffraction. To minimize attenuation, the equipments implement an attenuation correction loss that compensates the weak reflection from far sites. According to the arrival time of the spikes and on an assumed medium speed-of-sound, a distance calculation is made adding spatial information about the medium boundaries as exemplified in equation2.13.

$$v = 2d/t \tag{2.13}$$

where v ($ms-1$) is the medium average velocity propagation, d (m) is the distance where the reflection occur and t (s) is the time of flight.

The pipeline (as seen in Figure 2.12) of the A-scan ultrasound mode acquisition begins with the sending of an electric signal to the piezoelectric transducer that originates a pressure acoustic wave that insonifies the medium (Figure 2.13). At the same time, a clock count the elapsed time from the sent pulse until the received echo. Considering a average medium velocity of 1540(m/s) and given the time, a distance calculation can be made for the received echoes an, so, know where the reflections occur. When the echoes hit the piezoelectric transducer, a proportional electric signal is generated. Then, the electrical signal is processed and displayed for analysis [33]. An application of this method is the detection of structures in the eye, where irregularities echoes are detected.

B-scan mode

In a general way, B-mode refers to a two-dimensional representation of several A-mode lines. In this case the transducer is not anymore formed by a static single piezoelectric

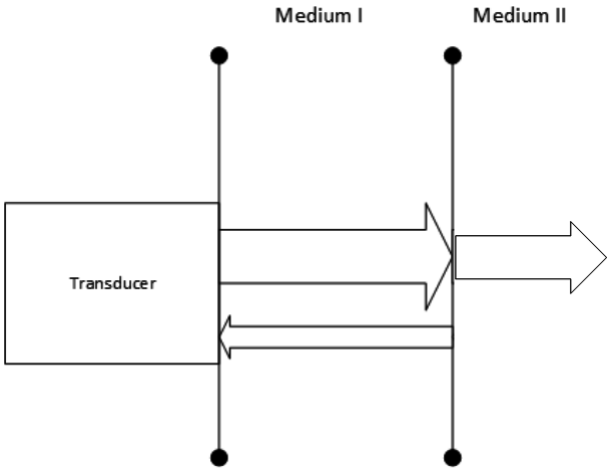

Figure 2.12: An illustration of a piezolelectric transducer with wave propagation and respective reflection in medium boundary.

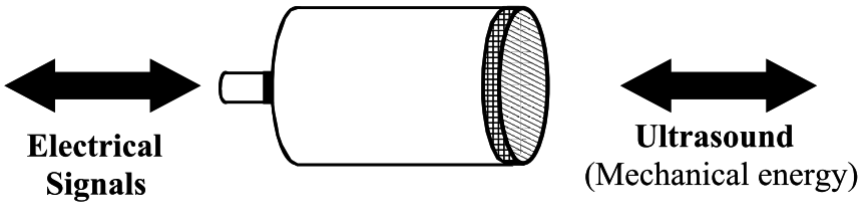

Figure 2.13: Piston-like transducer, usually applied in therapeutic US.

element, but by several elements or by a moving single element that emitted ultrasound waves at different places. (Figure 2.14). The amplitude of the received signals is represented by a brightness dot. Where the dots position represent the distance between the transducer and the reflective boundary, which is calculated by the elapsed times. Therefore, a 2D image is constructed by assign the multiple brightness dots to the respective signals set. In Figure 2.15 can be observed a set of signals with the respective B-mode image. It also can been seen that brightness dots are assigned to a stronger amplitude signal regions [33].

In an ultrasound system point of view, the image acquisition is started by a clock sequence (Figure 2.16): A pulse is generated and emitted by the piezoelectric elements. The transducer orientation coordinates are send to the scan converter. The receiving signal echoes are time-gain compensated, compressed, demodulated and filtered to define their inten-

sity. The acquired echo signals are send to the scan converter to storage with the assign arrival times and coordinate directions. When all echo signals are received, another sequence is initiated by the clock. If the clock sequences are in a increased rate, the images generated appear rapidly giving the motion sensation and structures can be followed in real-time. Thus, US has a characteristic of high temporal resolution [8; 10; 34].

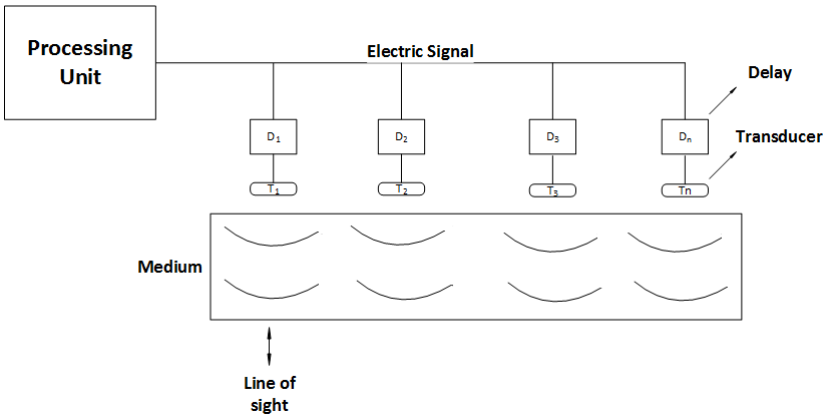

Figure 2.14: Driving of piezoelectric transducer elements aiming the acquisition of several signals necessary to form a B-mode image. Adapted from [8]

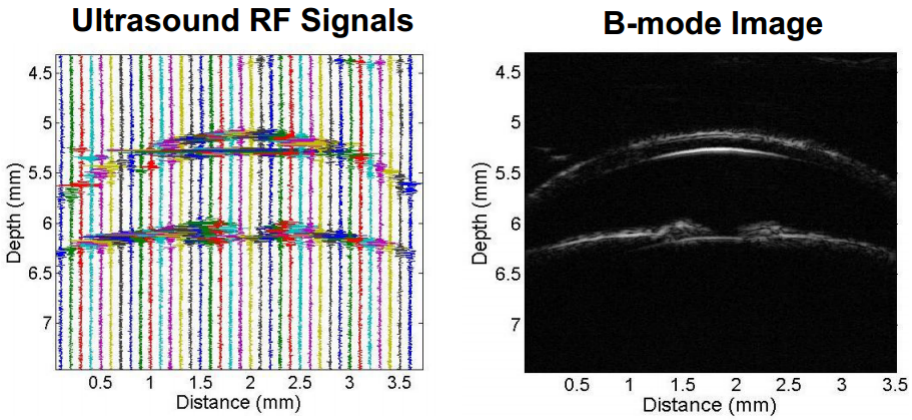

Figure 2.15: Representation of a B-mode image (on the right) and the RF signal set that leads to the formation of the image on the right(on the left). Adapted from [9]

There are two aspects that influence B-mode ultrasonography: the piezoelectric transducer position and the signal storage at right position for display. The correct position of the transducer allows the right assignment of the signal to the respective scan-line. It is crucial the storage of the correct scan-lines to avoid possible errors in dot attribution.

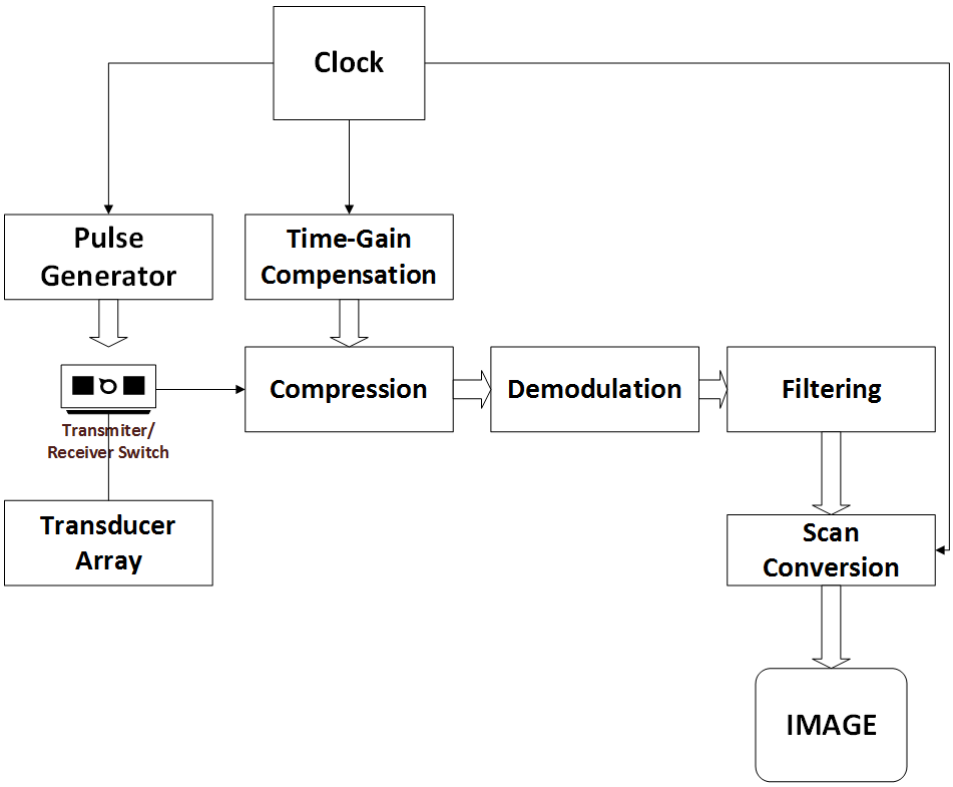

Figure 2.16: Components of an ultrasound scanner system. Adapted from [10]

Thus, it is necessary the correct storage of the signals levels at right location for the correct attribution of brightness dots location in the correct scan-line. To perform a correct scan a correct frequency slould be applied to minimize the transducer movements problems [33]

After the correct acquisition and storage of the received signal, it is necessary convert it to a digital scenario for posterior processing. The digital conversion has in account the spatial resolution which is related by the transducer width. The insonified medium is, then, divided into rectangular or square areas that are defined as pixels. Each pixel contains the proportional brightness value assigned to the local strength signal amplitude. All the pixels form a 2D matrix composed by rows and columns [33]. High values of frequency are associated with better spatial resolution and an increase of attenuation. An optimal USs imaging is achieved by the commitment between the highest frequency of the transducer for the adequate acoustic penetration to image the region of interest.

In ultrasound the signal processing is essential, because it prevents that B-mode image become all black or all white. Therefore, the continuous scan only stores maximum local amplitude values for each pixel. If the transducer detects higher values of amplitude for the same pixel with the transducer still, the value is substituted in memory, preventing the lack of B-mode brightness, once in all scan, there are various acquisitions with the same numerical value of brightness, this mechanism is called the overwrite-protect system. [33]. The Time-Gain Compensation is an algorithm for tissue attenuation compensation. The signal suffers attenuation in higher depths, and it is compensated by increasing the signal intensity in that regions, therefore, the resulting image is uniform with less artifacts. The RF compression is a technique to merge an original large pulse (characterized with poor resolution and low signal-to-ratio (SNR)) with a designed signal (p.e. the chirp signal [10]), resulting in a width decreasing in the intercorrelated signal. Thus, a better spatial resolution and SNR is obtained. Then, a demodulation is needed to extract the original information from the merged wave. The resulting signal is filtered with a low-pass filter and send to the scan converter to storage.

After the signal processing an image is achieved. This image has some characteristics like the spatial resolution and temporal resolution. As briefly cited before, the spatial resolution is related with the beam width and the pulse frequency. If the output B-mode image matrix has 512 rows and 512 columns the column is composed with 262 144 matrix elements, which means that image has the same number of pixels. The pixels dimension is calculated with the transducer-beam width, i.e., the beam width divided by number of columns gives the pixel width and the depth of the wave penetration (influenced by the pulse frequency) divided by the number of rows gives the pixels height [33].

Theoretically, a homogeneous medium should present an uniform brightness for all medium. However, that is not verified and images present different values of brightness. Analyzing the human body, there are multiple nonspecular reflections, originated by sub-wavelength

scatterers. This ultrasound scattering generates several wavefronts that merge with the main wavefront making interferences that causes brightness and darkness in the resulting image. This phenomena is called Speckle, as represented in Figure 2.17. With the speckle interference, the low brightness mediums are not detected because most of the brightness is lost. High brightness regions cover up the Speckle effect turning its effects not highly expressed in the images [33].

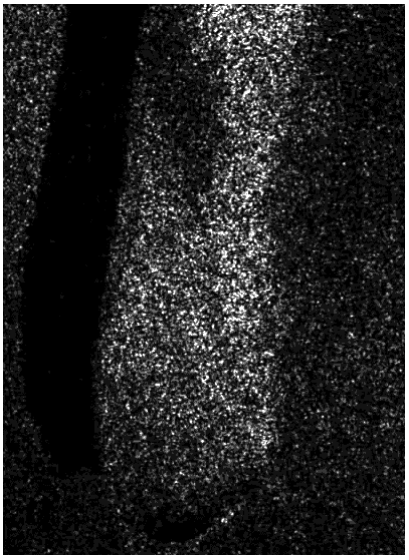

Figure 2.17: An example of the effect of speckle in a B-mode image of a human tissue. Adapted from [11]

B-mode imaging is composed by a single image with multiple lines of sight, where the wave pulse travels all the medium to inspect the interface regions and the consequent echoes are received for each line of sight. In real-time acquisition this process is repeated, which means that a series of images are memorized and viewed sequentially and rapidly giving a motion perception. After the echoes detection for each line of sight, for every line of sights, a new line of sight is created (by moving the transducer) and a new image is taken. The time for a wave travel a line of sight and back imposes the quantity of the images that could be taken: the frame rate. The usual frame rate of a scan is between 50 and 200 depending of the system specifications. The maximum number of frames, the frame rate (FR) per second (fps) is given by [33]:

$$FR = \frac{c}{2RN} \tag{2.14}$$

where c is the velocity of ultrasound in the medium, R the depth of interest, N the number of lines of sight per frame (lpf).

Equation 2.14 shows that the speed of sound is the main restriction of the FR, once, FR cannot be higher than the c. It also shows that with the scanning depth and/or numbers of line of sight are increased, the resulting FR decreases. Therefore, for a good value of FR the depth or the number of lines of sight must be reduced. However, reducing the lines of sight, the spatial resolution is affected, once, the quantity of detected information is reduced. If one reduce the analyzed depth, engaged a higher frequency of ultrasound wave, is obtained a better axial resolution. It is necessary a commitment between these factors to achieve optimal scan conditions for each situation.

C-Scan mode

C-scan mode allows the visualization of a plane of interest rejecting the undesired depths that are always present in B-mode images. Therefore, the detected times from the undesired regions are not saved in system memory, only the desired depths, calculated from the assigned elapsed times are processed. This process is achieved by gating the transducer for the specific wave detection arrival times. The gate has flexibility to select the slice location. Thus, is chosen a slice of interest with the desired orientation [33].

M-scan mode

The M-mode (motion-mode) is the ultrasonographic mode that highlights interface movement. M-mode is optimal to observe moving interfaces like the heart structures, once, usually, the movements frequency is lower than the frequency pulse rate of the ultrasound

scanner. The transducer is putted in a static position, and the scanner is set to consider focus on a single line of sight that related with the target moving interface. Converting a single line of sight into brightness dots, and adding a time dimension, it is possible create a 2D image that represent the interfaces movements through time (Figure 2.18). The white oscillatory dots correspond to the moving interface, while the static interfaces are represented by bright lines [33].

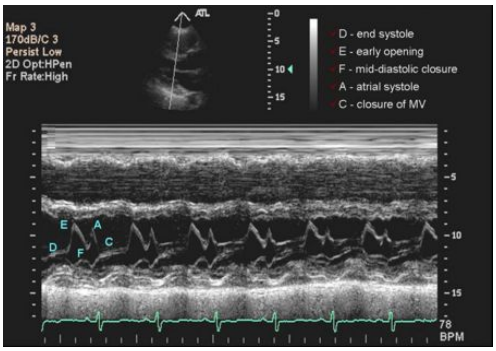

Figure 2.18: M-mode image from a heart mitral valve. Adapted from [13]

Ultrasound Doppler

Doppler effect is the change in frequency of a wave originated by the movement of an object relatively to a static observer. From the medical diagnosis point of view this effect in mainly used to monitor blood flow dynamics. Hemodynamic assessment is based on the computation of the difference in frequency between the frequency of an emitted ultrasound wave and the frequency of a received wave reflected by moving objects, which are the blood red-cells. Two main Doppler ultrasound modes can be pointed out: pulsed wave (PW) and continuous wave (CW) Doppler.

PW Doppler has the advantage of the volume imaging selection by choosing the depth respective times. The width is defined by the transducer's width. Therefore, is possible analyze, only, a region of interest with two coupled methods: with ultrasonographic imaging and the Doppler analysis. In the PW Doppler, a pulse is sent into the tissues

and reflected by a moving red cell. Thus, the echo travels back to the transducer with a different frequency, giving information about the blood movement. However, it is impossible the combination of Doppler method and the ultrasonographic acquisition at same time, once, the SOS in body is considered constant. To overcome this issue, during the acquisition the resulting image is frozen and the Doppler mode is activated. Then, the computed velocities are mapped in color, and overlapped with the frozen figure, representing the blood flux (Figure 2.19). The sensation of motion is achieved by combining these two methods in intermittent periods [33; 35]. PW is characterized for measures low flow rates, once, high flow rates causes overlapping of the echoes and consequently an aliasing in the resultant signal that induce errors in final color mapped image [35].

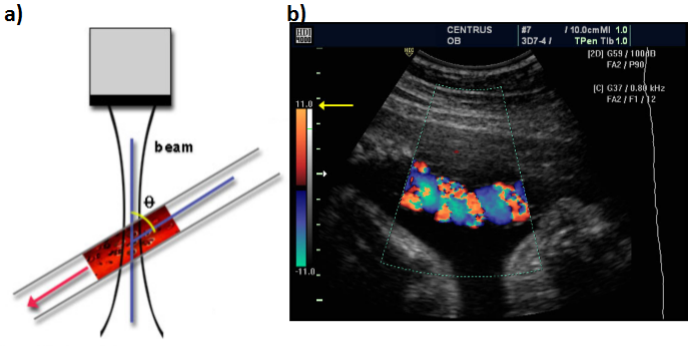

Figure 2.19: Illustration of Pulsed Wave (PW) Doppler imaging: a) represent a transducer position relatively to a blood vessel, where the beam forms an angle of θ with a blood vessel; b) represent a fetus umbilical artery flow using PW Doppler, with the flow velocity colormapped and overlapped with the related B-mode image. Adapted from [14].

Unlikely, PW Doppler, the CW Doppler send a continuous wave pulse. For that, it is used a transducer with two piezoelectric elements: one for sending and other acting as receptor, enabling the continuous reception of the ultrasound signal. As CW not applies pulsed ultrasound beams it disables echo-tracking and consequently the extraction of spatial information. CW Doppler is suited for applications where the measurement of high velocity flows are required, discarding aliasing artifacts verified in PW Doppler due to the superposition of various pulsed-waves. [33; 35].

Elastography

An emerging methodology using US is the elastography. This technique highlights the stiffness of the tissues, just like palpation, to distinguish the soft and hard sites of a medium.

Elastography does not measure, directly, the tissue stiffness but the strain, which is calculated by the displacement of the tissue (δl) divided by original tissue length (L): S = δl/L. The relation between stiffness and strain is defined by: E = stress/strain, where E is the Young's modulus traducing the stiffness [15]. The length measurements are supplied by B-mode images, where the axial displacements are measured. To obtain the axial displacements,it is applied compression and decompression of the target tissue by making pressure at the skin level with the transducer, resulting in a change of few millimeters. The resulting data, the elastogram, can be a colormap representing the strain and that can be overlapped to the original B-mode image as represented in Figure 2.20.

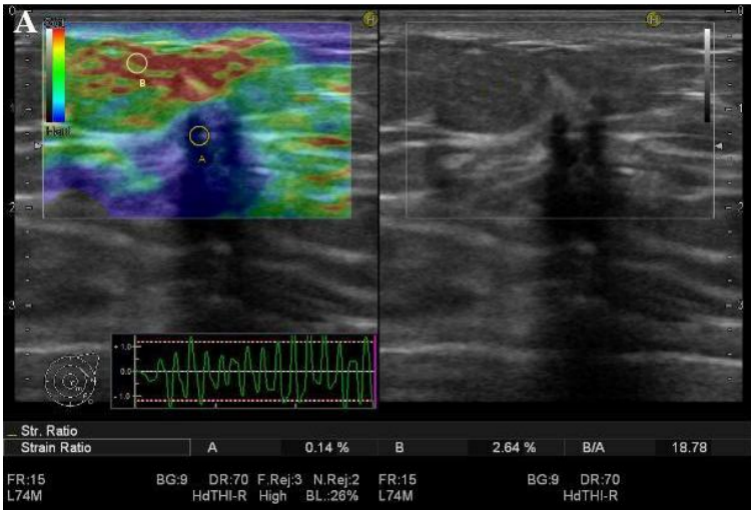

Figure 2.20: Elastography example of a tissue. It can been seen a elastogram codified as a colormap and overlapped with the B-mode image. Adapted from [15].

Pulse-inversion harmonic ultrasound imaging

The harmonic ultrasonographic imaging uses information from the second or third harmonics originated by the nonlinear distortion of the acoustic signal that insonifies a medium. The fundamental frequencies are eliminated and only those related with the harmonics are considered to form the image. The harmonic waves are produced on medium, gaining intensity with depth, until a limit depth, when their intensity starts to decreases due to attenuation (Figure 2.21) [16]. To mention that, it can be observed a harmonic merge in the detected signal. To solve this harmonic overlap, a pulse inversion of the desired harmonic is used to solve the problem. Pulse inversion of a specific harmonic block the overlapping with the other harmonics, then, is easy to detect the correct signal to produce the image. Harmonic imaging has a better axial resolution, once the harmonics have higher frequencies than the fundamental wave. The lateral resolution, also, can be better due to improved focusing with higher frequencies [16] (Figure 2.22). Also, the signal-to-noise ration is improved, once the amplitude of the harmonics are lower than the fundamental wave (Figure 2.21) which reduce the detection of echoes from undesired events, as those generated by reverberations [16; 36].

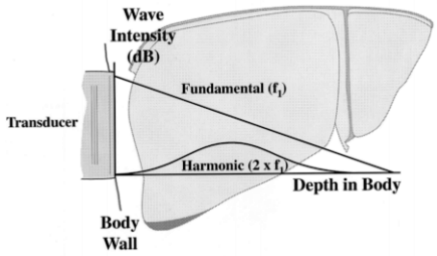

Figure 2.21: Illustration of the harmonic power evolution within the tissue versus depth. Adapted from [16].

2.3 Finite element methods (FEM)

A methodology to numerically solve many problems in physics as differential equations or boundary value problems is the finite element method (FEM).

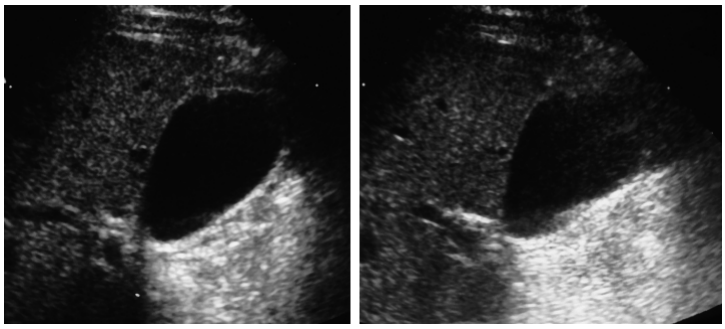

Figure 2.22: On the left side it is represented a harmonic image from a Gall-bladder polyp and in the right side is represented the conventional B-mode image. Adapted from [16].

FEM typically model electrical, mechanical, fluid and thermodynamic physics. FEM methodology consists in a set of finite elements connected at nodal points, which are located at the corners and along the sides, in the faces of the elements and within the volume. Therefore, elements fill all the geometry, never overlapping (as seen in Figure 2.23). The disposition of the elements depends on the model geometry [37] and every node has an equation assigned.

An appropriate mathematical model is a mandatory requirement to represent the physical problem. Mathematical model equations are solved for every element in a discretized way. The finite elements analysis(FEA) of complex systems usually requires the solution of a large number of algebraic equations, only this way, an effective(however, approximate) solution is achieved [37; 38]. This modeling method supplies a good strategy for understand how a given system reacts to specific initial conditions for a correct computational analysis and, consequently, the correct results. Therefore, FEM solutions are achieved with three important steps: Preprocessing, Analysis, and Postprocessing.

2.3.1 Preprocessing

The user does the preprocessing of a FEM problem. A Finite Element(FE) model must be built by first defining a geometry divided in discrete regions that are called elements.

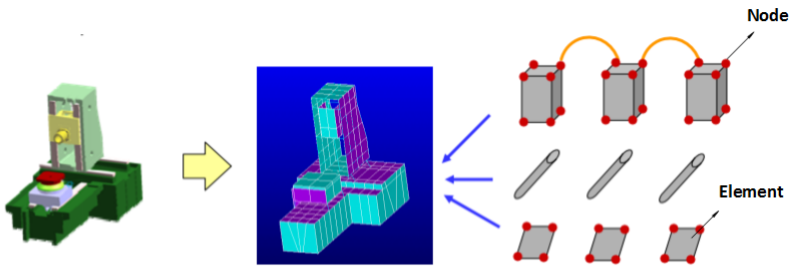

Figure 2.23: On the left the real system, on the center the Finite Element model and on the right the element and nodes that constitutes the FE. Adapted from [17]

The connection points are called nodes. The resulting set of elements creates a mesh that represents approximately the desired geometry. To facilitate the mesh creation, the FEM processors, could import a CAD files and do the conversion for mesh [37]. Another issue that fits in preprocessing is the assignment of the physics equations for each node. Therefore, it is necessary define initial conditions to the equations for the solving procedure.

2.3.2 Analysis

The FEM processor creates a matrix A from the instructions of the preprocessing. This A matrix is used to solve a system of linear equations:

$$Ax = b \tag{2.15}$$

where x is a vector with the desired variables and b is a vector with the initial conditions, i.e., given A and b, the FEM processor extract x for each node. Normally, each FEM problem has millions of nodes, which means millions of x to extract; therefore, the computation became extremely heavy. To overcome this problem there are some solvers that can be applied to solve the equation system. Solvers have a problem, while they solve, it is almost impossible to understand how they are working, and, so, they are nicknamed as ”black box” code [37].

2.3.3 Postprocessing

The postprocessing deals with the display of the results. Each node has its own result, so, the post-processor display the entire mesh, or a specific mesh selection, with the result. A resulting dataset is created with all the solutions. With the dataset is possible to create all the plots that the user wants.

2.4 COMSOL Multiphysics

COMSOL Multiphysics is a FEA, solver and simulation software for various multiphysics applications [39].

Any number of modules can be seamlessly combined to handle challenging multiphysics applications. COMSOL has the following modules:

Electrical

1. AC/DC Module
2. RF Module
3. Wave Optics Module
4. MEMS Module
5. Plasma Module
6. Semiconductor Module

Mechanical

1. Heat Transfer Module
2. Structural Mechanics Module
3. Non-linear Structural Materials Module
4. Geomechanics Module

5. Fatigue Module
6. Multibody Dynamics Module
7. Acoustics Module

Fluid

1. CFD Module
2. Mixer Module
3. Microfluidics Module
4. Subsurface Flow Module
5. Pipe Flow Module
6. Molecular Flow Module

Chemical

1. Chemical Reaction Engineering Module
2. Batteries and Fuel Cells Module
3. Electrodeposition Module
4. Corrosion Module
5. Electrochemistry Module

The simulations performed in this thesis use the fluid module: *Pipe-Flow module*; and the mechanical module: *Heat Transfer module* and *Acoustic module*.

2.4.1 COMSOL Solvers

COMSOL solves systems of linear equation problems. These equations have a significant number of unknown variables, or degrees of freedom (DOF). In general matrices may have thousands to millions of DOF's and the memory required for solving this problem is extremely expensive. It is necessary be aware of the condition number i.e., the influence

of the input argument in the final solution. COMSOL does not compute this value directly, but uses numerical methods for its estimation, instead. There are two classes of algorithms to solve functions/matrices: the direct methods and iterative methods.

Direct methods

COMSOL offers three solvers: MUMPS(Multifrontal Massively Parallel sparse direct Solver),PARDISO(Parallel Direct Sparse Solver) and SPOOLES(Sparse Object Oriented Linear Equations Solver). All of them achieve a final solution if the finite element problem is well elaborated, so, any of these solvers can be used because they are all based in LU factorization. However, there are a few differences between them that change the processing speed. To mention that, PARDISO is the fastest and SPOOLES is the slowest. Direct methods uses lot of RAM, however, PARDISO and MUMPS can store solutions in a hard disk freeing RAM space. MUMPS, also, supports cluster computing, using virtual memory to process solutions. In our simulations, we only use MUMPS and PARDISO solvers [40]. The LU factorization [41] refers to the factorization of A into two factors, a lower triangular matrix L and an upper triangular matrix U,

$$A = LU \tag{2.16}$$

as seen in the following example:

$$\begin{bmatrix} a_{11} & a_{12} & a_{13} \\ a_{21} & a_{22} & a_{23} \\ a_{31} & a_{32} & a_{33} \end{bmatrix} = \begin{bmatrix} l_{11} & 0 & 0 \\ l_{21} & l_{22} & 0 \\ l_{31} & l_{32} & l_{33} \end{bmatrix} \begin{bmatrix} u_{11} & u_{12} & u_{13} \\ 0 & u_{22} & u_{23} \\ 0 & 0 & u_{33} \end{bmatrix} \tag{2.17}$$

, where L or U is singular.

Applying this principle for solving linear equations given a system of linear equations in

matrix form:

$$Ax = b \tag{2.18}$$

given A and b, we want to extract x. After the LU factorization we obtain:

$$PA = LU \tag{2.19}$$

, where P=I for line ordering. Equation 2.19 can be rewrote as $LUx = Pb$. With this matrix equation we can solve:

$$\left\{ \begin{array}{ll} Ly = Pb & \text{for y} \\ Ux = y & \text{for x} \end{array} \right\} \tag{2.20}$$

With this arrangement COMSOL can solve the new equations by forward and backward substitutions. This way, we achieve a faster way to do the LU factorization, because with one initial Gaussian elimination we obtain the LU decomposition itself. All direct solvers are based in this process. Then in the following it is presented the specifications of the used solvers: MUMPS and PARDISO.

In MUMPS [42] solver there are three important steps for solving linear equations: (i) An matrix of equations are generated to evaluate an ordering and mapping accordingly to the given mesh (multifrontal computational graph). Then, this information is given to the processors for computation. (ii) MUMPS constructs multiple matrices that are processed in parallel. Each matrix suffers a numerical factorization. (iii) The right hand side factors derived from (ii) are saved in a vector and computed to generate a solution. These three steps combine to obtain a solution. However, they can be called separately to increase speed. If matrices are equal, the LU factorization is done just one time and this step is skipped.

PARDISO [43] solver is similar to MUMPS, it has the same three steps, however, in this

solver, for memory optimization, all matrices are released after the third step. The result is a slower solver, but with memory optimization.

Iterative methods

In our simulations, we do not use iterative methods for solving linear equations. However, we briefly describe the methodology behind this kind of methods.

The difference between direct and iterative solver, is that the solution is attained by sucessive approximations using several iterations instead of one big step. It is expected that along iterations that the solution error decreases until the attainment of an acceptable value that should be within a given tolerance range. If the error does not decreases, the simulation set up has problems and should be reviewed. Tolerance should be larger than the COMSOL precision and dictates the speed of generating solutions: if tolerance is higher, the calculated solutions are poorer but faster; if tolerance is tighter the calculated solutions have great accuracy but iterations are slower. Iterative solver are based in the conjugate gradient method.

The advantage of iterative solvers is their memory optimization, which is lower than the direct solvers methods. However, iterative solvers, do not always work, they depend on the equations used in simulations [40].

Like LU factorization, the conjugate gradient method [44; 45] obtains the numerical solutions of particular systems of linear equations $Ax = b$, where we try to find x. Choosing the p_k conjugate vectors, COMSOL estimates an approximation of the solution x, with iterative steps, i.e. modifying the conjugate vectors. In the initial step COMSOL considers

the x as x_0 and:

$$\begin{aligned} r_0 &= b - Ax_0 \\ p_0 &= r_0 \\ k &= 0 \end{aligned} \tag{2.21}$$

The algorithm searches for the correct convergence direction and the consequent residue vectors r_k and stores them in memory. The algorithm also describes that r_{k+1} is conjugate to p_i for all $i < k$ and r_k, p_k and x_k are necessary to estimate r_{k+1}, p_{k+1} and x_{k+1} in the following way:

$$\begin{aligned} x_{k+1} &= x_k + \alpha_k p_k \\ r_{k+1} &= r_k - \alpha_k A p_k \\ p_{k+1} &= rk + 1 + \beta_k p_k \\ k &= k + 1 \end{aligned} \tag{2.22}$$

The final result is x_{k+1} if r_{k+1} are within the error tolerance. The α_k and β_k are defined by:

$$\begin{aligned} \alpha_k &= \frac{r_k^T r_k}{p_k^T A p_k} \\ \beta_k &= \frac{r_{k+1}^T r_{k+1}}{r_k^T A r_k} \end{aligned} \tag{2.23}$$

The final solution is estimated and then for speed maximization can be applied a direct algorithm.

Chapter 3

Materials and Methods

3.1 Simulations

A set of simulations were made to understand the fundamental physics behind the proposed imaging technique. A simulation was based in real laboratory experiment, where temperature changes by circulating water at different temperatures in a copper coil. This experiment was used to change the temperature of a medium while B-mode images and temperature were acquired. This experiment was developed aiming to study the effects of temperature on the US, and consequently to acquire the B-mode images used in the development of thermo-responsive images. The other simulation analyses the heating by therapeutic ultrasound, which can be a feasible way to change temperature of the medium in *in-vivo* applications. On top of both temperature simulations a CBE simulations model was coupled aiming to access CBE behavior with temperature, and verify that the observed intensity changes in real images are due to CBE.

3.1.1 Simulation of heating by circulating water in a copper coil

Laboratory Experiment

In Figures 3.1 and 3.2 is showed the experimental arrangement developed that is composed by a PVC chamber that includes a copper pipe and an aluminum support that encloses the medium under study. The copper pipe is the element that transfers heat to the interior of the chamber, by recirculating water at different temperatures, and changes indirectly the temperature of the medium by changing the temperature of the water inside the chamber and of the temperature of the aluminum support.

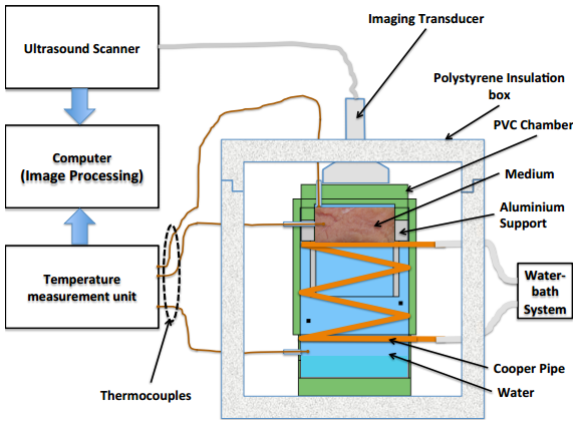

Figure 3.1: Experiment for image acquisition and temperature change. The experiment is composed by six main parts: a polyvinyl chloride (PVC) chamber (green) that contains water (blue), a cooper pipe (reddish brown) and an aluminum support (gray); a water temperature control system; an ultrasound scanner; a temperature measurement system; a computer; and a polystyrene isolation box.

The circulation of the water and its temperature inside the copper coil is controlled by a water-bath system (512-2D, Nova Ética, São Paulo, Brazil) that automatically changes water temperature by following a user-defined set point. To mention that, temperatures between 37°C and 44°C were considered, i.e., in the range used for hyperthermia. The PVC-chamber is inside a polysterene box aiming to reduce temperature losses with environment. The temperature measurement was measured at each 5-second by using

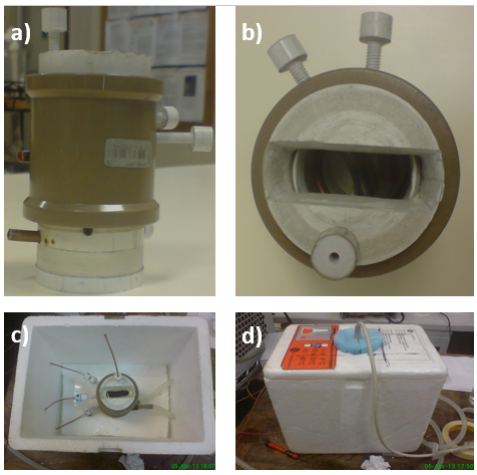

Figure 3.2: Photographies of the experimental setup developed for the temperature change based on the circulation of water by a copper coil. The PVC chamber is presented in lateral view (a) and top view (b). The top view of the opened polystyrene box is presented in c) where it is possible to observe the thermocouples connected. In d) it is presented the polystyrene box closed where its cover is used, also, to sustain the ultrasound transducer.

three J-type thermocouples : one at the bottom, other at the top and a third one in medium. The thermocouples were connected to a digital multimeter (34972A, Agilent, Santa Clara, CA, USA) that incorporates an automatic cold junction compensation (CJC) multiplexer (34901A, Agilent, Santa Clara, CA, USA). Images and the tissue temperature were recorded simultaneously as temperature changes. The images were saved by an ultrasound scanner (SonixMDP, Ultrasonix, British Columbia, Canada) as a video with 30 frames-per-second. The videos were saved in an external hard disc, and used afterwards for the development of thermo-responsive images the modeling of pixel-by-pixel intensity change with temperature. To mention that the images were acquired using a linear transducer working at 10 MHz, and the settings are left unchanged during each measurement trial.

Simulation Development

The different parts of the simulation model that reproduces the physics of the PVC chamber described previously can be decomposed in different sub-models. The coupling be-

Table 3.1: Materials and properties used in model simulation

	Dynamic Viscosity $Pa \cdot s$	Heat capacity $J/(Kg.K)$	Density Kg/m^3	Thermal Conductivity $W/(m.K)$
Inundating water	COMSOL defined	COMSOL defined	COMSOL defined	COMSOL defined
Circulating water	COMSOL defined	COMSOL defined	COMSOL defined	COMSOL defined
Lipid soft Tissue		3770	920	0.6
Aqueous soft Tissue		3770	1200	0.6
PVC		1470	1190	0.18
Aluminum		900	2700	160
Silica (absorber)		678	2320	COMSOL defined

tween these models are presented in Figure 3.3. To mention that the CBE simulation model is described in Section 3.1.3, as it is the same for both simulations.

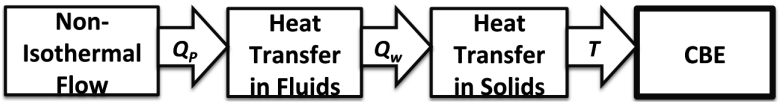

Figure 3.3: Coupling between the different models. Where Q_P is the heat source from the cooper pipe, Q_W, is the transferred heat from the water in the PVC chamber to the aluminum and the medium, and T is the temperature.

Simulation geometry

The simulation modeling is identical to the real PVC chamber, including all physical measures, material properties and the physical processes involved in the real experiment. The PVC chamber geometrical details are depicted in Figure 3.1 and Figure 3.4 represent its external geometry. The PVC chamber geometry was developed based on a CAD structure in the COMSOL geometry node. We use the dimension data and material properties from Table 3.1 and Table 3.2, both based in the real apparatus.

COMSOL Pipe-flow module

Table 3.2: Real experiment dimensions that were used to develop the geometry of the COMSOL simulations.

Experiment piece	Measures (cm)
PVC piece	
Height	18.5
Internal Diameter	44
Wall	0.15
Copper pipe	
External Diameter	0.63
Internal Diameter	0.4
Principal tube	
Internal diameter	6.005
External diameter	6.9
Height	7.6
Aluminum ring	
External diameter	0.925
Step height	1.15
Total height	4.27
Number of turns	3 turns
Base	
Base height	3.43
Distance from aluminum to bottom	3.56
External diameter	6.0
Top	
Internal step height	1.4
External step height	1.2

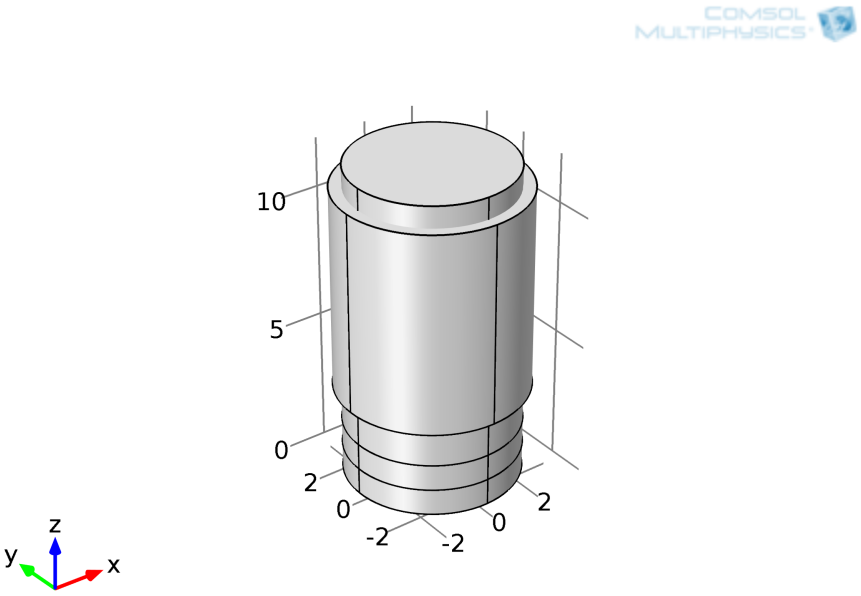

Figure 3.4: External COMSOL geometry of the PVC chamber.

After the definition of the simulation geometry and material properties, we introduce the physical phenomena. For the developed simulations, we assumed that: the chamber does not exchange heat with the outside environment; the other parts of the experiment were assumed to be ideal, and that they supplied the required inputs to the chamber system, and had no influence on it; temperature change is the main system input and was simulated by assuming a constant flow of water that enters in a spiral-shaped cooper pipe at a known temperature. COMSOL provides a Non-Isothermal Pipe Flow physics module that simulates water fluxes in pipes. The circulating water in the pipe is Newtonian. In Newtonian fluids, tension is directly proportional to the deformation rate of the fluid [46]. Afterwards, the physical laws that dictate the influence of the circulating water inside a cooper pipe are the mass, the momentum and the energy conservation. The equations that describes the process are described below [46; 47]:

$$\frac{\partial A\rho}{\partial t} + \nabla_t \cdot (A\rho u) = 0 \tag{3.1}$$

$$\rho\frac{\partial u}{\partial t} = -\nabla_t p - f_D\frac{\rho}{2d_h}u|u| \tag{3.2}$$

$$\rho A C_p\frac{\partial T}{\partial t} + \rho A C_p u\cdot\nabla_t T = \nabla_t\cdot Ak\nabla_t T + f_D\frac{\rho A}{2d_h}u^3 + Q_P \tag{3.3}$$

where $A(m^2)$ is the pipe cross-section, $u(ms^{-1})$, is the water average velocity in pipe, $p(Nm^{-2})$, is the water pressure within the pipe, $T(K)$, is the water temperature in the PVC chamber and $C_p(Jkg^{-1}K^{-1})$ and $k(Wm^{-1}K^{-1})$ are the water heat capacity at constant pressure, and the thermal conductivity respectively. The term Q_P from equation 3.3, is the heat source from the pipe. In *Heat transfer in fluids*, we explain the heat source.

The term $-f_D\frac{\rho A}{2d_h}u^3$ from equation 3.3 describes the heat dissipated due to internal friction in the fluid. *Non-Isothermal Pipe Flow* module from COMSOL uses the Churchill model to simulate the Darcy friction factor, f_D, between the pipe and the water. This Churchill model is suitable for various scenarios of fluxes: laminar flux, turbulent flux and the transitional zone between both [46]. The Churchill friction model imposed by *Non-Isothermal Pipe Flow* module is:

$$f_D = 8\left(\left(\frac{8}{Re}\right)^{12} + (A+B)^{-\frac{3}{2}}\right)^{1/12} \tag{3.4}$$

where:

$$A = \left(-2.457\ln\left(\frac{7}{Re}\right)^{0.9} + 0.7(e/d)\right)^{16} \tag{3.5}$$

$$B = \left(\frac{37530}{Re}\right)^{16} \tag{3.6}$$

The Darcy friction factor f_D depends on roughness (e) of the pipe divided by its diameter $d_i(m)$. Looking at Darcy friction model equation 3.4, we see that is a function of fluid properties (ρ, μ), flux velocity (u) and pipe geometry (d_i). All of these properties are

describe by the Reynolds number [46]:

$$Re = \frac{\rho u d_i}{\mu} \tag{3.7}$$

where $\rho(kgm^{-3})$ is the water density, $u(ms^{-1})$ is the water average velocity, $d_i(m)$ is the pipe inner diameter and $\mu(Pa \cdot s)$ is the water viscosity. COMSOL provides all the necessary tools to simulate fluid fluxes in pipes, and all the necessary fluid properties [47].

COMSOL Heat transfer in fluids module

The water circulates inside of the spiral pipe with a certain temperature. In the real experiment the water temperature inside the cooper pipe is regulated externally by a water-bath system. With COMSOL we simulate this behavior by defining the temperature at which the water enters in the pipe. The simulated heating is achieved by another physics module from COMSOL named *Heat transfer in fluids*. This module coupled with *Non-Isothermal Pipe Flow module*, enables the heating simulation in the PVC chamber. However, this heat transfer and the fluid friction with itself and the pipe, implies a small loss of temperature inside the pipe, which is compensated by the water bath-system. This phenomena is characterized by [48]:

$$\rho A C_p \frac{\partial T}{\partial t} + \rho A C_p u \cdot \nabla_t T = \nabla_t A k \nabla_t T + f_D \frac{\rho A}{2 d_h} |u|^3 + Q_P \tag{3.8}$$

where $A(m^2)$ is the pipe cross-section, $u(ms^{-1})$, is the water average velocity in pipe, $C_p(J \cdot Kg^{-1} \cdot K^{-1})$ is the heat capacity at constant pressure, $T(K)$, is the temperature in the pipe and $k(W \cdot m^{-1} \cdot K^{-1})$ is the thermal conductivity. The second term from the right hand-side from equation 3.8 present the dissipated heat due to internal friction of the fluid. We neglect this term [47] (see equation 3.9). Rearranging equation 3.8, the heat

transfer happens due to convection and it is defined by [48]:

$$\rho C_p \frac{\partial T}{\partial t} + \rho C_p u \cdot \nabla_t T = \nabla_t k \nabla_t T + Q_P \tag{3.9}$$

where $C_p(J \cdot Kg^{-1} \cdot K^{-1})$ is the heat capacity at constant pressure, $T(K)$, is the water temperature in the PVC chamber and $k(W \cdot m^{-1} \cdot K^{-1})$ is the thermal conductivity. The second therm of the right-hand side of equation 3.9, Q_P, is the heat source from the pipes. The couple term Q_P is defined by COMSOL. This heat transfer is, then, defined by:

$$Q_P = hz(T - T_P) \tag{3.10}$$

where $z(m)$ is the pipe perimeter, $h(W \cdot m^{-2} \cdot K^{-1})$, is the heat transfer coefficient, $T(K)$, is the water temperature in the PVC chamber and $T_P(K)$, is the water temperature in the pipe. The heat source power from pipes is directly proportional to the biggest difference between the temperatures (as seen in difference between temperatures in equation 3.10), i.e., if the temperatures are equal, $Q_P = 0$. Equation 3.10 shows a term, h, the heat transfer coefficient. This coefficient depends on water properties and from pipe flux nature. Through Nusselt number, we can define as h [46]:

$$h = Nu \frac{k}{d_i} \tag{3.11}$$

where, $k(W \cdot m^{-1} \cdot K^{-1})$ is the thermal conductivity from the fluid, Nu is the Nusselt number and $d_i(cm)$ is the inner diameter of the pipe.

The flux type is detected automatically by COMSOL. For laminar flux, $Nu = 3.66$ for circular pipes [46]. For turbulent flux, Nu is defined by [46]:

$$Nu = \frac{\frac{f_D}{8}(Re - 1000)Pr}{1 + 12.7(\frac{f_D}{8})^{1/2}(Pr^{(2/3)} - 1)} \tag{3.12}$$

where Pr is the Prandtl number, f_D is the Darcy friction factor and Re is the Reynolds number. The Prandtl number Pr is defined by [46]:

$$Pr = \frac{C_p \mu}{k} \tag{3.13}$$

where $k(W \cdot m^{-1} \cdot K^{-1})$ is the thermal conductivity from the water,$C_p(J \cdot Kg^{-1} \cdot K^{-1})$ is the heat capacity at constant pressure and $\mu(Pa \cdot s)$ is the water viscosity.

COMSOL Heat transfer in solids module

We simulated changes in temperature in the aluminum and in the medium, imposed by changes in the water in the chamber. In solids, heat transfer is done by conduction, as expressed by [48]:

$$\rho C_p \frac{\partial T}{\partial t} = \nabla_t k \nabla_t T + Q_W, \tag{3.14}$$

where $Q_W(Wm^{-1})$, is the transferred heat from the water in the chamber to the solid structure. The heat transfer is mediated again by coupling two modules from COMSOL: *Heat transfer in Fluids* and *Heat Transfer in Solids*.

3.1.2 Simulation of heating by therapeutic ultrasound

The different parts of the model, and their coupling are presented in Figure 3.5, and are described in the next sub-sections.

Figure 3.5: Coupling between the different models. Where I is the Intensity magnitude from pressure acoustics and T is the temperature.

Simulation Design

Model Geometry

This simulation uses acoustics pressure to increase temperature as described in Section 2.1.2. It is simulated a transducer that induces an acoustic pressure field in a medium surrounded by water. Three cylinders compose the model, the top cylinder represents the transducer, the middle represent the tissue sample and the third one represents the surrounding water (as seen in Figure 3.6). The measurements of the physical dimensions of the transducer and sample are presented in Table 3.3.

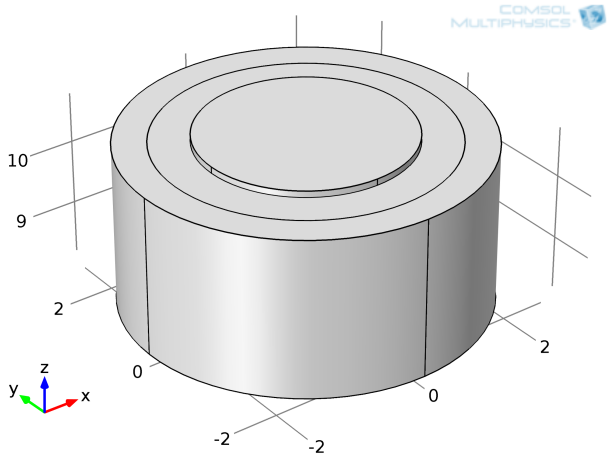

Figure 3.6: External geometry of the simulation of heating by therapeutic ultrasound, where the top cylinder represent the transducer, the middle cylinder the sample and the outsider cylinder represent the surrounding water.

Pressure Acoustic module

In this section, we simulate a model that allows a medical field approximation with therapeutic US. We simulate a transducer to induce acoustic pressure into a medium. COMSOL uses *Pressure Acoustic in Frequency Domain* physics to model the stationary acous-

Table 3.3: Dimensions defined for the simulation developed for medium heating by therapeutic ultrasound.

Experiment piece	Measures (mm)
Transducer	
Height	10
Diameter	18
Surrounding water	
Height	27.5
Diameter	44
Sample	
Height	25
Diameter	40

tic field to obtain the acoustic intensity distribution in the sample tissue. The sample has irregular mediums geometries developed in the COMSOL embedded functions to simplify the simulation and ease the computer processing. The intensity acoustic energy is solved and used as heat source input in *Bioheat Transfer* physics model. The Helmholtz equation describe the wave propagation in 3D cylindrical coordinates [49]:

$$\frac{\partial}{\partial r}\left(\frac{r}{\rho_c}\left(\frac{\partial p}{\partial r}\right)\right)+r\frac{\partial}{\partial z}\left(-\frac{r}{\rho_c}\left(\frac{\partial p}{\partial z}\right)\right)-\left(\left(\frac{\omega}{c_e}\right)^2\right)\frac{rp}{\rho_c}=0 \tag{3.15}$$

where r and z are radial and axial coordinates, $p(Nm^{-2})$ is the acoustic pressure, and $\omega(rad\cdot s^{-1})$ is the angular frequency. $\rho_c(kg\dot{m}^{-3})$ is the medium density, $c_e(ms^{-1})$ is the SOS in the medium. Using equation 3.15 involves the assumption that the acoustic wave propagation is linear and also that the amplitude of shear waves in the medium are much smaller than the pressure waves [49]. The heat source Q for thermal simulation, given in the plane wave limit, is then calculated as [49]:

$$Q=2\alpha_{abs}I=2_{abs}\left|Re\left(\frac{1}{2}pv\right)\right| \tag{3.16}$$

where α_{abs} is the absorption coefficient, $I(Wm^{-2})$ is the acoustic intensity magnitude,

$p(Nm^{-2})$ is the acoustic pressure, and $v(ms^{-1})$ is the acoustic particle velocity. The heat source $Q(Wm^{-3})$ is the coupled term calculated by COMSOL during the *Pressure acoustics* physics module analysis.

Bioheat transfer module

Heat transfer in biological tissues could be simulated in COMSOL by the Penne's equation [47]: Inserting the volumetric acoustic heat source into the Penne's Bioheat Transfer equation to model heat transfer (Q) within biological tissues gives [47]:

$$\rho C_p \frac{\partial T}{\partial t} = \nabla \cdot (k \nabla T) - \rho_b C_b w_b (T - T_b) + Q + Q_{met} \tag{3.17}$$

where $T(K)$ is the temperature, $\rho(kg \cdot m^{-3})$ is the density, $C_p(J \cdot Kg^{-1} \cdot K^{-1})$ is the medium heat capacity at constant pressure, $k(W \cdot m^{-1} \cdot K^{-1})$ is the medium thermal conductivity, $\rho_b(kg \cdot m^{-3})$ is the density of the blood, $c_b(J \cdot K^{-1})$ is the blood specific heat, w_b is the blood perfusion rate, $T_b(K)$ is the blood temperature, $Q(Wm^{-2})$ is the coupled heat source from equation 3.16 and $Q_{met}(Wm^{-2})$ is the metabolic heat source.

3.1.3 CBE simulation

We implemented the CBE equations 2.7 and 2.8 from literature in COMSOL, and generate CBE solutions over time, space and temperature. The temperature variations obtained from the *Heat Transfer* modules (in fluids, solids and using the bioheat transfer equation) and the information referred above concerning densities, velocities and attenuation provide all the necessary information to compute CBE. To simulate heterogeneous media, we defined specific medium geometries with specific characteristics, i.e., with different types of scatterers.

We associate the geometrical domain to the respective density and velocity of the tissue scatter, i.e., the introduced domain has a specific density that could be $\rho_{lip} = 0.92gcm^{-3}$ or $\rho_{aq} = 1.05gcm^{-3}$ and a velocity $c(T)_{ls}$ or $c(T)_{as}$ defined by polynomials 2.11 and 2.12, respectively. This association is made by if cycles: For densities we have:

$$\begin{aligned} &if dom == x \\ &\qquad \rho = \rho_{lip} \\ &else \\ &\qquad \rho = \rho_{aq} \\ &end \end{aligned} \tag{3.18}$$

For velocities we have:

$$\begin{aligned} &if dom == x \\ &\qquad v(T) = c(T)_{ls} \\ &else \\ &\qquad v(T) = c(T)_{as} \\ &end \end{aligned} \tag{3.19}$$

where x correspond to the lipid domain geometries. The temperature do not has a uniform distribution in all of simulation model, so, we need to acquire various temperatures from different points of the sample to compare with real experiment. This way, we can apply statistical methods over the acquired data and conclude about them. The temperature probes are randomly distributed in sample.

After experience simulations, solutions are generated for all the element mesh points. Thus, we can observe the variation of CBE with temperature in a specific time.

3.1.4 COMSOL Mesh/model simulation mesh

It is computationally impossible the application of the previous equations to a geometry with an infinity number of elements, thus it is necessary discretize the geometry domains. To do so, COMSOL has a module that discretizes the geometry in small geometric solids named mesh elements. The mesh elements could have some defined forms: hexahedrons, tetrahedrons, prisms or pyramid whose faces, edges, and corners are respectively, mesh faces, mesh edges and mesh vertices [47]. Pyramid elements are ideal to mesh sharp domain edges, like our sample domains, once, triangle angle from mesh faces have a low angle that allow the meshing of sharp geometries. In COMSOL it is possible to choose between two techniques for a geometry meshing: an automatic mode designated Physics Controlled Meshing or a manual mode designated User-controlled Meshing. We used the automatic mode Physics Controlled Meshing to avoid possible errors and to optimize the meshing process. This method, automatically, adapts physical process characteristics from simulation and the geometry to mesh for the Pipe-flow heating simulation. Even though this being an automatic process, COMSOL lets change the element mesh size. Thus, we obtain a specific size of mesh elements adapted to our needs. In the heating by therapeutic ultrasound simulation, for a fully user-defined optimization , we use the User-controlled to discretize the sample at the sub-wavelength level, i.e., we want to sequence the meshing process where mesh elements have a sub-wavelength size in the medium geometry. We use a tetrahedral free mesh with the following size condition: c/f0, where $c(ms^{-1})$ is the medium speed-of-sound and $f_0(Hz)$ is the transducer frequency. A tetrahedral free mesh generates an unstructured mesh of tetrahedrons, where the number of elements existent is controlled by the distribution and size of the mesh elements on the geometry. The meshes of each simulation are represented in Figure 3.7.

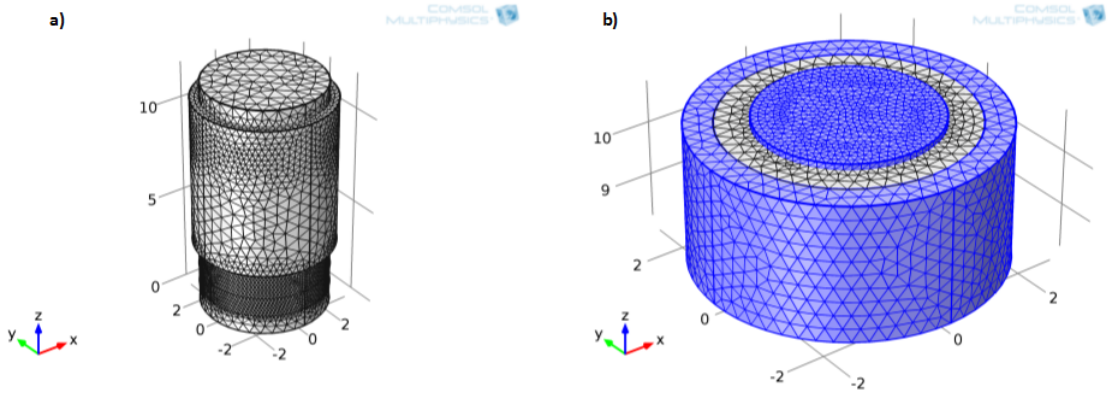

Figure 3.7: Model mesh for the two simulations. a)PVC chamber temperature change simulation mesh. b) Therapeutic ultrasound heating simulation mesh.

3.2 Development of thermo-responsive images

In a first analysis, we observed that the variations of intensity at the pixel level describe: linear, quadratic, and increasing and decreasing variations with temperature (as predicted by the CBE equations). Thus it was decided to describe these variations by linear and quadratic polynomial models, and also by a correlation analysis. In a more detailed analysis we observed that oscillations appeared in some pixels, which are not explained by the present CBE equations. Although, the present CBE model did not account this we decided also to model these oscillations and observe the regions where they happen. So, we considered a fourth type of models that are derived from the linear time invariant (LTI) system identification theory, and consisted on the modeling of an input/output relation by a second order transfer function, where two main parameters can be extracted: the damping ratio (ξ) and the undamped natural frequency (ω_n). After fitting/modeling, the parameters from the polynomial models, the signal of the correlation analysis, and the parameters from the second-order system identification theory obtained for each pixel were represented. The process of thermo-responsive image formation is presented in Figure 3.8.

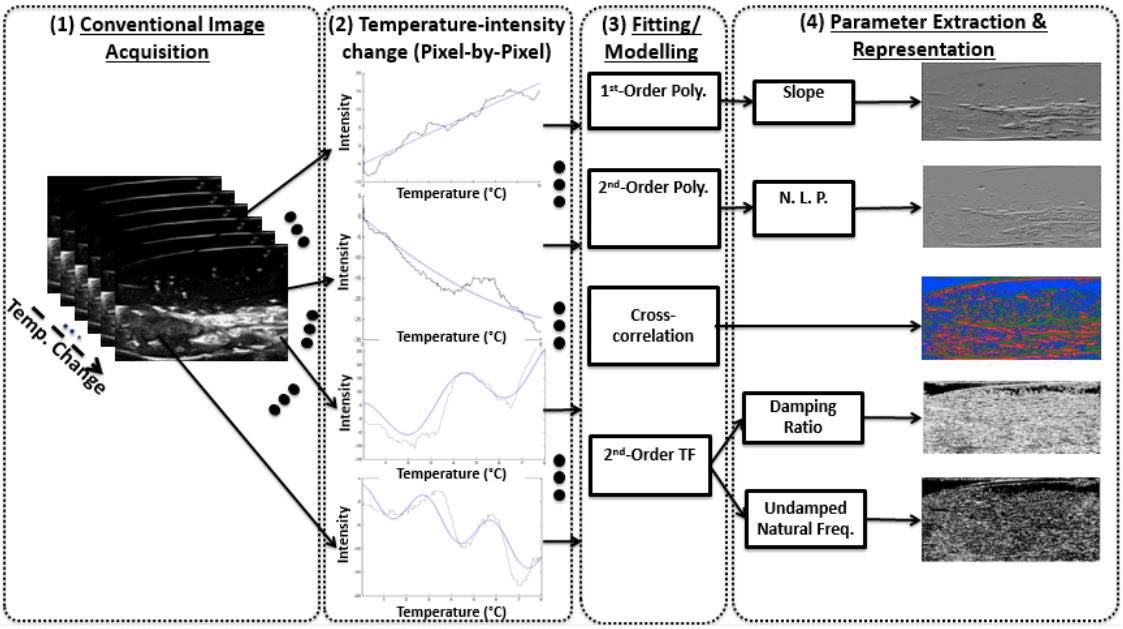

Figure 3.8: Thermo-responsive images formation. (1) Data acquisition during a temperature change; (2) Computation of the relation "grayscale level intensity-temperature". (3) Modeling of the acquired US B-mode imaging relation by applying three representation strategies: polynomials, cross-correlation, and second-order transfer function modeling. (4) Representation and extraction of a thermo-responsive model parameter originating different thermo-responsive images.

3.2.1 B-mode data pre-processing

Before applying the data collected using the experimental setup described in Section 3.1.1, intensity variations must be extracted from the acquired B-mode images. As referred the images were acquired at a rate of 30 frames per second (fps) and stored as a video file (.avi), and temperatures were saved at each 5-second. So, aiming to relate each temperature value with one intensity value, we averaged images in packets of 5-seconds, i.e., 150 images(30fps $\times$ 5s = 150) were averaged. To mention that this averaging process helps the attainment of improved results, given that it eliminates noise and artifacts from the images. Artifacts from each frame could not appear in the other frames, this way, and the average from all frames, attenuate the possible artifacts. The retrieval of the images from the video was performed using the *mmread* Matlab function from Micah Richert [50].

The function enables the image retrieval by passing as argument the indexes of the required images or the time interval relative to the beginning of the video recording. The pixels in each image were represented as an RGB vector that needed to be converted to a unique gray-level value. The Matlab function *rgb2gray* was used for this purpose. At the end each averaged gray scale image is a matrix with M×N pixels.

3.2.2 Modeling/fitting details

- Polynomial models

    1. First-order polynomial model

       The linear polynomial model is a first order polynomial with the equation: $lin_{m,n} = a_{m,n}T + b_{m,n}$. Where $lin_{m,n}$ is the temperature dependent intensity for the pixel at position (m,n), T is the temperature, and $a_{m,n}$ and $b_{m,n}$ are the model parameters to be found for the pixel at location (m,n). Here the values of a and b are found by a linear least square optimization using the Matlab function *polyfit*. The resulting thermo-responsive linear image is created by plotting the parameter a for each pixel.

    2. Quadratic polynomial model

       The quadratic polynomial model is a second order polynomial with the equation: $quad_{m,n} = a_{m,n}T^2 + b_{m,n}T + c_{m,n}$. Where $quad_{m,n}$ is the temperature dependent intensity for the pixel at position (m,n), T is the temperature, and $a_{m,n}$,$b_{m,n}$ and $c_{m,n}$ are the model parameters to be found for the pixel at location (m,n). Here the values of a, b and c are found by a least square optimization. The resulting thermo-responsive linear image is created by plotting the parameter a for each pixel.

- Cross-correlation

The intensity change is cross-correlated with the temperature change, and the correlation coefficients matrix computed by employing:

$$R_{m,n}(i,j) = \frac{C_{m,n}(i,j)}{\sqrt{C_{m,n}(i,i)C_{m,n}(j,j)}} \tag{3.20}$$

Where $C_{m,n}$ is the covariance between the temperature and the intensity for the pixel at the (m,n) position. As we are correlating two variables $R_{m,n}(i,j)$ is a 2×2 symmetric matrix with ones in the principal diagonal, corresponding to the autocorrelation of the temperature and intensity sequences, respectively. $R_{m,n}(2,1) = R_{m,n}(1,2)$ is the correlation coefficient between the intensity and temperature.

- Second order transfer function modeling

The modeling of the intensity-temperature relation by a second order transfer function was performed using the *tfest* Matlab function [51] that makes continuous-time transfer function estimations from sampled data. This function receives as important parameters the data to be modeled, the number of poles, the number of zeros and the delay between the system input and output. The function returns the identified transfer function as a structure that contains the coefficients of the numerator and denominator. The generic continuous transfer function estimated by tfest is [52]:

$$G(s) = e^{-\tau s}\frac{b_n s^n + b_{n-1}s^{n-1} + ... + b_0}{s^m + a_{m-1}s^{m-1} + ... + a_0} \tag{3.21}$$

where τ is an arbitrary delay, $b_0, ..., b_n$ are the coefficients of the numerator polynomial and $a_0, ..., a_{m-1}$ the coefficients of the denominator polynomial. In this, we estimate a second-order transfer function without delay and just with poles. So the

previous equation becomes:

$$G(s) = \frac{b_0}{s^2 + a_1 s + a_0} \tag{3.22}$$

The standard prototype transfer function of a generic second order control system with unit steady-state gain is given by:

$$G(s) = \frac{\omega_n^2}{s^2 + 2\xi\omega_n s + \omega_n^2} \tag{3.23}$$

So, by association we can say that $\xi\omega = a_1$, and $b_0 = a_0 = \omega_n^2$, becoming the values of the natural undamped frequency (ω_n) and the damping ratio (ξ) for the pixel at coordinates (m,n) given by:

1. $\omega_{m,n} = \sqrt{a_0}$
2. $\xi_{m,n} = \frac{a_1}{2\sqrt{a_0}}$

3.3 Methods Summary

We developed two simulation models to analyze the changes in CBE due to temperature changes imposed by circulating water inside a copper coil and due to temperature changes caused by therapeutic ultrasound heating. We acquired also B-mode images from *ex-vivo* tissue samples where we observed intensity variations due to heating, and that are related with CBE (as seen in Figure 3.9), as it will be presented in the results section. The intensity variations were modeled by different approaches, turning possible to develop thermo-responsive images.

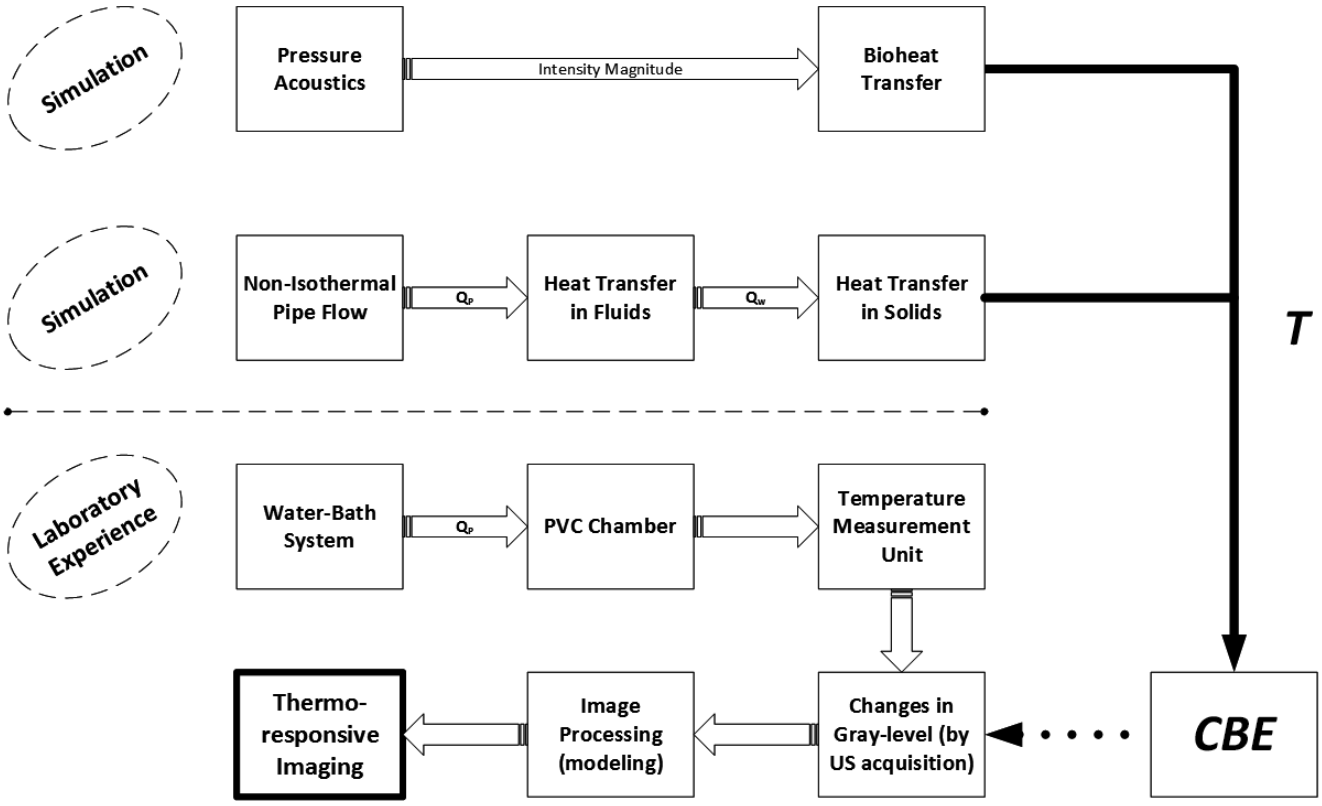

Figure 3.9: Method diagram

Chapter 4

Results

4.1 Simulations

4.1.1 Simulation of heating by circulating water in a copper coil

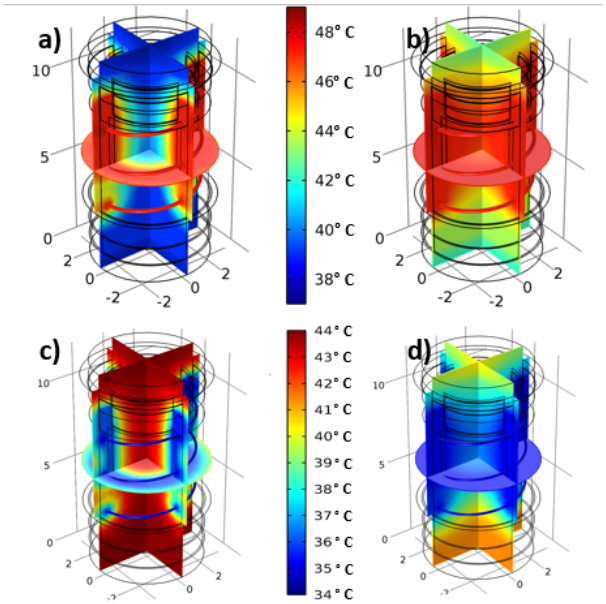

Figure 4.1: Multi-slice view of the simulated temperature profile at different time instants in the PVC chamber. a) heating at 900s; b) heating at 2280s; c) cooling at 600s ; and d) cooling at 1980s.

Considering the heating by circulation water by a copper pipe simulation, first, we try to reproduce the heating and cooling from the real experiment presented in Section 3.1.1. Figure 4.1a) and b) present a multi-slice view of the simulated 3D temperatures distribution in two different time instants (900s and 2280s) and Figure 4.1c) and d) present the cooling temperature distributions in instants 600s and 1980s. We can observe temperature gradients originated by changing the temperature of the water inside the cooper pipe. For heating, we imposed in both scenarios (real and simulated), the first 5 min (300 s) to correspond to a baseline temperature of 37°C, and for the remaining time to correspond to a gradual temperature change of the water in the pipe from 37°C to 46°C. In the cooling simulation, it was not considered any baseline time, once, in real experiment it was not applied. In this simulation cooling was implemented by a temperature change from 44°C to 35°C, like in the real scenario.

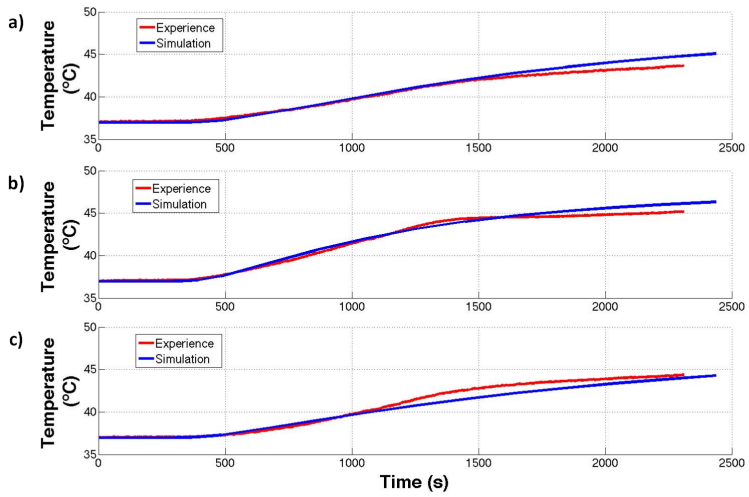

Figure 4.2: Simulated (blue curves) vs measured (red curves) temperatures during heating. a)In a specific position inside the medium and chosen to be approximately the same position as used in the real laboratory experiment. b)Water temperature at the top of the chamber. c) Water temperature at the bottom of the chamber.

In Figure 4.2 the simulated temperatures during heating are compared with the measured ones, when the medium was considered to be a porcine kidney sample. We can observe that the simulated curves closely follow the measured temperature curves, specially during the first 1500 seconds. The measured root mean squared error were 0.46°C, 0.52°C,

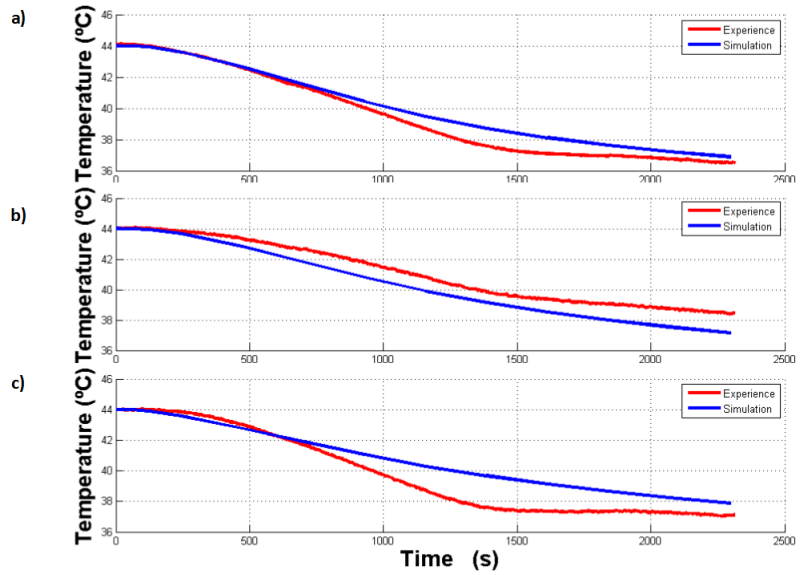

Figure 4.3: Simulated (blue curves) vs measured (red curves) temperatures during cooling. a)In a specific position inside the medium and chosen to be approximately the same position as used in the real laboratory experiment. b)Water temperature at the top of the chamber. c) Water temperature at the bottom of the chamber.

and 0.51°C, for the temperature in the sample, top of the chamber and bottom of the chamber, respectively. In Figure 4.3 the simulated temperatures during cooling are also compared with the real scenario for the same porcine kidney sample. Like in the heating simulation, the first 1000 seconds are very similar between real and simulated scenarios with the root mean squared being 0.56°C, 0.79°C and 1.0°C for temperature in sample, top of the chamber and bottom of the chamber, respectively.

Figure 4.4 shows the temperature collected from the laboratorial experiment (full red curve) in the sample and a set of simulated temperature measurements in the kidney sample tissue at various positions inside the sample. The maximum variation of the temperature simulation measurements given by standard deviation(σ) is 1.28°C. The experimental temperature is within the range $\bar{T}\pm\sigma$ (where T is the simulation mean temperature and σ is the standard deviation), for all range of temperatures. Figure 4.5 shows the experimental temperature (full red curve) in the sample and the simulated temperatures, during cooling, and related to the same sample positions as considered for the heating simulation

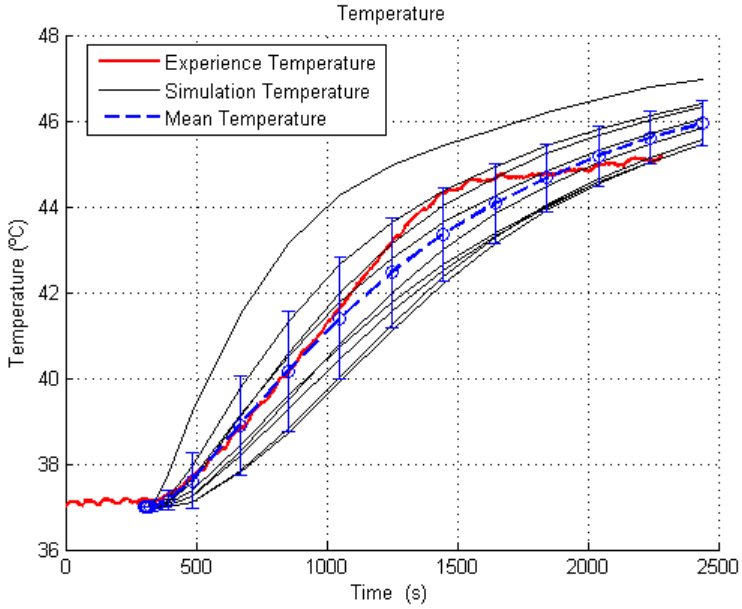

Figure 4.4: Temperature variation during heating, in the copper pipe simulation, in randomly selected positions of the tissue sample.

in Figure 4.4. Again, the experimental temperature is within the range $\bar{T}\pm\sigma$ for all range of temperatures, where the maximum variation σ = 1.15°C.

4.1.2 Simulation of heating by therapeutic ultrasound

In the simulation of heating by therapeutic ultrasound we analyze acoustic pressure and, consequently, the acoustic intensity magnitude (Figure 4.6) through a tissue sample with defined regions formed by different scatterers types with different densities (Visible in Figure 4.20a)), the simulated tissue represent a real human tissue, an average density of $1500kgm^{-3}$ was considered, like in previous simulation. The simulated transducer has a diameter of 1.8 centimeter and a frequency of 1MHz. The attenuation coefficient of the tissue and of the water was considered to be $7.71(Npm^{-1}MHz^{-1})$ and $0.0253(Npm^{-1}MHz^{-1})$ [47], respectively. The ultrasounds velocity in the tissue was considered $1568ms^{-1}$, i.e., the average ultrasounds velocity considered for soft tissues [21].

Temperature gradient representations are presented in Figure 4.7 and Figure 4.8 for two

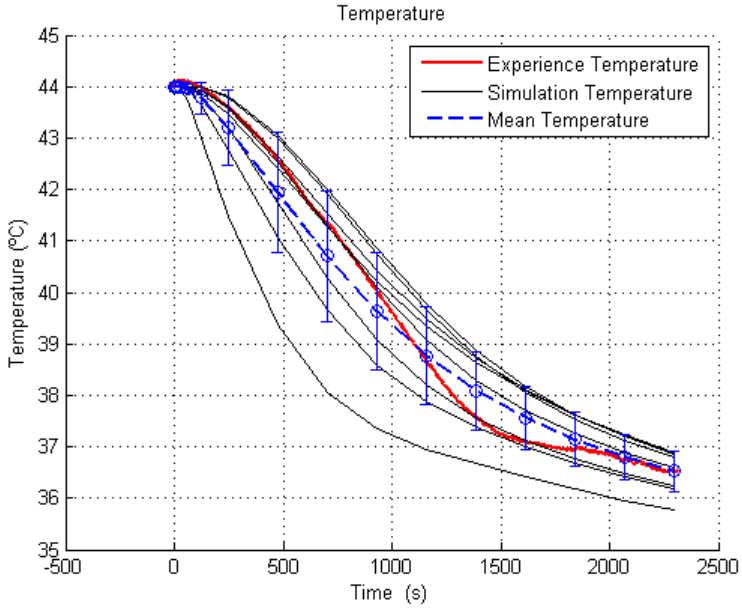

Figure 4.5: Temperature variation during cooling, in the copper pipe simulation, in randomly selected positions of the tissue sample.

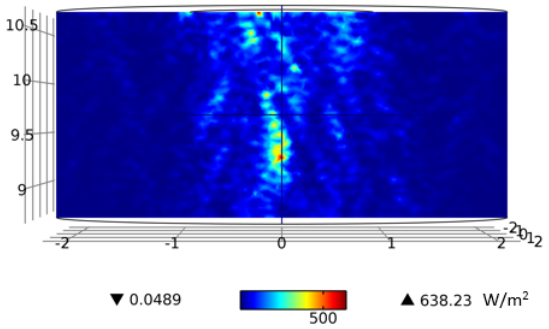

Figure 4.6: A 2D slice of the intensity field applied in the heating by therapeutic ultrasound.

different time instants (60s and 300s), where Figure 4.8 has the blood perfusion influence. The values of blood perfusion were obtained from [53; 54; 55] and were considered to be: blood temperature = 37 °C; blood specific heat = $4000(Jkg^{-1}K^{-1})$; blood perfusion rate = $0.005(ls^{-1})$; blood density = $1000(kgm^{-3})$; and for blood metabolic heat source = $287.7(Wm^{-3})$.

Temperature increases, with a constant acoustic pressure field applied to the sample. Here

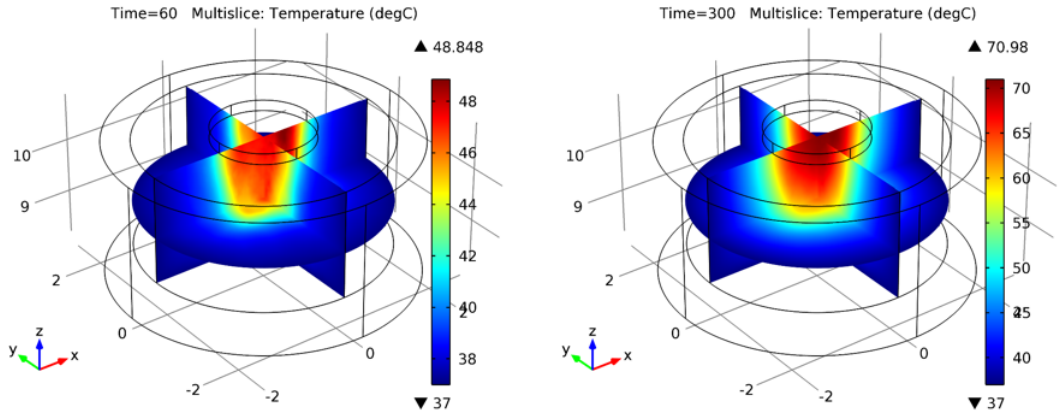

Figure 4.7: Temperature variation obtained with heating by therapeutic ultrasound at two different time instants (left=60s and right=300s).

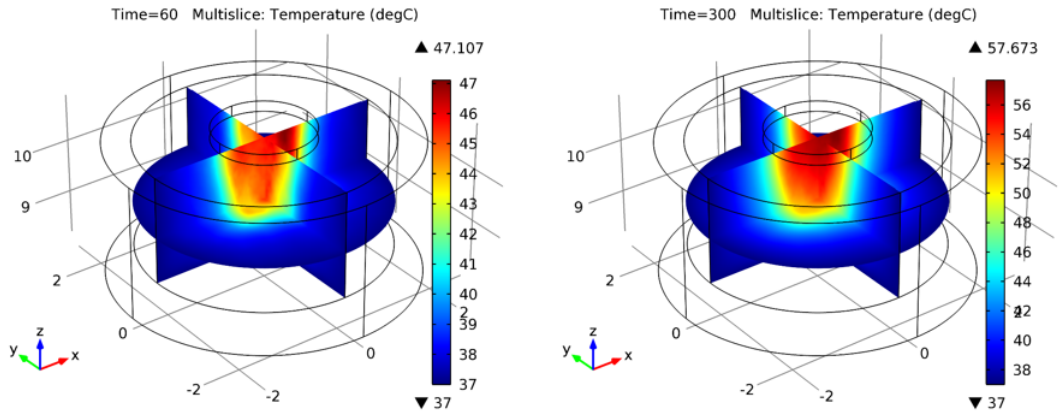

Figure 4.8: Temperature variation obtained with heating by therapeutic ultrasound at two different time instants (left=60s and right=300s) in a sample tissue with the consideration of blood perfusion.

an initial temperature of the tissue of 37°C was also considered. In Figure 4.9 it is represented the variation of temperature with time at a specific location within the sample (Figure4.10). The maximum temperature variation reaches the value of 36.82°C and in the surrounding a value of 13.90°C was observed without blood perfusion. With blood perfusion influence the maximum temperature variation was 19.49°C for the center of the sample and 6.29°C in the surrounding of the center.

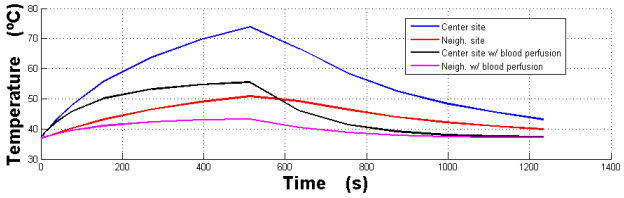

Figure 4.9: The blue and red curves represent the temperature simulated, without the consideration of blood perfusion, at the center of the sample and at a center neighbor position, respectively. The black and magenta curves represent the temperature measured, with the consideration of blood perfusion, at the center of the sample and at a center neighbor position, respectively.

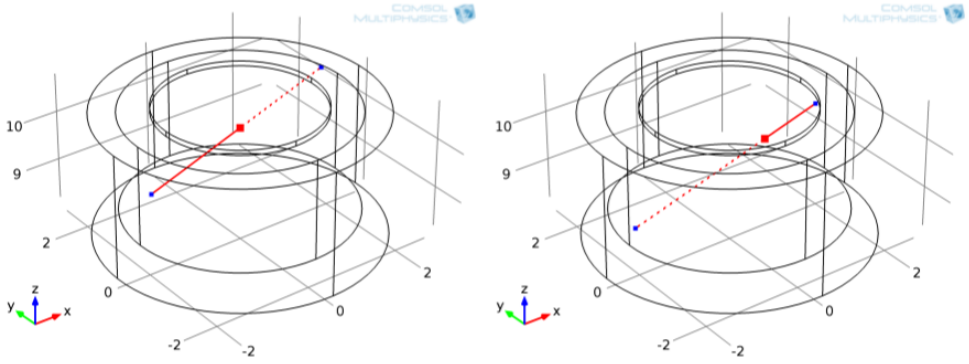

Figure 4.10: Probe sites for temperature acquisition in simulation of heating by therapeutic ultrasound. The red dot in the left figure represent the central measurement point and the red dot in the right figure represent the surrounding measurement point taken in account.

4.1.3 CBE variation with temperature

Simulation of temperature by circulating water in a copper coil

After the simulation of temperature we simulate CBE with the increasing temperature. Using the experimental setup described in Chapter 3, we changed the temperature of *ex-vivo* samples, while acquiring US B-Mode images, and as described in [18] we observed that isolated pixels presented different intensity changes with temperature, and that these changes were coherent with the CBE behavior observed in raw US signals. Aiming to prove that the observed intensity changes are caused by CBE we create a simulation where the regions with different scatterers types were defined based on a thermo-responsive im-

age obtained with the cross-correlation model presented in Section 3.2.2. In the real experiment the *ex-vivo* tissue analyzed was a porcine kidney. The results from the correlation model are presented in Figure 4.11a), where green regions are those for which intensity increases with temperature, red regions those for which intensity decreases with temperature, and blue regions those where it cannot be assigned a clear correlation trend. Regions with positive correlations were considered as regions with lipid scatterers in the simulation, and the regions with negative and unknown correlations were considered in the simulation to belong to an uniform region made by aqueous scatterers. This simplification is valid because we want to observe the effect of different scatterer types and the detail presented in Figure 4.11a) is not important. Figure 4.11b) e c) show the CBE simulations using the pipe-flow heating simulation at different simulation instants. The CBE variation is represented in Figure 4.12 for multiple discrete points inside the simulation. The maximum variation reaches 5dB for a temperature range of 37°C-46°C.

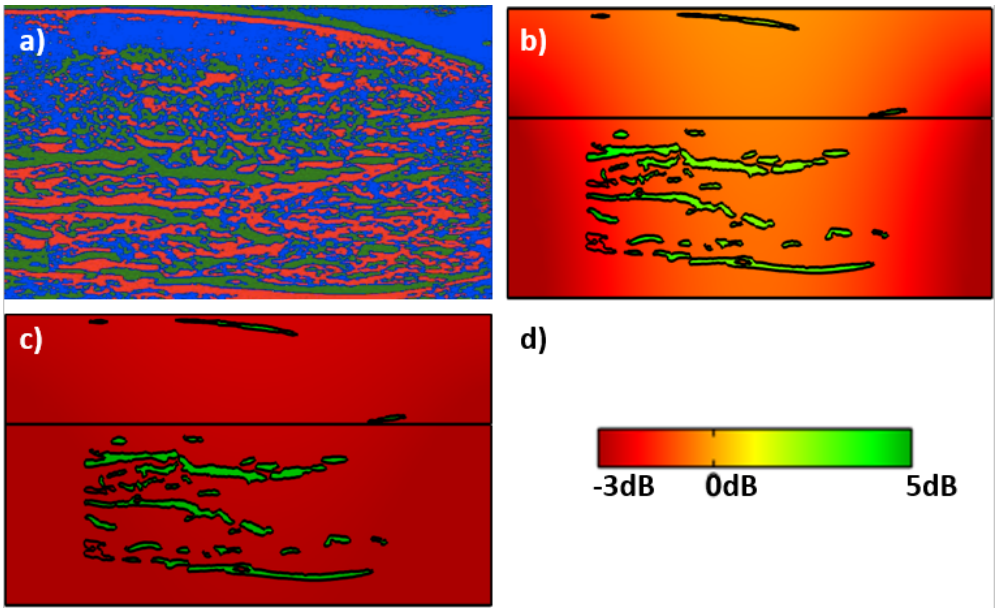

Figure 4.11: Simulated CBE variation with temperature at 900s (b) and 2280s (c). a) Correlation between temperature and pixel intensity change, obtained from conventional B-mode images (More details on 3.2.2). Green pixels indicate regions with positive correlations with temperature, red regions negative correlations, and blue regions undefined correlations (i.e., correlations coefficients less than 0.5). d) Scale related with the CBE simulation.

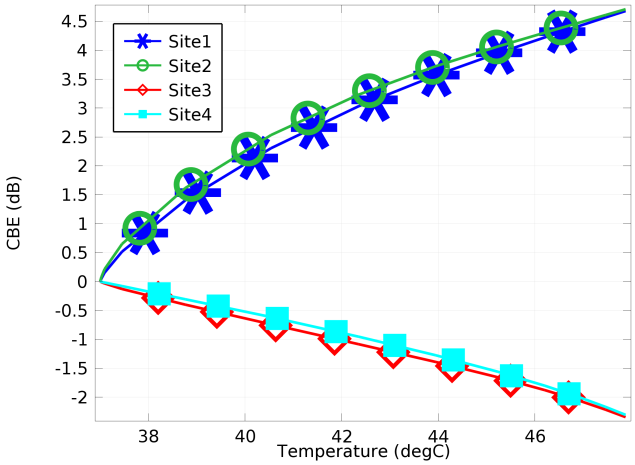

Figure 4.12: CBE curves obtained at different sites in simulation of heating by circulating water by a copper coil.

Simulation of heating by therapeutic ultrasound

For the simulation of CBE in the presence of temperature variations induced by therapeutic ultrasound, we defined the scatterers types in the different regions by using proprietary COMSOL functions, instead of the manual definition as performed in the previous simulation. Manual definition results in non-optimized geometries turning simulations extremely heavies from the computational point of view. In the same way as previously, we considered that the medium has the thermal and acoustic properties of a porcine kidney, but the regions with different scatterers types defined using COMSOL. In this sample we also use the lipid and the aqueous densities defined by $0.92gcm^{-3}$ and $1.05gcm^{-3}$ and the velocities for each type of scatterer (lipid and aqueous) are defined by 2.11 and 2.12, respectively. Figure 4.13 and Figure 4.14 represent the CBE variation, without and with blood perfusion influence, at 390s and 1020s, respectively. As in the simulation of heating by pipe-flow water circulation, CBE evolves in accordance with temperature and as predicted by the CBE theory. Figure 4.15 and Figure 4.16 represent four CBE variations, without and with blood perfusion influence, observed at arbitrary positions inside the simulated sample, respectively. As presented in these figures, CBE vary almost mono-

tonically.

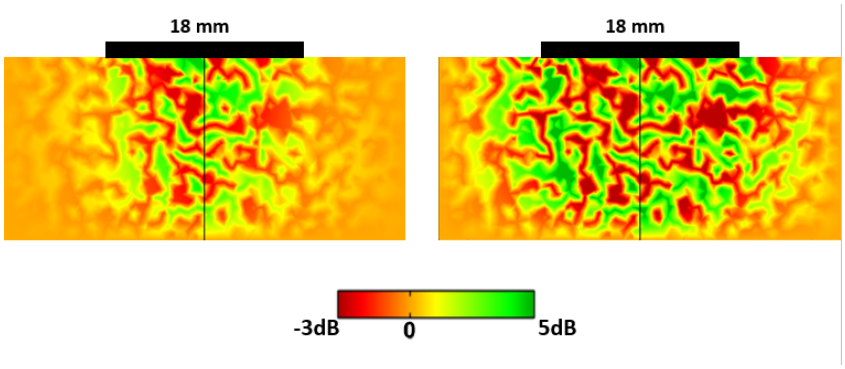

Figure 4.13: Axial CBE variations in simulation of heating by therapeutic ultrasound at: a) 60s and b) 300s

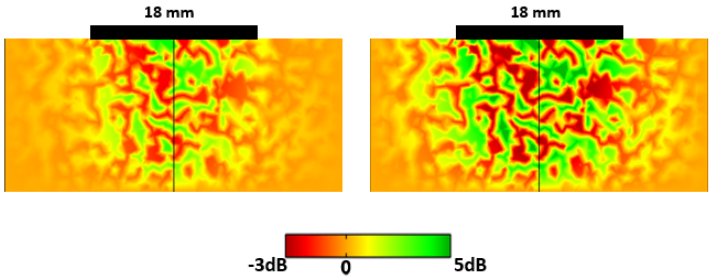

Figure 4.14: Axial CBE variations in simulation of heating by therapeutic ultrasound at: a) 60s and b) 300s; with blood perfusion influence.

4.2 Thermo-responsive image formation

In this Section we consider the development of thermo-responsive using two types of data: from CBE simulations and from real images collected using the experimental setup described previously. Simulation with the data from CBE simulations aim to prove that different medium properties, like scatterers types and densities express different CBE changes that can be modeled by the proposed approaches described in Section 3.2.2, also to infer that the intensity variations observed in real images are due t medium properties differences, justifying the potential of the termo-responsive images developed from real tissues.

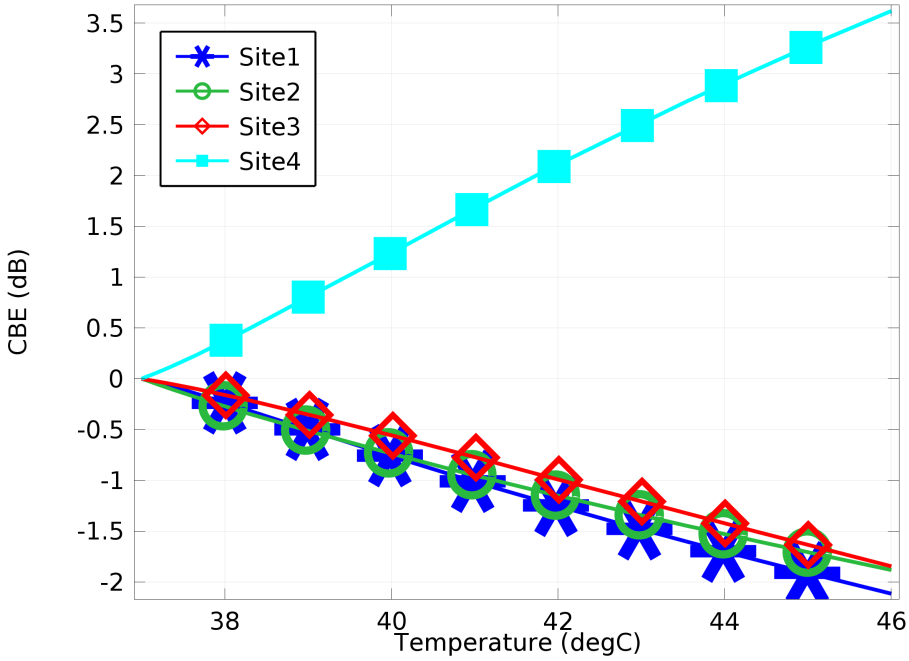

Figure 4.15: CBE curves obtained at different sites in simulation of heating by therapeutic ultrasound.

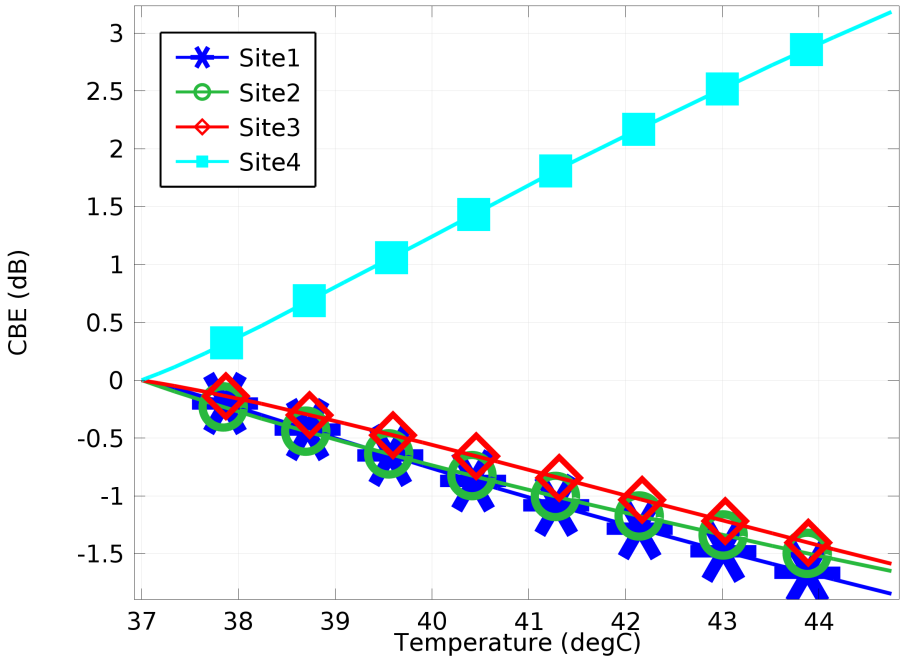

Figure 4.16: CBE curves obtained at different sites in simulation of heating by therapeutic ultrasound with blood perfusion influence.

4.2.1 Polynomial simulation and modeling

To understand the mechanism of this imaging, first we simulate well-defined layered samples represented in Figure 4.17a) and b) represent the two defined media. One rectangular layered domains and other with circle domains. In Figure 4.17a), the bottom rectangle has a lipid density scatterer of $0.92gcm^{-3}$ and consequently a $c(T)_{ls}$ defined by 2.11 the ascending next three rectangles have densities of $1.20gcm^{-3}$, $1.00gcm^{-3}$ and $1.05gcm^{-3}$ and are considered as aqueous scatterer with $c(T)_{as}$ defined by 2.11. In Figure 4.17b), the same properties are attributed to the concentric circles: the exterior of the circles has a lipid scatterer density ($0.92gcm^{-3}$) and velocity ($c(T)_{ls}$). The greatest, medium and inner circles have densities defined as $1.20gcm^{-3}$, $1.00gcm^{-3}$ and $1.05gcm^{-3}$ and are considered as aqueous scatterer with $c(T)_{as}$.

Figure 4.17a1) and a2) represente the simulated thermo-responsive images for the linear and quadratic polynomial fitting, respectively for line layered sample. Figure 4.17b1) and b2) present the images for linear and quadratic polynomial fitting, respectively for the circle layered sample.

To complete the study of the polynomial models in simulated data, we revisited the kidney sample considered previously with regions with different densities and velocities scatterers types. Figure 4.18c) represent the defined scatterers density for the different regions and, consequently, the scatterer velocity defined by 2.11; Figure 4.18d) and e) represent the thermo-responsive images developed using the linear and quadratic polynomials models, respectively. The thermo-responsive images can be compared with one acquired B-mode image (Figure 4.18a)) and with the termo-responsive image obtained with the correlation model in the real B-mode images (Figure 4.18b)). These simulations can also be used for comparison with the termo-responsive images obtained by using the linear and quadratic polynomial fitting in the experimental B-mode images, presented in the

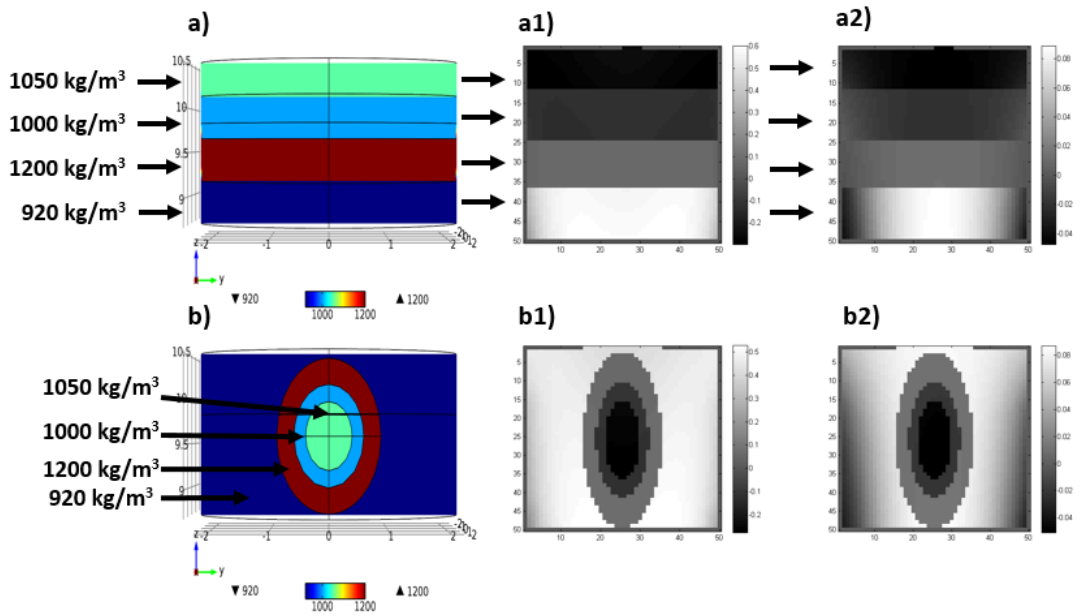

Figure 4.17: Simulation of CBE, obtained by copper pipe heating, in two well-defined layered samples: a) scatterer density in the rectangle layered sample, a1) thermo-responsive image obtained from the application of the linear model, a2) thermo-responsive image obtained from the application of the quadratic polynomial fitting, b) scatterer density in the circle layered sample, b1)thermo-responsive image obtained from the application of the linear polynomial fitting and b2) thermo-responsive image obtained from the application of the quadratic polynomial fitting.

next Section.

The previous density maps are quite simple because, as referred previously, manually-defined regions are heavy to compute by COMSOL, thus in the following we describe a simulation where the density map was defined arbitrary by the native COMSOL functions. Figure 4.19 represent a simulation where heating and cooling was implemented by the copper pipe model, and were the scatterer type and density map was defined by COMSOL. Figure 4.19a) represent the density map, Figure 4.19b) and c) represent the thermo-responsive images obtained with the linear and quadratic polynomial fitting applied to the simulated CBE curves, considering that the temperature is increasing in the medium, respectively. On the other hand, Figure 4.19d) and e) represent the same image type as those in Figures 4.19b) and c) but considering that the temperature is decreasing

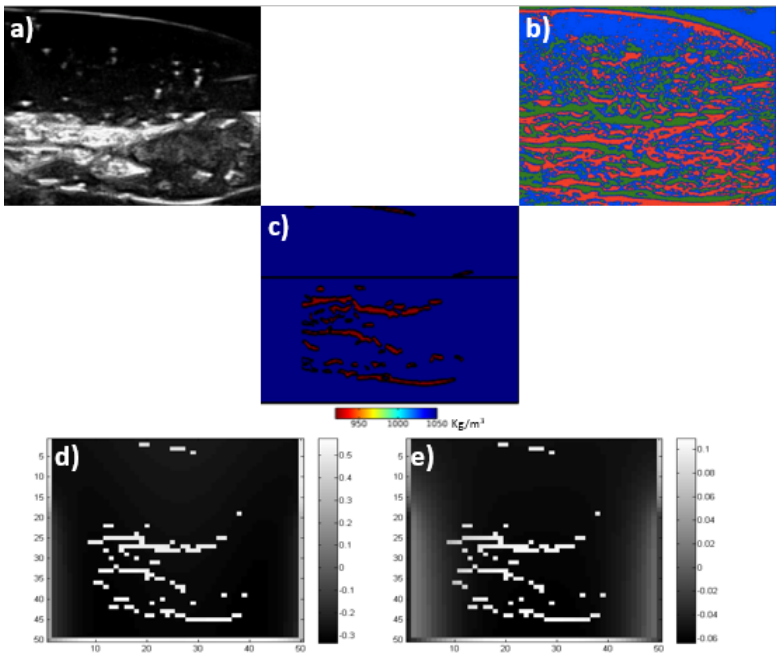

Figure 4.18: Comparison between simulation and real images: a) B-mode image collected from the *ex-vivo* sample, b) thermo-responsive image obtained by applying the cross-correlation modeling to the B-mode images collected from the *ex-vivo* sample, c) scatterer density map, d) thermo-responsive images obtained using the linear polynomial model and e) the quadratic polynomial model in simulated CBE data.

in the medium, respectively. These simulations provide the inspection of CBE curves in more detailed geometries, and are useful to infer if the effect of heating is different from the effect of cooling.

Using the same density map, we simulate the effect of therapeutic heating. It was simulated a US therapeutic heating with and without perfusion. Figure 4.20 represent these simulations. With these simulations, we pretend an approximation to a real scenarios, where exist factors like blood perfusion. Figure 4.20a) represent the medium with different scatterer densities. Figure 4.20b) represent the intensity field of the simulated therapeutic ultrasound transducer (Wm^{-2}). The pressure field was defined to be non-uniform aiming to simulate the effect of intensity gradients. In the same line as from the previous simulations, thermo-responsive images during heating and cooling are presented in Figures 4.20c), d), e) and f), where c) and d) are the simulation of heating with thera-

peutic ultrasound for the polynomial linear and quadratic models, respectively, without the influence of blood perfusion. Figures 4.20e) and f) are the simulation of heating with therapeutic ultrasound for the polynomial linear and quadratic models, respectively, with the influence of blood perfusion.

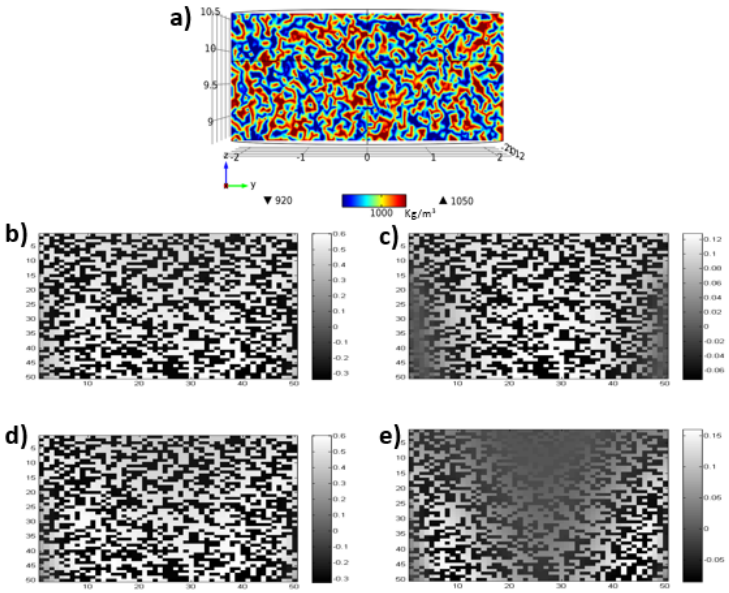

Figure 4.19: Thermo-responsive images from an irregular medium, obtained from simulated CBE data originated by using the PVC Chamber temperature change simulation: a) scatterer density map, b) linear model in heating process, c) quadratic model in heating process, d) linear model for cooling process and e) quadratic model for cooling process.

4.2.2 Thermo-responsive images from intensity variations in B-mode images

Thermo-responsive images from real image data were obtained by tracking the intensity variations at the pixel level by different modeling/fitting approaches. In this thesis we already used one of this image types, more precisely a cross-correlation model, for the definition of different scatterer regions in the previous sub-section, and presented in Figures 4.11a) and 4.18b. Here, in addition we showed the results by applying the linear and quadratic polynomial fitting, and also the modeling by a second-order transfer function

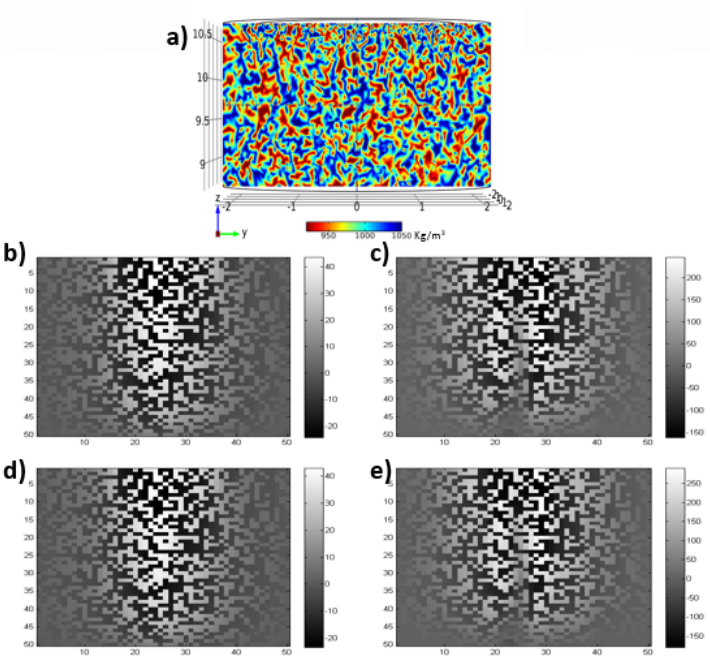

Figure 4.20: Thermo-responsive images from an irregular medium, obtained from simulated CBE data originated by using the heating by therapeutic ultrasound: a) scatterer sample density map, b) linear model without blood perfusion effect, c) quadratic model without blood perfusion effect, d) linear model with blood perfusion effect and e) quadratic model with blood perfusion model.

aiming to capture the oscillations observed in the kidney sample. In addition to the kidney sample already mentioned we also create images from bovine bone, bovine muscle, and porcine muscle.

Analyzing separately the intensity change with temperature for independent pixels we observed relations like those presented in Figure 4.21. On the one hand, as already mentioned, for some pixels it was observed an increasing relation with temperature that can be assumed to be linear (Figure 4.21a)) or to be quadratic (Figure 4.21b)). On the other hand, for other pixels the intensity decreases with the temperature increase, and the relation can be also linear (Figure 4.21c)) or quadratic (Figure 4.21d)). These facts justify the development of thermo-responsive images presented next by the application of the correlation signal modeling, and of the linear and polynomial fitting, as presented in Section 3.2.2.

The thermo-responsive images for the kidney sample are presented in Figure 4.22b,c and

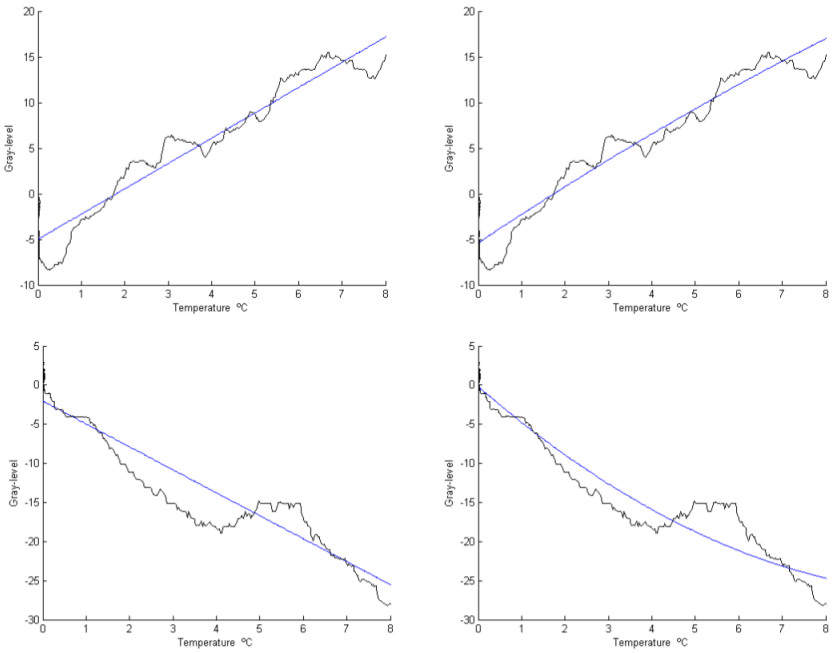

Figure 4.21: Gray-level variation versus temperature (normalized) in four random points of a sample: positive variation with linear model, b) positive variation with quadratic model, c) negative variation with linear model and negative variation with quadratic model.

d. Figure 4.22e is a MRI slice that, corresponds approximately the same slice obtained with conventional B-Mode US (Figure 4.22a)). In Figure 4.23 it is represented the same image types for the same kidney sample, but now during cooling.

In Figure 4.24, it is represented images of a longitudinal cross-section of a bovine bone processing. Here, instead of an MRI image we compare the US and thermo-responsive images with a computed tomography (CT) slice. The bone has the thickness of 1.296 cm, approximately. Just like, in Figure 4.24, Figure 4.26 presents the results for the cooling of the sample. In Figure 4.28 it is represented a bovine muscle processed using the information acquired during heating . Unfortunately, for this tissue it was not possible to acquire images by other imaging modality (like MRI and CT) for comparison. In Figure 4.29 is represented a porcine muscle processed also for the data acquired during heating, and once again, it was not possible to acquire images by other imaging modalities.

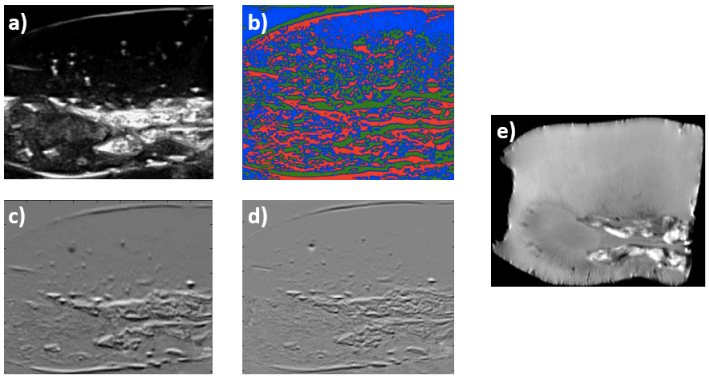

Figure 4.22: Thermo-responsive images from intensity variations computed from B-Mode images colected from a porcine kidney heating experiment: a) B-Mode Ultrasound acquisition, b) thermo-responsive image obtained from the application of the cross-correlation model (colormap: red-negative cross-correlation values, under -0.5; green-positive cross-correlation values, above 0.5; blue-undefined cross-correlation regions values, between -0.5 and 0.5), c) thermo-responsive image obtained from the application of the linear polynomial model, d) thermo-responsive image obtained from the application of the polynomial model and e) MRI Slice.

4.2.3 Thermo-responsive images by second-order transfer function modeling - Preliminary results

In addition, to the observed quadratic and linear relations between the pixel intensity and the temperature, we observed also that in some pixels periodic oscillations are visible, as presented in Figure 4.30. It is possible to observe also that intensity can be oscillatory and increasing or oscillatory and decreasing with the temperature. This observation leads us to implement other type of modeling that could capture these oscillations and also the increasing/decreasing behavior. We considered for this task a modeling by a second-order transfer function as described in Section 3.2.2 Figure 4.31a) and Figure 4.31b) represent a MRI slice and a US image, respectively. Figure 4.31c) is the representation of ω_n(undamped natural frequency coefficient) for each pixel. Figure 4.31d) represent ξ(damping ratio) for each pixel.

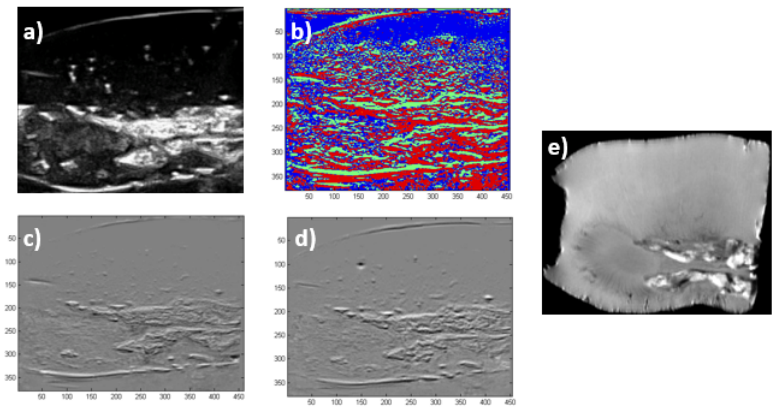

Figure 4.23: Thermo-responsive images from intensity variations computed from B-Mode images colected from a porcine kidney cooling experiment: a) B-Mode Ultrasound acquisition, b) thermo-responsive image obtained from the application of the cross-correlation model (colormap: red-negative cross-correlation values, under -0.5; green-positive cross-correlation values, above 0.5; blue-undefined cross-correlation regions values, between -0.5 and 0.5), c) thermo-responsive image obtained from the application of the linear polynomial model, d) thermo-responsive image obtained from the application of the polynomial model and e) MRI Slice.

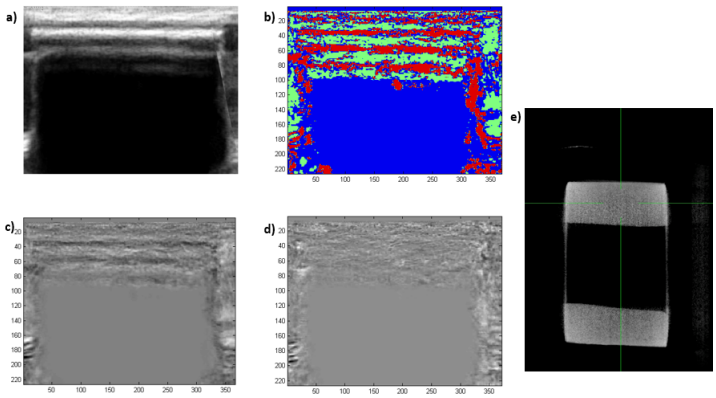

Figure 4.24: Thermo-responsive images from intensity variations computed from B-Mode images colected from a saggital cross-section of a bovine bone heating experiment: a) B-Mode Ultrasound acquisition, b) thermo-responsive image obtained from the application of the cross-correlation model (colormap: red-negative cross-correlation values, under -0.5; green-positive cross-correlation values, above 0.5; blue-undefined cross-correlation regions values, between -0.5 and 0.5), c) thermo-responsive image obtained from the application of the linear polynomial model, d) thermo-responsive image obtained from the application of the polynomial model and e) CT Slice.

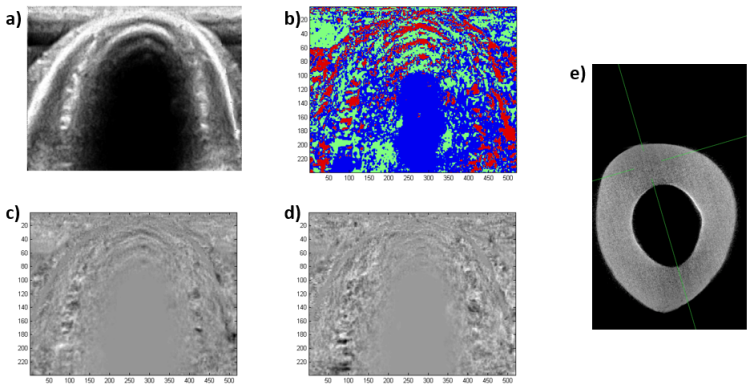

Figure 4.25: Thermo-responsive images from intensity variations computed from B-Mode images colected from a axial cross-section of a bovine bone heating experiment: a) B-Mode Ultrasound acquisition, b) thermo-responsive image obtained from the application of the cross-correlation model (colormap: red-negative cross-correlation values, under -0.5; green-positive cross-correlation values, above 0.5; blue-undefined cross-correlation regions values, between -0.5 and 0.5), c) thermo-responsive image obtained from the application of the linear polynomial model, d) thermo-responsive image obtained from the application of the polynomial model and e) CT Slice.

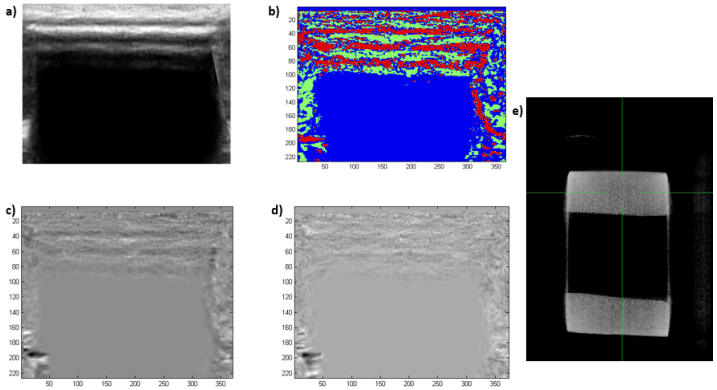

Figure 4.26: Thermo-responsive images from intensity variations computed from B-Mode images colected from a saggital cross-section of a bovine bone cooling experiment: a) B-Mode Ultrasound acquisition, b) thermo-responsive image obtained from the application of the cross-correlation model (colormap: red-negative cross-correlation values, under -0.5; green-positive cross-correlation values, above 0.5; blue-undefined cross-correlation regions values, between -0.5 and 0.5), c) thermo-responsive image obtained from the application of the linear polynomial model, d) thermo-responsive image obtained from the application of the polynomial model and e) CT Slice.

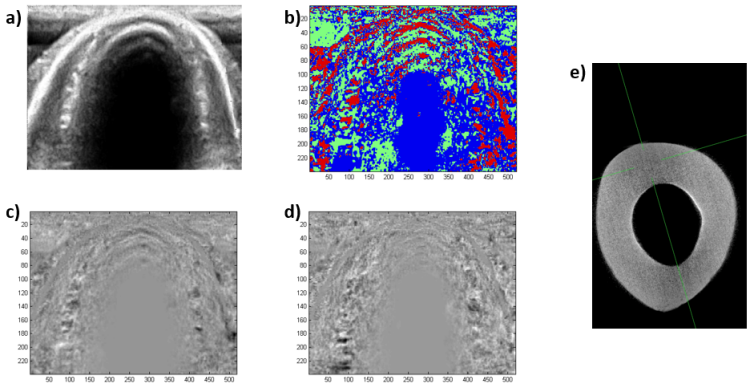

Figure 4.27: Thermo-responsive images from intensity variations computed from B-Mode images colected from a axial cross-section of a bovine bone cooling experiment: a) B-Mode Ultrasound acquisition, b) thermo-responsive image obtained from the application of the cross-correlation model (colormap: red-negative cross-correlation values, under -0.5; green-positive cross-correlation values, above 0.5; blue-undefined cross-correlation regions values, between -0.5 and 0.5), c) thermo-responsive image obtained from the application of the linear polynomial model, d) thermo-responsive image obtained from the application of the polynomial model and e) CT Slice.

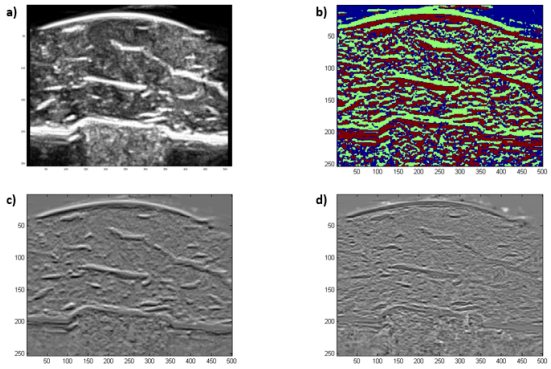

Figure 4.28: Thermo-responsive images from intensity variations computed from B-Mode images colected from a bovine muscle heating experiment: a) B-Mode Ultrasound acquisition, b) thermo-responsive image obtained from the application of the cross-correlation model (colormap: red-negative cross-correlation values, under -0.5; green-positive cross-correlation values, above 0.5; blue-undefined cross-correlation regions values, between -0.5 and 0.5), c) thermo-responsive image obtained from the application of the linear polynomial model and d) thermo-responsive image obtained from the application of the polynomial model.

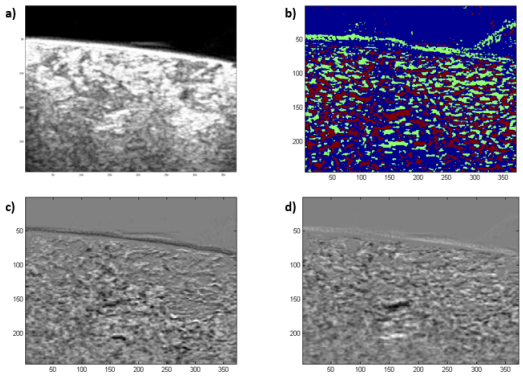

Figure 4.29: Thermo-responsive images from intensity variations computed from B-Mode images colected from a porcine muscle heating experiment: a) B-Mode Ultrasound acquisition, b) thermo-responsive image obtained from the application of the cross-correlation model (colormap: red-negative cross-correlation values, under -0.5; green-positive cross-correlation values, above 0.5; blue-undefined cross-correlation regions values, between -0.5 and 0.5), c) thermo-responsive image obtained from the application of the linear polynomial model and d) thermo-responsive image obtained from the application of the polynomial model.

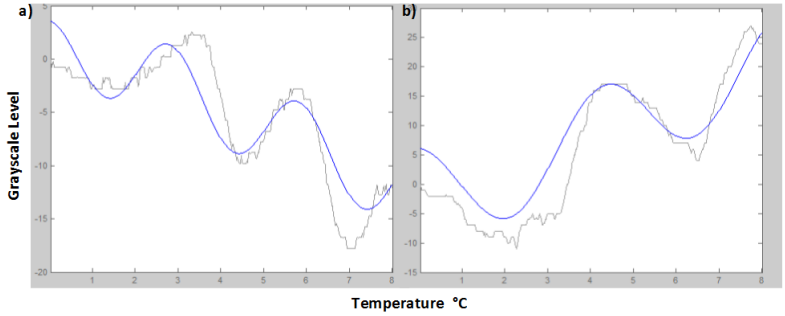

Figure 4.30: Gray-level variation for a) positive and b) negative random pixels, with the respective response system.

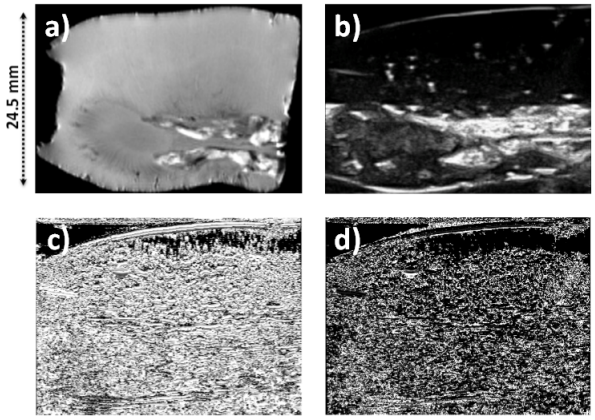

Figure 4.31: Similarities between a) MRI Slice b) B-Node Ultrasound acquisition, c)damping ratio model image and d)Undamped natural frequency model image.

Chapter 5

Discussion

In this Chapter we discuss the simulations from thermo-responsive imaging and the laboratory thermo-responsive images compared with US imaging, MRI and CT.

5.1 Simulations

5.1.1 Simulation of temperature variations by circulating water in a copper coil

The temperature field obtained using the simulation that uses a copper pipe to change temperature presented an expected profile, i.e., at the beginning of the heating phase temperature starts to increase close to the copper pipe and this increase propagate to the center of the PVC chamber as the simulation time increases. At the maximum simulation time (2280s) the temperature is almost homogeneously distributed in the PVC chamber. During cooling a coherent behavior was also observed, i.e. temperature starts to decrease first in the region close to the copper coil and this decrease propagates to the center of the PVC chamber. Simulation temperatures are extremely correlated with experimental temperatures measured. Figure 4.2a),b) and c) represent temperature at system top, medium

under study, and bottom, respectively. The root mean squared error between simulation and experimental temperature for top, medium and bottom are 0.46°C, 0.52°C and 0.51°C, respectively, for a temperature range of 37°C-46°C. The measured error is small and shows the good reproducibility of the simulation.

To verify the variation of the temperature in the simulation we consider ten temperature curves obtained from ten arbitrary positions inside the medium and compare them with the thermocouple measurement obtained from the real experiment and using a kidney sample. We can see that the temperature measured is between the range delimited by the standard deviation of the simulated curves. Figure 4.4 shows the various temperature variations at arbitrary positions inside the simulated sample, but now during cooling. In the same way we compute the mean and the standard deviation for each time instant and extract the standard deviation, plotted as error bars in the figure. The maximum standard deviation observed was of 1.28°C. The experimental temperature is always within the respective standard deviation value. Thus, temperature in the heating simulation is plausible for every point of the simulation sample.

As in heating, in cooling we can assume that the simulated temperatures are close to the experimental ones, and that the root mean squared error for the temperatures at the medium, top, and bottom are in the range [44°C, 35°C]. Compared with heating, in cooling the error are slightly superior.

One of the sources of error may due to the fact that in the simulation we consider a perfect isolation (adiabatic walls) between the PVC chamber and the surrounding environment, which for sure does not occur in the real experimental setup, even with the use of a polystyrene box as an isolation layer. This problem seemed to be amplified during cooling. Future model improvements will consider more realistic boundaries, simulating the polystyrene box and losses with the exterior. Thus in a general way, we conclude that the simulated temperature are validated and that the simulation reproduce closely the

physical phenomena of the laboratory experiment.

5.1.2 Simulation of heating by therapeutic ultrasound

The USs simulation cannot be compared due to lack of experimental data. However, it is extremely useful to understand the real scenario and to prepare future experimental acquisitions.

Accordingly to Figure 4.7, temperature in the sample increases more rapidly than in the simulation where temperature change was implemented by circulating water by a copper pipe. At 390s, the temperature at the center of the sample reaches 44°C, while in the surrounding regions reaches 40°C. The maximum temperatures are reached in half-time of the other simulation. This simulation is divided in two main important parts: first, the heating; second the cooling. Heating is achieved using the USs pressure field that insonifies the sample. Cooling is achieved by natural conduction, when the transducer is turned off at 1020s. With this simulation, we implement two scenarios, one with and other without blood perfusion consideration. Aiming to evaluate the effect of heat transport by blood in *in-vivo* scenarios. Analyzing these two scenarios, we verify that in situations without perfusion the temperature is easily increased than in the case where perfusion was considered. In the central sample area the temperature is increased more rapidly due to the higher intensity of the pressure field. That fact can be visualized in Figure 4.9, where the curves reach higher values in the center areas. It also can be seen that curves without blood influence reach higher values than with the blood influence. For curves with no blood perfusion influence the maximum temperature variation reaches 8.62°C, while with blood perfusion influence this value decrease to 3.10°C, which means a difference of 5.52°C and that is a notorious difference for the center site (see Figure 4.8 and Figure 4.10). These data make perfect sense, once blood has the biological feature of maintain the corporal temperature constant. The importance of this simulation is to understand the blood heat

transfer influence, and is a preliminary step to the *in-vivo* scenario.

5.1.3 CBE variation with temperature

In Figure 4.11a), we observe that isolated pixels present different intensity changes with temperature, and that these changes are coherent with CBE behavior observed in raw US signals. Information from Figure 4.11a) is used to create simulation kidney tissue sample geometry. The geometry of tissue simulation has its main structures defined based on simplified regions observed Figure 4.11a). These regions in the simulations have scatterers properties relative to the information from Figure 4.11a). In accordance with the CBE theory, regions in Figure 4.11a) for which intensity increases with temperature, i.e. the green regions were assumed to be composed by lipid scatterers. On the other hand, red regions were assumed to be composed by aqueous scatterers and are regions were the intensity decreases with temperature increase. Looking at Figure 4.11b) and Figure 4.11c), we observe that, as expected, in the simulation regions defined to represent lipid scatterers presented positive relations with temperature while those with aqueous scatterers have negative relations with temperature. Looking at Figure 4.11 we can also observe a CBE gradient due to the existence of a temperature gradient (more visible at lower temperatures/times, i.e., in Figure 4.11b)). Figures 4.12, 4.15 and 4.16 show the simulated CBE evolution with temperature, where it can be seen positive and negative CBE variations, which is in accordance with the theoretical model. Accordingly, the negative curves are acquired in sites with aqueous scatterers properties, while the positive curves are acquired in sites with lipid scatterers properties.

5.2 Thermo-responsive image formation

5.2.1 Thermo-responsive images from simulated data

We developed well-defined medium geometries with different scatterers densities aiming to understand the effect of density on CBE, and consequently on the thermo-responsive images. One of the medium geometries consisted of concentric regions and the other of layered regions. Each region has a scatterer density that varies between $920(kgm^{-3})$ and $1200(kgm^{-3})$, for an average medium density of $1050(kgm^{-3})$. For the lowest scatterer density, $920(kgm^{-3})$ (corresponding to lipid scatterer) CBE vary positively with temperature, and consequently, a thermo-responsive image in this region will contain pixels with positive values. The other densities correspond to aqueous scattereres and consequently the thermo-responsive images will assume negative or near zero pixel values in these regions. The density of $1200(kgm^{-3})$ results in a CBE relation with temperature that is almost constant, thus the thermo-responsive images will contain pixel values close to zero in the related regions. We can observe also that a density of $1050(kgm^{-3})$ results in CBE relations that decrease faster with temperature and thus the pixel values assume more negative values than for the density of $1000(kgm^{-3})$. In Figure 4.17a2) the effect of the temperature gradient is more visible, because we are assuming a single temperature measurement point in the middle of the sample to develop the entire image. However, the CBE is a local feature that depends on local temperature values, thus some temperature-CBE relations become more quadratic, and the quadratic polynomial fitting is more sensitive to these values.

In order to approximate the simulations to real-world scenarios, we consider more realistic geometries. In one simulation, presented in Figure 4.18, we used regions with different scatterers densities. The used regions are a simplification of domains obtained from a thermo-responsive image obtained from an *ex-vivo* porcine kidney. A second packet of

simulations considers a density map defined by COMSOL. In Figure 4.19 and 4.20 it is presented the results from the application of the linear and quadratic polynomial fitting by considering that the medium temperature is changed by circulating water by a copper pipe, and by therapeutic ultrasound heating, respectively. The result confirms the previous assumptions for the simulations with regular geometries that different densities result in different CBE curves and consequently in thermo-responsive images. To mention again than the quadratic fitting approach is more sensitive to temperature gradients, as explained before for the simulations using regular geometries. The linear fitting has less degrees of freedom and thus is less sensitive to temperature perturbations.

5.2.2 Thermo-responsive images from intensity variations in B-mode images

In all acquisitions, a heating and cooling experiment was made. The acquisition performed in the porcine kidney during heating was the one more explored, since it was used in the simulations to define regions with different scatterers types, and the sample was subjected to MRI imaging. The application of the correlation and of the polynomials models to the B-mode intensity variation acquired from the kidney sample are presented in Figures 4.22b), 4.22c) and 4.22d). Comparing the conventional B-mode image (Figure 4.22a) with the thermo-responsive images it can be seen that they present more details, i.e., an improved sensitivity. The thermo-responsive images contributed with additional information, especially contributing to a better visualization of the continuity and definition of the different structures, improving the quality of US-based images. Comparing the thermo-responsive images one can see that the quadratic polynomial fitting yield even mode detailed images. For the cooling acquisition, similar images, as those obtained during heating were obtained, as previewed by the simulations. In Figure 4.24 a imaging of a sample of an *ex-vivo* bovine bone is developed. It could been seen that the CT image

presents, only the anatomic structure of the bone, like the conventional B-mode image. With the new imaging we had several information compared to the conventional USs. It can been seen how the structures inside mineral structure of a bone sagittal cross-section react to the temperature. This fact, also is verified for the cooling procedure represented in Figure 4.24 and for the bone axial cross-sections represented by Figure 4.25 and 4.27 for heating and cooling procedures, respectively. The images are very similar between the heating and cooling process, too.

Figures 4.28 and 4.29 represented bovine and porcine muscles for a heating procedure, respectively. It can be seen that the texture of these image, in both of developed image models, represent a better definition of tissue continuities and discontinuities than the conventional ultrasound image giving additional information about the tissue structure. Especially, like in the kidney, it is possible to evaluate in more details the different structures and their continuity and interconnection. The studied *ex-vivo* samples aim to give a broader view of the application of the proposed methodology to different types of tissues: soft-tissues represented by the porcine kidney (organ) and muscle samples (muscle tissue), and bone tissue represented by the bovine bones (connective-tissue). In Appendix A, more examples of the processing of other tissues, like fat, are presented.

5.2.3 Thermo-responsive images by second-order transfer function modeling - Preliminary results

We observed oscillations that are not previewed by the present CBE model in the intensity curves extracted from the acquired B-mode images. Given these observations we decided to apply a different modeling approach to capture simultaneously the oscillations and if they are increasing or decreasing in amplitude with temperature. Thus, we applied a modeling based on a second order transfer function and extracted two parameters. One related with the frequency of oscillation, called the undamped natural frequency (ω_n),

and other if the amplitude of the oscillation is increasing or decreasing with temperature, called the damping factor (ξ). By plotting ω_n for each pixel we found that the oscillation occurred at the interfaces between structures, resulting in a kind of segmentation of the tissue structures. The ξ plotting, also, represent a very detailed image, points out that it may exist more information than the one presented by the conventional ultrasound image. So, the oscillations seemed to indicate transition regions with mixed scatterers types, which is also a very interesting finding. However, these assumptions are very preliminary and should be better explored in the future and supported by a modified CBE theory.

Chapter 6

Conclusion

In this thesis we propose a new methodology to improve USs image, turning it more informative. The images computed based in the proposed methodology were called as "thermo-responsive" images because they are dependent on a temperature change and on the response of the media to this change. The response of the media are expressed as intensity changes on the conventional B-mode images. These changes were associated with changes on backscattered energy (CBE), which is a very well known temperature-dependent US feature.

The primary objective of this thesis was to validate the hypothesis that "CBE propagate along the processing pipeline of the ultrasound equipments and have an expression on conventional B-mode images". That is, to validate the assumption that the intensity variations with temperature at the B-mode image level are due to CBE. With the first simulations we concluded that in fact CBE was the main factor affecting intensity variations. Variations of intensity changes were observed during heating and associated with changes in CBE, as proved by the simulation models developed in this thesis. With other simulations we analyzed density variations for different scatterers types, and in accordance with equation 2.7 and 2.8, CBE are sensible to these changes and consequently the thermo-

responsive images highlight these changes. Considering that attenuation is referred to be important for temperatures above 50°C (outside of the temperature range considered) and that for the present CBE theory the speed-of-sound is dependent on temperature (equations 2.10), we can infer that the obtained thermo-responsive images can give information about the combined effect of density and ultrasounds velocities variations with temperature inside the *ex-vivo* tissue samples analyzed. So, we can say that this new imaging modality is the result of the combined effect of density and ultrasounds velocities change with temperature that contribute to an improved visualization of the internal tissue structures, even in those tissues where traditionally conventional USs images are very poor, like in bone.

However, as we show previously, unexpected oscillations by the not previewed by the present CBE theory were visible in the intensity changes with temperature. We identified the regions were they appeared, i.e., at the interfaces, future developments should face the development of a new theoretical basis for this phenomenon. Future developments should also face additional experiments, aiming to find out more about this new imaging modality.

Bibliography

[1] W. R. Hedrick, L. D. Hykes, and L. D. Starchman, *Ultrasound Physics and Instrumentation*. Mosby, 1992, pp. 153–156.

[2] M. Kalra, M. Maher, and T. Toth, "Radiology strategies for ct radiation," *Radiology*, pp. 619–628, 2004.

[3] D. o. N. M. University of Washington. (2013, Oct.) Introduction to physics. [Online]. Available: http//:depts.washington.edu/nucmed/IRL/pet_intro/toc.html

[4] G. Tarantola, H. F. Zito, and P. Gerundini, "Pet instrumentation and reconstruction algorithms in whole body applications," *Journal of Nuclear Medicine*, no. 44, pp. 756–769, 2003.

[5] R. C. Jack, A. M. Bernstein, and P. Thompson, "The alzheimer's disease neuroimaging initiative (adni): Mri methods," *Journal of Magentic Resonance Imaging*, no. 27, p. 695, 2008.

[6] U. of Florida. (2014, May) Magnet lab. [Online]. Available: http://www.magnet.fsu.edu/education/tutorials/magnetacademy/mri/fullarticle.html

[7] M. C. Bhardwaj. (2014, Jun.) Applications of non-contact ultrasound. [Online]. Available: http://www.ndt.net/article/v05n01/bhardwaj/fig17.gif

[8] J. B. Santos, "Licenciatura em engenharia biomedica: Instrumentacao para imagi-

ologia." *Faculdade de Ciencias e Tecnologia da Universidade de Coimbra: IIM*, 2008.

[9] (2014, Jul.) Medical ultrasound parameters ultrasound. [Online]. Available: http://www.imi.ncku.edu.tw/modules/content/talks/971121Image.pdf

[10] N. P. Burns, "Introduction to the physical principles of ultrasound imaging and doppler," *Fundamentals in Medical Biophysics*, no. 19, 2013.

[11] (2014, Jul.) Centro de investigaciones opticas. [Online]. Available: http://www.ciop.unlp.edu.ar/Ingles/Investigacion/LineasDeInvestigacion/ProcImgMetroOpt_eng.html

[12] G. Stetten, A. Cois, W. Chang, D. Shelton, R. Tamburo, J. Castelluci, and O. V. Ramm, "C-mode real-time tomographic reflection for a matrix array ultrasound sonic flashlight," *Lecture Notes in Computer Science*, no. 2879, 2003.

[13] (2014, Jul.) M-mode echocardiography. [Online]. Available: http://askdrwiki.com/mediawiki/index.php?title=M_mode_echocardiography

[14] C. Deane. (2014, Jul.) Doppler ultrasound: principles and practice. [Online]. Available: http://echoincontext.mc.duke.edu/doppler01/doppler01_10.asp

[15] F. J. Carlsen, C. Ewertsen, L. Lonn, and M. B. Nielsen, "An overview with emphasis on breast cancer diagnosis," *Diagnostics*, no. 3, pp. 117–125, 2013.

[16] S. Choudhry, B. Gorman, W. J. Charboneau, D. Tradup, F. Beck, M. Kofler, and S. D. Groth, "Comparasion of tissue harmonic imaging with conventional us in abdominal disease," *Imaging and Therapeutic Technology*, no. 3, pp. 1127–1135, 2000.

[17] O. Weck and Y. I. K. I. Y., "Finite element method," *Engineering Design and Rapid Prototyping*, 2004.

[18] C. A. Teixeira, A. Fontes, M. V. Kruger, A. V. Alvarenga, and W. C. A. Pereira,

"Expressiveness of temperature-induced changes in backscattered energy in conventional b-mode images," *Proceedings of Meetings on Acoustics*, no. 19, 2013.

[19] R. M. Arthur, W. L. Straube, J. W. Trobaugh, and E. G. Moros, "Non-invasive estimation of hyperthermia temperatures with ultrasound," *International journal of hyperthermia*, no. 21, pp. 589–600, 2005.

[20] R. M. Arthur, W. L. Straube, J. D. Starman, and E. G. Moros, "Noninvasive temperature estimation based on the energy of backscattered ultrasound," *Medical Physics*, no. 30, p. 1021, 2003.

[21] R. M. Arthur and W. L. Straube, "Theoretical estimation of the temperature dependence of backscattered ultrasonic power for non-invasive thermometry," *Ultrasound in Medicine and Biology*, no. 20, pp. 915–922, 1994.

[22] G. Haar, "Therapeutic ultrasound," *European Journal of Ultrasound*, no. 1, pp. 3–9, 1999.

[23] C.Simon, P. VanBaren, and E. Ebbini, "Two-dimensional temperature estimation using diagnostic ultrasound," *IEEE Transactions on Ultrasonics, Ferroelectrics and Frequency Control*, no. 45, pp. 1088–1099, 1998.

[24] T. Kim, A. Stoica, and R. S. Chang, *Medical Imaging: a review*. Berlin: Springer-Verlag Berlin Heidelber, 2010, pp. 504–516.

[25] H. Takadama, H. Kim, T. Kokubo, and T. Nakamura, "An x-ray photoelectron spectroscopy study of the process of apatite on bioactive titanum metal," *Journal of biomedical materials research*, no. 55, pp. 185–193, 2001.

[26] T. Florh, S. Schaller, T. Kokubo, and K. Stierstorfer, "Radiology multi-detector row ct systems and image techniques," *Radiology*, no. 235, pp. 756–773, 2005.

[27] A. Kopp, M. Heuschmid, T. Kokubo, and Kuttner, "Multislice computed tomogra-

phy; basic principles and clinical applications," *Electromedica*, no. 68, pp. 94–105, 2000.

[28] J. D. Tward, H. J. Siewerdsen, J. M. Daly, J. D. Moseley, and A. D. Jaffray, "Soft-tissue detectability in cone-beam ct: Evaluation by 2afc tests in relation to physical performance metrics," *Medical Physics*, no. 34, pp. 4459–4471, 2007.

[29] E. M. Phelps and C. J. Mazziotta, "Positron emission tomography: Human brain function and biochemistry," *Science*, no. 4701, 1985.

[30] J. Czernin and H. Schelbert, "Pet/ct imaging: Facts, opinions, hopes and questions," *Journal of Nuclear Medicine*, no. 4, 2004.

[31] I. A. E. Agency, *Cyclotron Produced Radionuclides: Principles and Practice*. Vienna: International Atomic Energy Agency, 2008.

[32] E. M. Haacke, W. R. Brown, R. M. Thompson, and R. Venkatesan, *Magnetic Resonance Imaging: Physical Principles and Sequence Design*. Wiley-Liss, 1999.

[33] W. R. Hedrick, L. D. Hykes, and L. D. Starchman, *Ultrasound Physics and Instrumentation*. Mosby, 1992.

[34] V. Chan and A. Perlas, *Basics of Ultrasound Imaging*. Springer.

[35] (2014, Jul.) Duke university school of medicine. [Online]. Available: http://echoincontext.mc.duke.edu/doppler01/doppler01_10.asp

[36] H. J. Rasmussen, Y. Du, and A. J. Jensen, "Third harmonic imaging using pulse inversion," *IEEE, International Ultrasonics Symposium*, 2011.

[37] D. Rolance, "Finite element analysis," *Department of Materials Science and Engineering, MIT*, 2011.

[38] E. Suli, "Lecture notes on finite element methods for partial differential equations," *Mathematical Institute, University of Oxford*, 2012.

[39] C. Multiphysics. (2014, Jul.) Multiphysics software product suite. [Online]. Available: http://www.itis.ethz.ch/itis-for-health/tissue-properties/database/heat-generation-rate

[40] C. Blog. (2014, Jul.) Solutions for linear systems of equations: Direct and iterative solvers. [Online]. Available: http://www.comsol.com/blogs/solutions-linear-systems-equations-direct-iterative-solvers

[41] (2014, Jul.) Lu decomposition. [Online]. Available: http://en.wikipedia.org/wiki/LU_decomposition

[42] M. Raju, "Parallel computation of finite element navier-stokes codes using mumps solver," *International Journal Of Computer Science Issues*, no. 2, pp. 1694–1784, 2009.

[43] (2014, Jul.) Intel mkl pardiso: Parallel direct sparse solver interface. [Online]. Available: https://software.intel.com/sites/products/documentation/doclib/mkl_sa/11/mklman/GUID-7E829836-0FEF-46B2-8943-86A022193462.htm

[44] (2014, Jul.) Conjugate gradient method. [Online]. Available: http://en.wikipedia.org/wiki/Conjugate_gradient_method

[45] R. Shewchuk, "An introduction to the conjugate gradient method without the agonizing pain," *Natural Sciences and Engineering Research Council of Canada*, 1994.

[46] R. B. Munson, F. D. Young, and H. T. Mokiishi, *Fundamentals of fluid mechanics*. Wiley.

[47] C. Multiphysics. COMSOL Multiphysics, Inc.

[48] ——. COMSOL Multiphysics, Inc.

[49] ——, *Focused Ultrasound Induced Heating in Tissue Phantom: Solved with COMSOL Multiphysics 4.3b - Model Library*. COMSOL Multiphysics, Inc.

[50] M. Richard. (2014, Jul.) Matlab central: mmread.m. [Online]. Available: http://www.mathworks.com/matlabcentral/fileexchange/8028-mmread

[51] M. Documentation. (2014, Jul.) idtf. [Online]. Available: http://www.mathworks.com/help/ident/ref/idtf.html

[52] ——. (2014, Jul.) tfest. [Online]. Available: http://www.mathworks.com/help/ident/ref/tfest.html

[53] I. foundation. (2014, Jul.) Tissue properties. [Online]. Available: http://www.itis.ethz.ch/itis-for-health/tissue-properties/database/heat-generation-rate

[54] J. H. Li, X. X. Zhang, and F. Y. Yi, "Measurement of blood perfusion using the temperature response to constant surface flux heating," *Journal of Thermophysics*, no. 6, pp. 1631–1644, 2002.

[55] M. B. Ducharme and P. Tikuisis, "Role of blood as heat source or sink in human limbs during local cooling and heating," *International Journal Of Computer Science Issues*, no. 5, pp. 2084–2094, 1994.

Real images processed

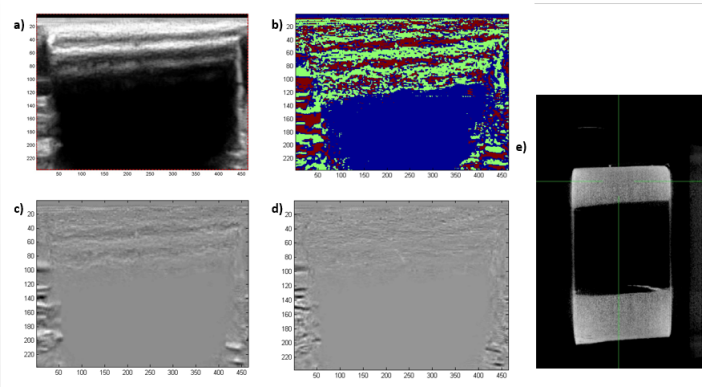

Figure A.1: Thermo-responsive images from intensity variations computed from B-Mode images collected from a saggital cross-section of a bovine bone heating experiment: a) B-Mode Ultrasound acquisition, b) thermo-responsive image obtained from the application of the cross-correlation model (colormap: red-negative cross-correlation values, under -0.5; green-positive cross-correlation values, above 0.5; blue-undefined cross-correlation regions values, between -0.5 and 0.5), c) thermo-responsive image obtained from the application of the linear polynomial model, d) thermo-responsive image obtained from the application of the polynomial model and e) CT Slice.

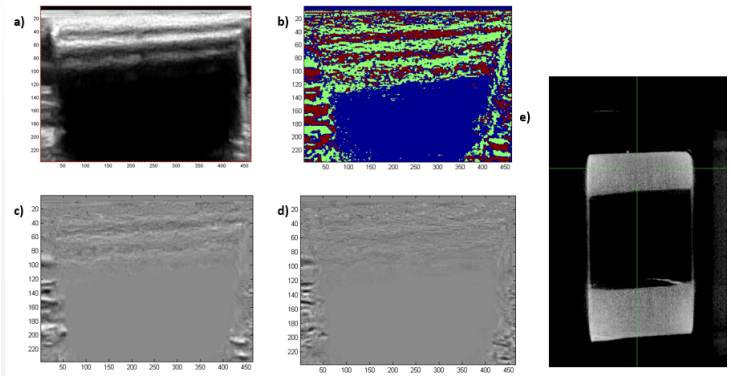

Figure A.2: Thermo-responsive images from intensity variations computed from B-Mode images collected from a saggital cross-section of a bovine bone cooling experiment: a) B-Mode Ultrasound acquisition, b) thermo-responsive image obtained from the application of the cross-correlation model (colormap: red-negative cross-correlation values, under -0.5; green-positive cross-correlation values, above 0.5; blue-undefined cross-correlation regions values, between -0.5 and 0.5), c) thermo-responsive image obtained from the application of the linear polynomial model, d) thermo-responsive image obtained from the application of the polynomial model and e) CT Slice.

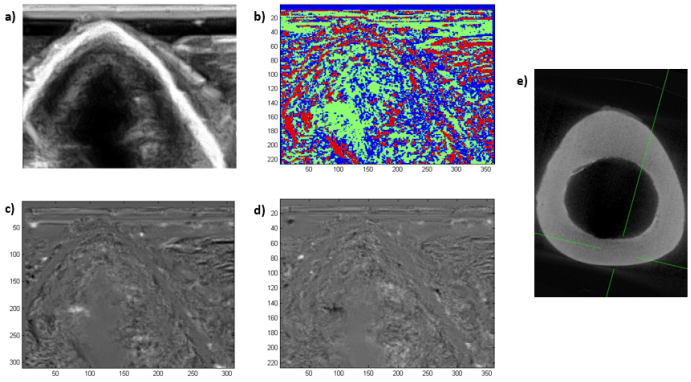

Figure A.3: Thermo-responsive images from intensity variations computed from B-Mode images collected from a axial cross-section of a bovine bone heating experiment: a) B-Mode Ultrasound acquisition, b) thermo-responsive image obtained from the application of the cross-correlation model (colormap: red-negative cross-correlation values, under -0.5; green-positive cross-correlation values, above 0.5; blue-undefined cross-correlation regions values, between -0.5 and 0.5), c) thermo-responsive image obtained from the application of the linear polynomial model, d) thermo-responsive image obtained from the application of the polynomial model and e) CT Slice.

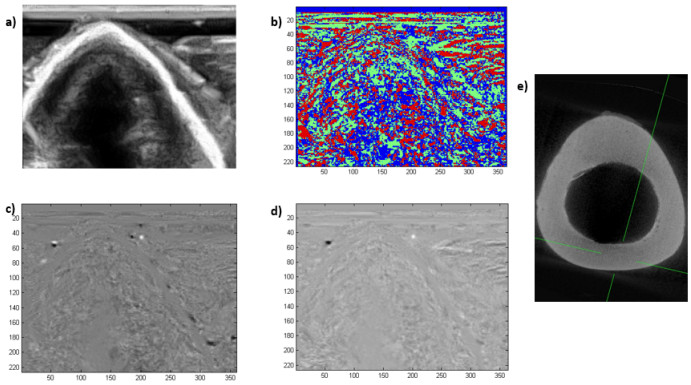

Figure A.4: Thermo-responsive images from intensity variations computed from B-Mode images collected from a axial cross-section of a bovine bone cooling experiment: a) B-Mode Ultrasound acquisition, b) thermo-responsive image obtained from the application of the cross-correlation model (colormap: red-negative cross-correlation values, under -0.5; green-positive cross-correlation values, above 0.5; blue-undefined cross-correlation regions values, between -0.5 and 0.5), c) thermo-responsive image obtained from the application of the linear polynomial model, d) thermo-responsive image obtained from the application of the polynomial model and e) CT Slice.

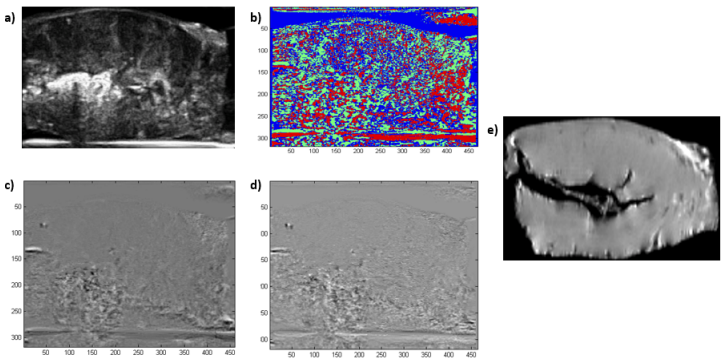

Figure A.5: Thermo-responsive images from intensity variations computed from B-Mode images collected from a porcine heart heating experiment: a) B-Mode Ultrasound acquisition, b) thermo-responsive image obtained from the application of the cross-correlation model (colormap: red-negative cross-correlation values, under -0.5; green-positive cross-correlation values, above 0.5; blue-undefined cross-correlation regions values, between -0.5 and 0.5), c) thermo-responsive image obtained from the application of the linear polynomial model, d) thermo-responsive image obtained from the application of the polynomial model and e) MRI Slice.

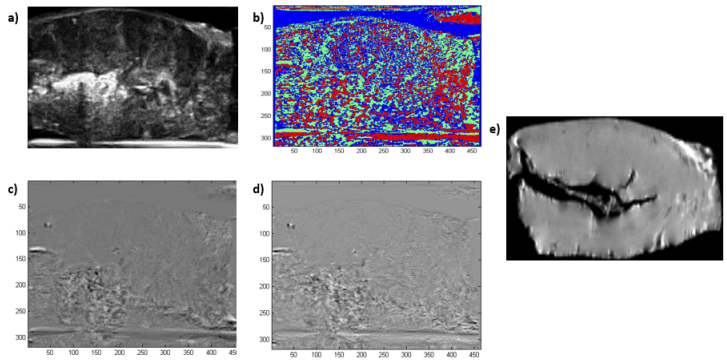

Figure A.6: Thermo-responsive images from intensity variations computed from B-Mode images collected from a porcine heart cooling experiment: a) B-Mode Ultrasound acquisition, b) thermo-responsive image obtained from the application of the cross-correlation model (colormap: red-negative cross-correlation values, under -0.5; green-positive cross-correlation values, above 0.5; blue-undefined cross-correlation regions values, between -0.5 and 0.5), c) thermo-responsive image obtained from the application of the linear polynomial model, d) thermo-responsive image obtained from the application of the polynomial model and e) MRI Slice.

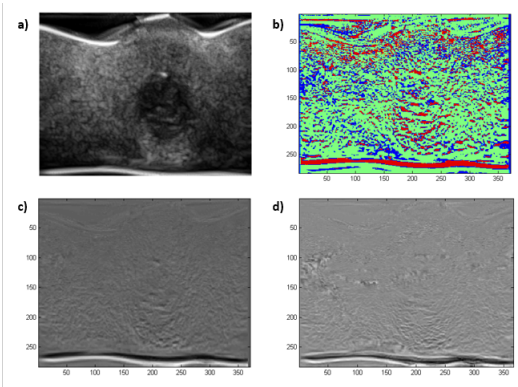

Figure A.7: Thermo-responsive images from intensity variations computed from B-Mode images collected from a silicon phantom heating experiment: a) B-Mode Ultrasound acquisition, b) thermo-responsive image obtained from the application of the cross-correlation model (colormap: red-negative cross-correlation values, under -0.5; green-positive cross-correlation values, above 0.5; blue-undefined cross-correlation regions values, between -0.5 and 0.5), c) thermo-responsive image obtained from the application of the linear polynomial model and d) thermo-responsive image obtained from the application of the polynomial model.

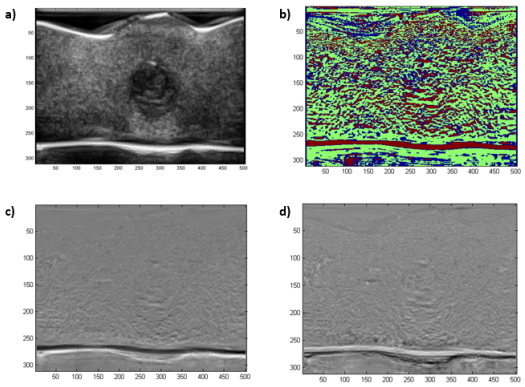

Figure A.8: Thermo-responsive images from intensity variations computed from B-Mode images collected from a silicon phantom cooling experiment: a) B-Mode Ultrasound acquisition, b) thermo-responsive image obtained from the application of the cross-correlation model (colormap: red-negative cross-correlation values, under -0.5; green-positive cross-correlation values, above 0.5; blue-undefined cross-correlation regions values, between -0.5 and 0.5), c) thermo-responsive image obtained from the application of the linear polynomial model and d) thermo-responsive image obtained from the application of the polynomial model.

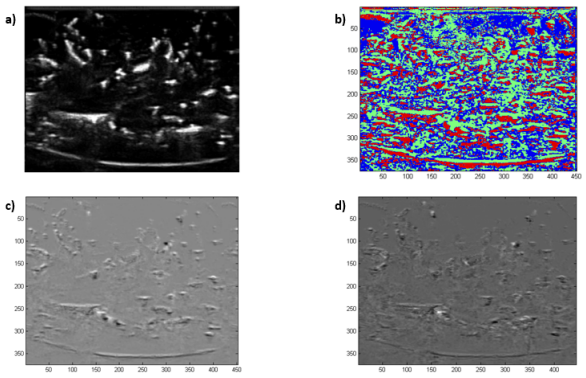

Figure A.9: Thermo-responsive images from intensity variations computed from B-Mode images collected from a porcine liver heating experiment: a) B-Mode Ultrasound acquisition, b) thermo-responsive image obtained from the application of the cross-correlation model (colormap: red-negative cross-correlation values, under -0.5; green-positive cross-correlation values, above 0.5; blue-undefined cross-correlation regions values, between -0.5 and 0.5), c) thermo-responsive image obtained from the application of the linear polynomial model and d) thermo-responsive image obtained from the application of the polynomial model.

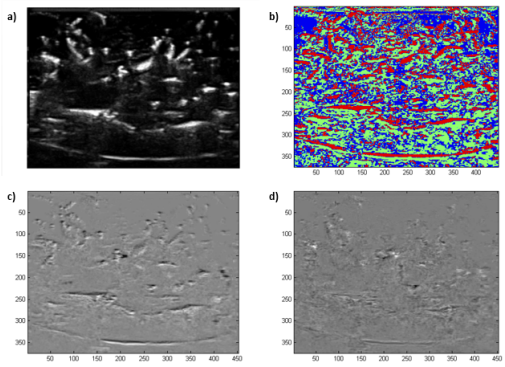

Figure A.10: Thermo-responsive images from intensity variations computed from B-Mode images collected from a porcine liver cooling experiment: a) B-Mode Ultrasound acquisition, b) thermo-responsive image obtained from the application of the cross-correlation model (colormap: red-negative cross-correlation values, under -0.5; green-positive cross-correlation values, above 0.5; blue-undefined cross-correlation regions values, between -0.5 and 0.5), c) thermo-responsive image obtained from the application of the linear polynomial model and d) thermo-responsive image obtained from the application of the polynomial model.

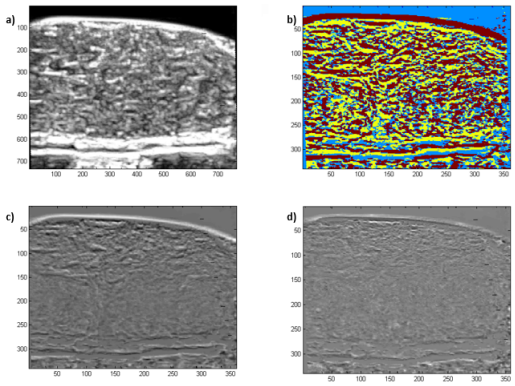

Figure A.11: Thermo-responsive images from intensity variations computed from B-Mode images colected from a porcine fat heating experiment: a) B-Mode Ultrasound acquisition, b) thermo-responsive image obtained from the application of the cross-correlation model (colormap: red-negative cross-correlation values, under -0.5; green-positive cross-correlation values, above 0.5; blue-undefined cross-correlation regions values, between -0.5 and 0.5), c) thermo-responsive image obtained from the application of the linear polynomial model and d) thermo-responsive image obtained from the application of the polynomial model.

Proceeding Papers published

A Coupled 4-Dimensional Temperature-Changes in Backscattered Energy simulation model based in Ultrasound

R. J. Simões[1], M. A. Von Kruger[2], W. C. A. Pereira[2] and C. A. Teixeira[1]

[1] Centre for Informatics and Systems (CISUC), University of Coimbra, Portugal
[2] Programa em Engenharia Biomédica, COPPE, Universidade Federal do Rio de Janeiro, Brazil

Abstract— **Ultrasound (US) has been pointed as an appropriate technology for non-invasive temperature estimation by acquisition of both raw backscattered signals and images. Among the temperature-dependent features, changes in backscattered energy (CBE) have been pointed as an appropriate measure. CBE are extracted from raw backsacttered signals, but can be estimated form B-Mode ultrasound images as recently observed by the authors.**

We developed a coupled Temperature-CBE model in COMSOL based on a previous experiment with temperature variation in a sample of biological tissue. This model enables 4D (3D plus time) simulations.We intend to clarify the influence of CBE variations on the intensity of conventional US images observed by the authors in past experiments.

The simulated temperature differ from real temperatures of about a root mean square error of 0.5°C, in a temperature changes from 37°C to 46°C. CBE simulations are in accordance with the theory that it presents a monotonic relation with temperature, and that: for aqueous and lipid scatterers CBE decrease and increase with temperature, respectively. Finally, the developed model enabled us to confirm the hypothesis that CBE propagate along the processing pipeline of the US scanners and can be observed in B-mode images.

Keywords— **Changes on backscattered energy, Temperature, COMSOL, Non-invasive temperature estimation.**

I. Introduction

The idea of estimating temperature by non-invasive methods is very attractive, since it would enable the tracking of thermal dose, while minimizing secondary effects of invasive temperature measurements. In addition, this idea would become more interesting if one could estimate temperature in real-time, with minimal errors, on a broad number of patients, and with low-cost and portable instrumentation. Magnetic resonance imaging (MRI) solved partially the problem, i.e., it achieved acceptable errors and real-time processing [1]. However, it requires expensive instrumentation, broad application, and portability. In this sense, ultrasound (US) could contribute to solve the MRI problems, and a considerable research effort in the past 20 years has been dedicated to it. Among the US features, temporal echo-shifts [2] originated from stationary targets, and changes on backscattered energy (CBE) from sub-wavelength medium inhomogeneities [3] were the more studied ones. Both measures detected temperature changes because they are sensitive to changes on speed-of-sound (SOS) and medium expansion/compression. However, temporal echo-shifts are highly sensitive to medium movements. In this sense CBE are more robust and vary monotonically with temperature. It was reported that lipid scatterers contribute with monotonically increasing CBE curves with temperature, while aqueous scatterers have monotonically decreasing trends[1, 3, 4]. In this paper we developed a coupled Temperature-CBE model in COMSOL Multiphysics® (COMSOL,Inc) that enables 4D (3D plus time) simulations of CBE in user defined geometries. Simulations are developed in a finite element analysis software, suitable for the simulation of coupled physical phenomena. The simulation model reproduces a real experiment apparatus used by the authors to studying the effects of temperature on US B-mode images, and aims to validate the hypothesis that "CBE propagate along the processing pipeline of the ultrasound equipments and have an expression on conventional B-mode images".

II. Materials and Methods

A. Laboratory experiment

A experiment was set up in our laboratory as presented in Fig. 1. The experiment was developed to change temperature of a given medium and acquire conventional images and temperature information, aiming to study the effects of temperature in ultrasound images. The six main parts of the apparatus are: 1) A polyvinyl chloride (PVC) chamber that contains: water, an aluminum support, and a spiral-shaped cooper pipe. The cooper pipe enables changing the water temperature, and consequently the aluminum and medium temperature. 2) A water-bath temperature control system that injects water through the cooper pipe and enables to change the temperature inside the chamber. The system accepts a setpoint and automatically controls water temperature. Here we con-

sidered temperature changes between 37°C and 46 °C. 3) An ultrasound scanner with a linear transducer and that produces B-Mode images. 4) A temperature measurement system that enables the acquisition of temperature inside the chamber in three different places: at the bottom; inside the medium, and at the top of the chamber. 5) A computer that receives both US (B-Mode) images, via a video acquisition board, and the temperature values, supplied by the temperature measurement system. 6) A polystyrene isolation box that minimizes the influence of room temperature fluctuations.

To mention that, in this paper we report the development of the COMSOL model for the PVC chamber, which is the main part of the system.

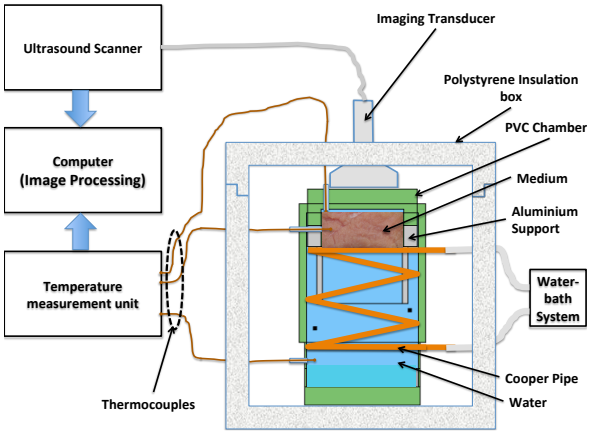

Fig. 1: Experiment for image acquisition and temperature change. The experiment is composed by six main parts: a polyvinyl chloride (PVC) chamber (green) that contains water (blue), a cooper pipe (reddish brown) and an aluminum support (gray); a water temperature control system; an ultrasound scanner; a temperature measurement system; a computer; and a polystyrene isolation box.

B. COMSOL model

For the simulations developed we assumed that: the chamber does not exchange heat with the outside environment; the other parts of the experiment were assumed to be ideal, and that they supplied the required inputs to the chamber system, and had no influence on it; temperature change is the main system input and was simulated by assuming a constant flow of water that enters in a spiral-shaped cooper pipe at a know temperature. The different parts of the model, and their coupling are presented in Fig. 2, and are described in the next sub-sections.

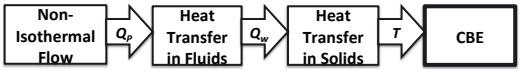

Fig. 2: Coupling between the different models. Where Q_P is the heat source from the cooper pipe, Q_W, is the transferred heat from the water in the PVC chamber to the aluminum and the medium, and T is the temperature.

B1 Non-Isothermal flow

The first step of the COMSOL model development was the definition of the model geometry, and material properties in accordance with the real chamber presented in Fig. 1. Afterwards the physical laws that dictate the influence of circulating water inside a cooper pipe were introduced in the model. COMSOL provides all the necessary tools to simulate fluid fluxes in pipes [5], and all the necessary fluid properties. Fluid flow is modeled by considering the basic laws of conservation of mass, momentum and energy [5].

B2 Heat transfer in fluids

In the real experiment the water temperature inside the cooper pipe is externally regulated by a water-bath system. With COMSOL we simulate this behavior by defining the temperature at which the water enters in the pipe. The heating simulation model is achieved by another physics module from COMSOL named *Heat transfer in fluids*. This module coupled with *Non-Isothermal Pipe Flow module*, enables the simulation of temperature change inside the PVC chamber.

The heat transfer to the water happens due to convection and it is defined by [6]:

$$\rho C_p \frac{\partial T}{\partial t} + \rho C_p u \cdot \nabla_t T = \nabla_t k \nabla_t T + Q_P \qquad (1)$$

where T(K) is the water temperature in the chamber,

C_p(J/kg/K) and k(W/m/K) are the water heat capacity at constant pressure, and the thermal conductivity respectively. The term Q_P from equation 1, is the heat source from the pipe and is defined by: $Q_P = hz(T - T_P)$, where z(m) is the pipe perimeter, h(W/m^2/K), is the heat transfer coefficient, T, is the water temperature in the chamber and T_P(K), is the water temperature in the pipe. The heat transfer coefficient (h) depends on the water properties and on the pipe flux properties [5].

B3 Heat transfer in solids

We simulated changes in temperature in the aluminum and in the medium, imposed by changes in the water in the chamber. In solids heat transfer is done by conduction, as expressed by [6]:

$$\rho C_p \frac{\partial T}{\partial t} = \nabla_t k \nabla_t T + Q_W, \qquad (2)$$

where Q_W(W/m), is the transferred heat from the water in the chamber to the solid structure. The heat transfer is mediated again by coupling two modules from COMSOL: *Heat transfer in Fluids* and *Heat Transfer in Solids*.

B4 CBE simulation

The backscattered energy signal received from a medium/tissue depends on tissue properties, like attenuation and the backscattered coefficient. The backscattered coefficient depends on medium speed-of-sound (SOS) and density. R.M.Arthur and J. W. Trabough [1] modeled CBE originated by sub-wavelength scatterers as a function, SOS, attenuation, and density:

$$CBE(T) = \frac{\alpha(T_R)}{\alpha(T)} \cdot \frac{\eta(T)}{\eta(T_R)} \cdot \frac{1 - e^{-2\alpha(T)z}}{1 - e^{-2\alpha(T_R)z}} \tag{3}$$

where T is the temperature in °C, T_R is a reference (basal) temperature,α(T) is the temperature-dependent attenuation, η(T) is the backscattered coefficient, and z is the path traveled by a given ultrasound wave within the medium volume. The backscatter coefficient is defined by:

$$\frac{\eta(T)}{\eta(T_R)} = \frac{\left(\frac{\rho_m c(T)_m^2 - \rho_s c(T)_s^2}{\rho_s c(T)_m^2}\right)^2 + \frac{1}{3}\left(\frac{3\rho_s - 3\rho_m}{2\rho_s - \rho_m}\right)^2}{\left(\frac{\rho_m c(T_R)_m^2 - \rho_s c(T_R)_s^2}{\rho_s c(T_R)_m^2}\right)^2 + \frac{1}{3}\left(\frac{3\rho_s - 3\rho_m}{2\rho_s - \rho_m}\right)^2}. \tag{4}$$

Where ρ_m is the medium density, $c(T)_s$ is the temperature-dependent SOS of the scatterer s and $c(T)_m$, the SOS of the medium.

In the literature [4] two types of scatterers are commonly assumed: a lipid-based scatterers and a water-based (aqueous) scatterers, both being part of a water-based medium. The density for lipid and aqueous scatterers are referred to be as 0.92 g/cm^3 and [1.05-1.2] g/cm^3, respectively. The variation of velocity (c) and attenuation (α) with temperature was assumed to be described by the following polynomials[4]:

$$\alpha(T) \approx 0.98 - 0.03T + 0.80e^{-3}T^2 - 0.68e^{-5}T^3 \tag{5}$$
$$c(T)_m \approx 1533.1 + 3.06T - 0.03T^2 \tag{6}$$
$$c(T)_{ls} \approx 1810.7 - 13.89T + 0.10T^2 \tag{7}$$
$$c(T)_{as} \approx 1471.4 + 4.00T - 0.04T^2. \tag{8}$$

Where α(T), $c(T)_m$, $c(T)_{ls}$, and $c(T)_{as}$ are the temperature dependent attenuation coefficient, SOS in soft-tissue, SOS in lipid scatterers, and SOS in aqueous scatterers, respectively.

We implemented CBE equations 3 and 4 from literature in COMSOL, and generate solutions with CBE over time, space and temperature. The temperature variations obtained from the *Heat Transfer* modules (in fluids and solids) and the information referred above concerning densities, velocities and attenuation provide all the necessary information to compute CBE. To simulate heterogeneous media, we defined specific medium geometries with specific characteristics, i.e., with different types of scatterers.

III. Results & Discussion

Fig. 3 presents an axial cross-section of the simulated 3D temperatures distribution in two different time instants (900s and 2280s). We can observe temperature gradients originated by temperature changes. As expected, temperature is higher close to the pipe and tends to decrease as distance from the pipe increases. Temperature solutions are generated for all the elements in the 3D geometry, discrete point locations can be inspected, turning possible the comparison between temperatures originated by the simulation and real temperatures observed in the laboratory. For the results presented in this paper, we imposed in both scenarios (real and simulated), the first 5 min (300 s) to correspond to a baseline temperature of 37°C, and for the remaining time to correspond to a gradual temperature change of the the water temperature in the pipe from 37°C to 46°C. In Fig. 4 the simulated temperatures are compared with the measured ones, when the medium was considered to be a porcine kidney sample. We can observe that the simulated curves closely follow the measured temperature curves, specially during the first 1500 seconds. The measured root mean squared error were 0.46°C, 0.52°C, and 0.51°C, for the temperature in the sample, top of the chamber and bottom of the chamber, respectively.

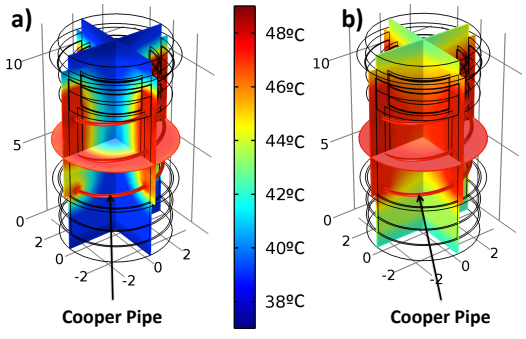

Fig. 3: Spatial temperature simulation at (a) 900s and (b) 2280s after the simulation starting.

In a previous work [7], and using the experimental setup described in Sub-Section A we changed the temperature of ex-vivo samples, while acquiring US B-Mode images. We observed that isolated pixels presented different intensity changes with temperature, and that these changes were co-

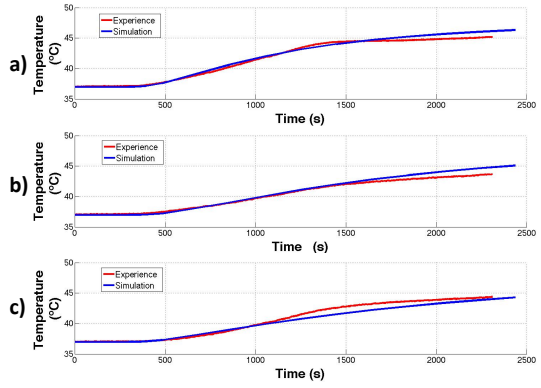

Fig. 4: Simulated (blue curves) vs measured (red curves) temperatures. a)In a specific position inside the medium and chosen to be approximately the same position as used in the real laboratory experiment. b)Water temperature at the top of the chamber. c) Water temperature at the bottom of the chamber.

herent with the CBE behavior observed in raw US signals. The main conclusion was that CBE observed in raw US signals propagated along the processing pipeline of the ultrasound scanner and has an expression on the final image. We replicate the same experiment but now using a porcine kidney sample. We again observed that for some pixels a positive correlation between intensity and temperature was observed, while for others a negative correlation exists, as presented in Fig. 5a. In this paper we used this correlation information to define CBE simulations in COMSOL as follow. First of all we create a binary image, based on Fig. 5a, describing positive correlations (green regions) against negative (red regions) and undefined correlations (blue regions). Afterwards we created regions with different scatter types by assigning regions with positive correlations to have lipid scatterers, and the other regions to have aqueous scatterers. To mention that, due to computational limitations we just consider the main structures in Fig. 5a. Then the information of regions with different scatter types was integrated in the simulation model. The results of the CBE simulations for the same time instants as for the temperature presented in Fig. 3a and b are presented in Fig. 5 b and c. We observed that, as expected, regions defined to represent lipid scatterers presented positive relations with temperature, while those with aqueous scatterers tend to present negative relations with temperature. Looking at Fig. 5 we can observe CBE gradients due to the existence of a temperature gradient (more visible at lower temperatures, i.e., in Fig. 5b), which validate the effective coupling between the different COMSOL models.

And, also as expected, the simulated CBE images present similarities with the real correlation image in Figure 5a. This result validate the hypothesis that “CBE propagate along the processing pipeline of the ultrasound equipments and have an expression on conventional B-mode images”. Thus by tracking indirectly CBE from ultrasound images we can develop non-invasive temperature estimation methodologies.

The main limitations of the simulation model is that for now we considered perfect boundary conditions, meaning that no temperature loses are assumed. Even that in the real experiment the overall system was isolated with a polystyrene box, this can be the reason for higher temperature errors at higher temperatures, as presented in Fig. 4. Future model improvements will consider more realistic boundaries, simulating the polystyrene box and loses with the exterior.

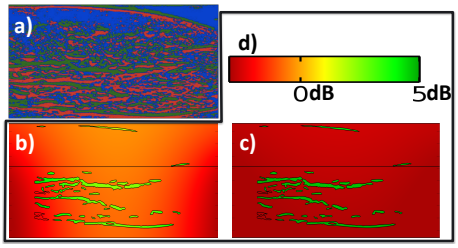

Fig. 5: Simulated CBE variation with temperature at 900s (b) and 2280s (c). a) Correlation between temperature and pixel intensity change, obtained from conventional B-mode images (More details on [7]). Green pixels indicate regions with positive correlations with temperature, red regions negative correlations, and blue regions undefined correlations (i.e., correlations coefficients less than 0.5). d) Scale related with the CBE simulation.

ACKNOWLEDGEMENTS

Financial support of the Luso-Brazilian cooperation project CAPES/FCT ”Thermo-response”.

CONFLICT OF INTEREST

The authors declare that they have no conflict of interest.

REFERENCES

1. Arthur R M, Straube W L, Trobaugh J W, Moros E G. Non-invasive estimation of hyperthermia temperatures with ultrasound. *International journal of hyperthermia.* 2005;21:589–600.
2. Simon C., VanBaren P., Ebbini E.S.. Two-dimensional temperature estimation using diagnostic ultrasound *Ultrasonics, Ferroelectrics and Frequency Control, IEEE Transactions on.* 1998;45:1088 -1099.
3. Arthur R. Martin, Straube William L., Starman Jared D., Moros Eduardo G.. Noninvasive temperature estimation based on the energy of backscattered ultrasound *Medical Physics.* 2003;30:1021.
4. Straube W L, Arthur R M. Theoretical estimation of the temperature dependence of backscattered ultrasonic power for non-invasive thermometry. *Ultrasound in Medicine and Biology.* 1994;20:915–922.
5. Munson Bruce Roy, Young Donald F, Okiishi Theodore Hisao. *Fundamentals of fluid mechanics*. New York 1990.
6. COMSOL . COMSOL Multiphysics User’s Guide 2012.
7. Teixeira C. A., Fontes A., Kruger M. A. Von, Alvarenga A. V., Pereira W. C. A.. Expressiveness of temperature-induced changes in backscattered energy in conventional B-mode images in *Proceedings of Meetings on Acousticsl*;19:075006 2013.

A Change on Backscattered Energy (CBE) simulation model to analyze the influence of heating in ultrasound data

R. J. Simões *, M. A. von Krüger **, W. C. A. Pereira**, C. A. Teixeira *

* Centro de Informática e Sistemas (CISUC), Universidade de Coimbra, Portugal
**Programa de Engenharia Biomédica - COPPE, Universidade Federal do Rio de Janeiro, Brasil
e-mail: ricardodiassimoes@gmail.com

Abstract: Thermal variations influence media properties and consequently induce changes on the propagation of ultrasound (US) waves. Two main questions may arise: Is it possible to estimate temperature based on the variations from the measured US signals? Is it possible to obtain new information (images) from the analysis of the US signals variations? We created two simulation models that enable the assessment of how temperature variations influence the changes on backscattered energy (CBE). Two heating scenarios were considered: slow temperature variations by water-bath heating and heating induced by therapeutic US. The water-bath simulation mimics a real experiment. The therapeutic ultrasound model simulates the heating originated by a piston-like transducer.

CBE simulations were performed in 2D and presented the same patterns as gray-level variations observed on images collected from the real experiment. This fact enables us to conclude that CBE variations observed at the raw-data level propagate along the scanners pipeline and are observed at the final image level. In the same way, the simulations with therapeutic ultrasound allow us to validate past studies were temperature estimation strategies were performed based on the assumption that changes B-Mode gray-level was due to changes on CBE.

Keywords: Change in Backscattered Energy, Ultrasound, COMSOL simulations.

Introduction

Ultrasound (US) is widely used in clinical diagnostic due to its portability and low-cost instrumentation. In the last decades two important concerns of US research were: the improvement of the quality of the image, and the development of trustworthy methods for non-invasive temperature estimation [1,2]. Concerning improvement of image quality, modalities such as harmonic imaging by administration of contrast agents, and elastography were the most important ones. On the other hand, different features from US were extracted aiming to estimate temperature non-invasively. Among the extracted features, changes on backscattered energy (CBE) was one of the more promising ones. CBE is influenced by temperature because they are sensitive to changes in speed-of-sound (SOS) and medium expansion/compression. In literature, it is reported that CBE vary monotonically positive in lipid medium scatterers and monotonically negative in aqueous medium scatters [3].

Recent studies observed variations similar to CBE, computed from raw ultrasound data, in conventional B-mode ultrasound images [4]. In pixel-by-pixel analyses, intensity increases, or decreases with temperature were observed, leading to raising the hypothesis that CBE variations at the raw data level propagate along the processing pipeline of the ultrasound scanners, and are observed in the final images.

In this paper, and aiming to validate the previous hypothesis, we present two simulation models that enable to simulate CBE in the presence of two different heating sources: water-bath heating, and heating by therapeutic ultrasound. Simulations were preformed in the finite element software COMSOL Multiphysics® (COMSOL, Inc).

Materials and Methods

I. Water-bath heating simulation

The water-bath heating simulation reproduces the experimental setup presented in Fig. 1.

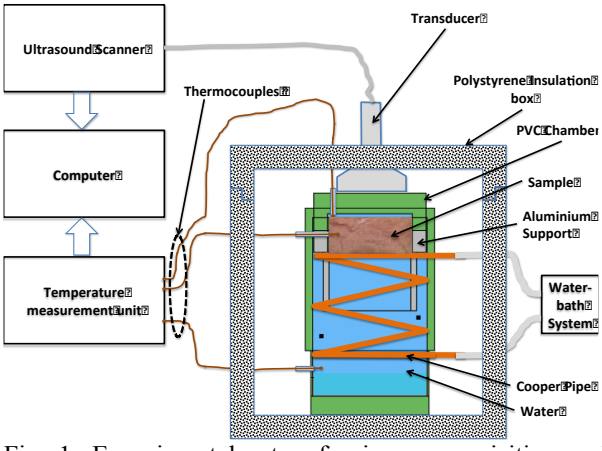

Fig. 1: Experimental setup for image acquisition and temperature change. The experiment is composed by six main parts: a PVC chamber (green) that contains water (blue), a cooper pipe (reddish brown) and an aluminum support (gray); a water temperature control system; an ultrasound scanner; a temperature measurement system; a computer; and a polystyrene isolation box.

In this simulation, the heating process is achieved by simulating the flow of hot water, at 46ºC, in a cooper pipe, which is considered as the heating source. The water inside the chamber is heated, and consequently the solid structures, including the tissue sample under analysis. The simulation model is, in fact, a series of coupled sub-models as presented in Fig. 2.

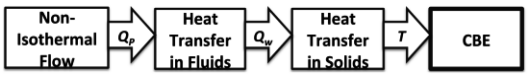

Fig. 2: Coupling between different COMSOL modules. Where Q_P is the heat source from the pipe. Q_W is the transferred heat from the embedded water to the solid structure and T is the system temperature.

Fluids heating convection are ruled by the following equation [5,6]:

$$\rho C_p \frac{\partial T}{\partial t} + \rho C_p u.\nabla_t T = \nabla_t k \nabla_t T + Q_P \qquad (1)$$

Where ρ (kg/m^3) is the density, T(K) is the water temperature inside the chamber, C_P(J/(kg.K)) and k(W/(m.K)) are the water specific heat at constant pressure, and thermal conductivity, respectively. The term Q_P from equation 1 is the heat source originated by the cooper pipe and is defined by: $Q_P = hz(T - T_P)$, where z(m) is the pipe perimeter, and h(W(m^2.K)) is the heat transfer coefficient.

At this point, the water inside the chamber is considered as the heat source for the solid structures (aluminum support and sample). The solids heating conduction process is defined by [6]:

$$\rho C_p \frac{\partial T}{\partial t} = \nabla_t k \nabla_t T + Q_W \qquad (2)$$

Where Q_W(W/m), is the transferred heat from the embedded water to the solid structure.

II. Therapeutic US heating

The other heating approach was by therapeutic ultrasound, which is used in clinics to promote thermal therapies, such as hyperthermia. US heating is simulated by a piston-like transducer. Another aspect in this model is that we consider the bio-heat transfer equation, approaching the simulation to an in-vivo scenario. Fig.3 presents the coupled sub-models used in this simulation.

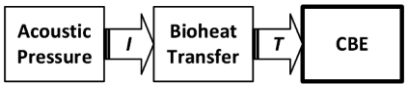

Fig. 3: Coupling between the different modules for therapeutic US heating simulation, where I is the sound wave intensity and T is the system temperature.

The compression and rarefaction epochs imposed by the US induces friction between the media particles, which promotes temperature increases. The US absorption process decreases signal intensity through the sample. The heating process is defined by the bio-heat transfer equation [6]:

$$\rho C_t \frac{\partial T}{\partial t} = \nabla.(k_t \nabla T) + \omega_b \rho_b C_b (T_a - T) + Q + q_m \qquad (3)$$

Where, ρ, C_t and k_t are the density, specific heat and thermal conductivity of the sample tissue, ω_b, ρ_b, C_b are the perfusion rate, density and specific heat of the blood, T_a is the arterial temperature, T is the tissue temperature at instant t, Q is the external heating source and q_m the metabolic heating.

III. CBE simulation

The backscattered energy depends on the attenuation and on the backscattered coefficients of each medium. The backscattered coefficient, also, depends on SOS and density. CBE is modeled in literature by [2]:

$$CBE(T) = \frac{\alpha(T_R)}{\alpha(T)} \frac{\eta(T)}{\eta(T_R)} \frac{1 - e^{-2\alpha(T)z}}{1 - e^{-2\alpha(T_R)z}} \qquad (4)$$

where T is the temperature in ºC, T_R is a reference (basal) temperature, $\alpha(T)$ is the temperature-dependent attenuation, $\eta(T)$ is the backscattered coefficient, and z is the path traveled by a given US wave within the sample volume.

The ratio between the pretended backscattered coefficient (at a given temperature) and the basal backscattered coefficient (at 37ºCelsius) is defined by [2]:

$$\frac{\eta(T)}{\eta(T_R)} = \frac{\left(\frac{\rho_m c(T)_m^2 - \rho_s c(T)_s^2}{\rho_s c(T)_m^2}\right)^2 + \frac{1}{3}\left(\frac{3\rho_s - 3\rho_m}{2\rho_s - \rho_m}\right)^2}{\left(\frac{\rho_m c(T_R)_m^2 - \rho_s c(T_R)_s^2}{\rho_s c(T_R)_m^2}\right)^2 + \frac{1}{3}\left(\frac{3\rho_s - 3\rho_m}{2\rho_s - \rho_m}\right)^2} \qquad (5)$$

where ρ_m is the medium density, $c(T)_s$ is the temperature-dependent SOS of the scatterers and $c(T)_m$, the SOS of the medium.

In literature [7], two types of scatterers are assumed: lipid-based and aqueous-based scatterers, both being part of water-based medium. Table 1 presents the attenuation, SOS and density variation for each type of scatterer. Where $\alpha(T)$, $c(T)_m$, $c(T)_{ls}$, $c(T)_{as}$, ρ_{ls} and ρ_{as} are the temperature dependent attenuation coefficient, SOS in soft-tissue, SOS in lipid scatterers, SOS in aqueous scatterers, density of lipid scatterers and range density of aqueous scatterers, respectively. We implemented equations 4 and 5 in COMSOL and generated solutions over time and temperature. In both simulation models regions with different types of scatterers were defined, thus enabling the observation of CBE with temperature. For the water bath heating experiment we defined regions based on a porcine kidney sample. Images from the sample were acquired using the water-bath experimental setup (Fig. 1).

Table 1 – Properties for CBE simulation equations [7]

Prop	Equation/Value
$\alpha(T)$	$0.98 - 0.003T + 0.8e^{-3}T^2 - 0.68e^{-5}T^3$
$c(T)_m$	$1533.1 + 3.06T - 0.03T^2$
$c(T)_{ls}$	$1810.7 - 13.89T + 0.10T^2$
$c(T)_{as}$	$1471.4 + 4.00T - 0.04T^2$
ρ_{ls}	0.95
ρ_{as}	[1.05;1.2]

As a result from this image acquisition, we observed that different intensity changes occurred in the presence of temperature changes. In a pixel-by-pixel analysis, we observed that positive, negative and undefined correlations exist, being possible to compute an image as presented in Fig. 5a (more details in [4]). Green pixels represent a positive correlation (above 0.5) between the gray-level intensity variation and temperature, red pixels represent a negative correlation (under -0.5) between gray-level intensity variation and temperature, and the blue pixels represent the undefined correlations (with correlation in range of [-0.5 ; 0.5]). We hypothesize that these variations are due to CBE changes. Thus, aiming to prove this hypothesis we defined regions with different scatter types based on the image in Fig. 5a. Due to computational limitations the number of regions were simplified, resulting in the simulations in Fig. 5b and 5c. For the therapeutic ultrasound heating simulation we simplified the definition of the regions, i.e. we created a kidney sample by defining randomly regions with aqueous or with lipid scatterers in the geometry. This is a valid approach since we just wanted to observe the influence of US heating on the medium, and confirm past assumptions that it is possible to compute temperature maps from B-mode images, because average intensity changes are due to CBE changes [8].

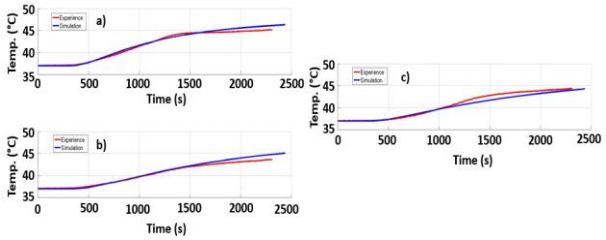

Fig. 4: Simulated (Blue line) vs measured (Red line) temperatures. a) In a specific position inside the medium and chosen to be approximately the same position as used in the real laboratory experiment. b) Water temperature at the top of the chamber. c) Water temperature at the bottom of the chamber.

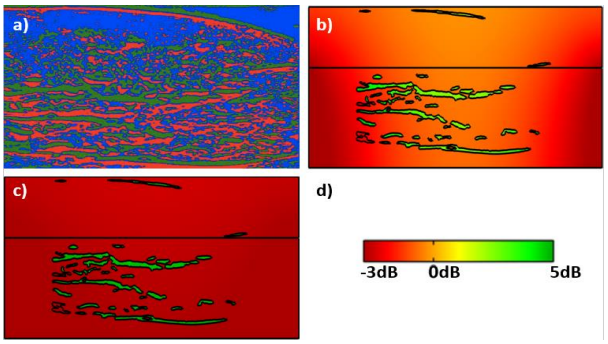

Fig. 5: Simulated CBE variation with temperature at 900s (b) and 2280s (c). a) Correlation between temperature and pixel intensity change, obtained from conventional B-mode images (More details on [4]). Green pixels indicate regions with positive correlations with temperature, red regions negative correlations, and blue regions undefined correlations (i.e., correlations coefficients less than 0.5). d) Color scale related with the CBE simulations in b) and c).

Results & Discussion

Fig. 4 represents the simulated temperature evolution as compared to the measured temperatures for the water-bath heating. The temperatures from simulation are closely related with the temperatures in the experiment, once the root mean square difference is less than 0.52 ºC for all the three-measured points.

Looking at Fig. 5b and Fig. 5c, the temperature increase results in an increase or decrease of CBE, depending on the scatterer types defined for a given region. In Fig. 5b a gradient can be observed due to the inhomogeneous heat diffusion at time instants close to the beginning of the simulation. While time is running, temperature stabilizes at a high level (46ºC) and a homogenous CBE is attained (Fig. 5c). An important observation is that Fig. 5b and 5c are simplified versions of Fig. 5a. This validates the assumption that the intensity variations observed in US images due to temperature are caused by CBE observed at the raw level.

Fig. 6 represents the CBE variation with temperature. The variation tends to be monotonically positive or negative, as theoretically expected. The therapeutic US heating simulations are presented in Fig.7. The simulation considered a frequency of 1MHz and a diameter of 32mm for the therapeutic ultrasound transducer. It was observed that the sample tissue with random media achieves the final temperature (46ºC) in half of the time (1020s) of the water-bath heating; therefore, an homogenous temperature is achieved in the central region close to the therapeutic transducer. CBE vary in the same way as in the previous simulation. With the temperature increase, in the lipid-medium tissues zones (represented as green), CBE increase and

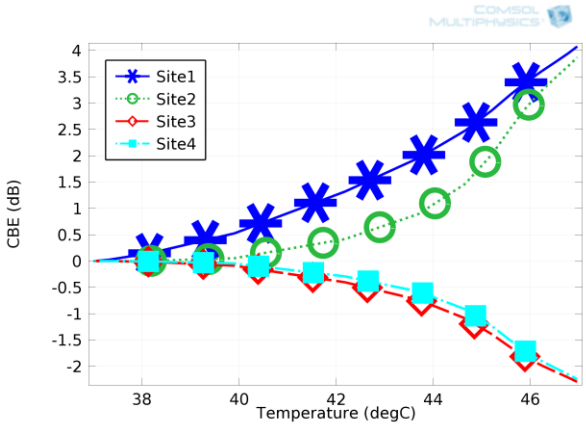

Fig. 6: CBE variation with temperature measured at random sites in kidney sample tissue.

in the aqueous-medium tissues (represented as red), CBE decrease. In [8] we developed non-invasive temperature estimations based on conventional B-mode images, when an ex-vivo tissue sample was heated by therapeutic ultrasound. Again, we hypothesized that these estimations were possible because CBE at the raw US data level propagated along the processing pipeline of conventional scanners. With this simulation we concluded that therapeutic US heating induces CBE patterns similar to the temperature maps obtained in [8].

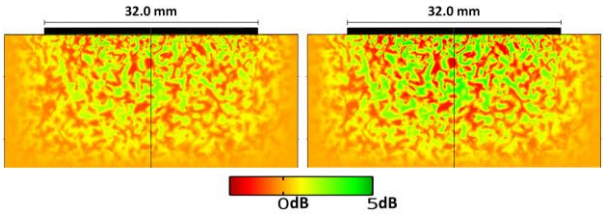

Fig. 7: Simulated CBE variation in therapeutic US heating: a) 390s and b) 1020s.

Fig. 8 present CBE variations from arbitrary places in sample tissue. More linear CBE curves were observed than in the water-bath experiment. This can be explained by the fast heating, resulting in less pronounced steady-state temperature gradients in the area under study.

Conclusion

This paper presents two simulation models that led to the conclusion that CBE changes at the raw data level propagate along the processing pipeline of conventional US scanners and have an expression in the final images. Thus, one can extrapolate that by processing the final images it is possible to extract similar information as by processing raw data, and consequently to develop trustworthy methodologies based on CBE theoretical assumptions. Future developments will consider models that will be able to explain undefined correlations observed in regions with mixed scatterer types.

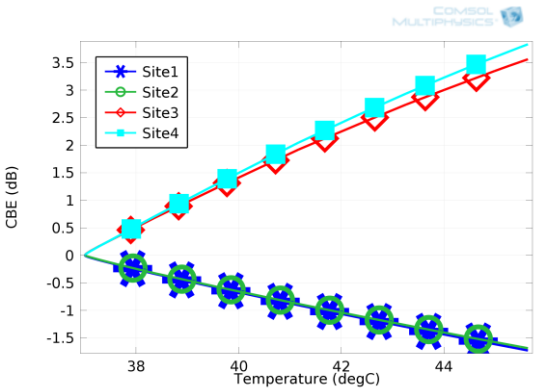

Fig. 8: CBE variation with temperature measured at random sites in the sample with random mediums.

Acknowledgements

Financial support of the Luso-Brazilian cooperation project CAPES/FCT “Thermo-response” (FCT/CAPES: 10172/13-0) and to CNPq and FAPERJ.

References

[1] Simon C., VanBaren P., Ebbini E.S.. Two dimensional temperature estimation using diagnostic ultrasound Ultrasonics, Ferroelectrics and Frequency Control, IEEE Transactions on. 1998;45:1088 -1099.

[2] Arthur R M, Straube W L, Trobaugh J W, Moros E G. Non-invasive estimation of hyperthermia temperatures with ultrasound. International journal of hyperthermia. 2005;21:589–600.

[3] Arthur R. Martin, Straube William L., Starman Jared D., Moros Eduardo G.. Noninvasive temperature estimation based on the energy of backscattered ultrasound Medical Physics. 2003;30:1021.

[4] Teixeira C. A., Fontes A., Kruger M. A. Von, Alvarenga A. V., Pereira W. C. A.. Expressiveness of temperature-induced changes in backscattered energy in conventional B-mode images in Proceedings of Meetings on Acousticsl;19:075006 2013.

[5] Munson Bruce Roy, Young Donald F, Okiishi Theodore Hisao. Fundamentals of fluid mechanics. New York 1990.

[6] COMSOL . COMSOL Multiphysics User’s Guide 2012.

[7] Straube W L, Arthur R M. Theoretical estimation of the temperature dependence of backscattered ultrasonic power for non-invasive thermometry. Ultrasound in Medicine and Biology. 1994;20:915922.

[8] Teixeira C. A., Alvarenga A. V., Cortela G., Kruger M. A. Von, , Pereira W. C. A..Feasibility of non-invasive temperature estimation by the assessment of the average gray-level content of B-Mode images. Ultrasonics, 2014;54:1692-1702.